Hurricane Risk Assessment of Power Transmission Systems: From Physics-Based Surrogates to Parameterized Fragility Models

Hurricane Risk Assessment of Power Transmission Systems: From Physics-Based Surrogates to Parameterized Fragility Models

by

Xinyue Wang

Presented to the Graduate and Research Committee

of Lehigh University

in Candidacy for the Degree of

Doctor of Philosophy

in

Structural Engineering

Lehigh University

Bethlehem, PA

January 2026

DISSERTATION SIGNATURE SHEET

Approved and recommended for acceptance as a dissertation in partial fulfillment of the requirements for the degree of Doctor of Philosophy.

Xinyue Wang

Hurricane Risk Assessment of Power Transmission Systems: From Physics-Based Surrogates to Parameterized Fragility Models

_____
Date

_____
Dr. Paolo Bocchini
Dissertation Advisor

_____
Accepted Date

Committee Members:

_____
Dr. Richard Sause
Committee Chairperson

_____
Dr. Farrah Moazeni
Committee Member

_____
Dr. Ethan Yang
Committee Member

_____
Dr. Jamie Padgett
External Member

Dedication

I dedicate this to my family: Ailan Yin, Qiyun Wang, and Xinjie Wang.

谨以此献给我的家人：殷爱兰、王启云、王新洁。

Acknowledgments

This work and I myself (still a work in progress) would not have been possible without the unwavering love and support of my advisor, Dr. Paolo Bocchini. It has been my sheer luck and privilege to pursue my Ph.D. under his guidance. Over the years, Dr. Bocchini has played many roles beyond that of a research advisor—he has been a mentor, a friend, a "therapist," and at times, truly a father figure. His rigor, dedication, wisdom, and kindness will forever inspire me in my future career and life.

I would like to thank Dr. Richard Sause, my academic advisor and committee chair. I greatly admire his rigor in teaching and research, and he has been both inspiring and supportive throughout my journey. I also wish to express my sincere gratitude to other committee members—Dr. Farrah Moazeni, Dr. Ethan Yang, and Dr. Jamie Padgett—for their valuable support and suggestions at different stages and in various forms. Their time, expertise, and encouragement are warmly appreciated.

Despite being isolated from the buzz of the world, ATLSS has been my research haven and truly my home at Lehigh. I will miss the friends and peers with whom I have worked, studied, and even gone hungry together. I am especially grateful to my dear friend, Sena Mürsel, who began this journey with me and has always been by my side. And of course, to the amazing Tommy Marullo, whose kindness and constant willingness to help us students will never be forgotten.

Lastly, my deepest gratitude goes to my family in China. The return flight I once took for granted in August 2019 has only now approached, more than six years later. It has been

tremendously difficult for both me and my family. I carry deep guilt for all the important moments of joy and sorrow that I have missed, times when I should have been with them. At the same time, I am eternally grateful for their unconditional love, understanding, and resilience. They have been my roots, my rock, and my light during the darkest times.

Table of Contents

List of Tables

List of Figures

Abstract

Electric power systems are vulnerable to hurricane-induced wind hazards, which have historically caused severe damage and widespread outages. Risk and resilience assessment of electric power networks requires estimating the structural response for thousands of structures at the regional scale. In particular, latticed transmission towers can entail large modeling and computational burden when high-fidelity finite element models are used. The lack of appropriate surrogate analytical models (or low-fidelity models) has hindered the efficient modeling of tower portfolios and, in turn, downstream research and applications.

This dissertation advances a multi-scale framework for efficient and realistic hurricane risk assessment of transmission tower portfolios and networks. At the structural scale, panels are abstracted as the basic components in transmission towers, and their failure limit state and engineering demand parameters are defined to capture the buckling failure mode. Physics-based surrogate models for panels are developed, and polynomial response surface metamodels are constructed to ensure consistent simulation of panel capacity and demand. Validation against high-fidelity finite element models confirms that the proposed surrogate beam-column element formulation offers good accuracy and enables efficient panel-based tower analysis; for example, a pushover analysis can be completed within seconds. These surrogate models lay the foundation for deriving portfolio-oriented, parameterized fragility models for transmission towers.

At the portfolio (or class) scale, the dissertation refines the framework for developing parameterized class fragility models by examining a range of modeling choices and propos-

ing improvements to current practices. By applying this framework to a representative class of transmission towers in the Florida transmission line portfolio, parameterized hurricane fragility models are developed using efficient surrogate models and dynamic time history analysis. The results show that inter-structure variability constitutes the dominant source of uncertainty in the tower portfolio; prioritizing this uncertainty in propagation enables more efficient and effective fragility derivation. Sensitivity analysis reveals that tower fragilities are most influenced by three tuning parameters—design wind speed, span length, and yaw angle—as well as by several uncertain variables embedded within the fragility model. The derived fragility models fill the gap in parameterized models for transmission towers and can be tailored to support more granular hurricane risk assessments at the regional scale.

At the network scale, the implications of adopting alternative fragility analysis practices for high-voltage transmission networks are examined. Within a probabilistic simulation framework, three representative fragility models for transmission towers—a parameterized class fragility model, a mean fragility model, and an archetype fragility model—are compared. Network performance is evaluated using multiple metrics such as global efficiency and the number of failed towers. For demonstration, the Florida transmission network is analyzed under two historical hurricanes—Irma (2017) and Michael (2018)—allowing for comparison with observed damage data. Results from both geospatial analyses and aggregate network-level metrics show that the parameterized fragility model consistently yields more reliable and accurate estimates of system performance. In contrast, using the mean fragility model tends to underestimate risk, while using one archetype model substantially overestimates it. These findings highlight the importance of adopting flexible, parameterized fragility models to capture the heterogeneity of transmission assets and to improve the accuracy of large-scale hurricane risk analyses. Such models enhance the fidelity of subsequent recovery and resilience analyses and ultimately support more informed and effective decision-making for power infrastructure under hurricane hazards.

Chapter 1

Introduction

1.1 Motivation

Electric power transmission systems form the backbone of modern society, ensuring the continuous delivery of electricity across long distances. However, these systems are vulnerable to natural hazards such as hurricanes and wildfires. Risk and resilience assessments have become essential for decision-making in both the public and private sectors (Mitchell-Wallace et al., 2017; Schofer et al., 2021). A key component of these frameworks is fragility analysis, for which fragility models (or fragility curves) are commonly used. At the regional or network scale, fragility modeling must account for the compounded effects of structure-to-structure uncertainty arising from heterogeneous portfolios. In electric power systems, this challenge is pronounced, as large transmission networks may include thousands of lattice towers with diverse geometries, materials, and design vintages.

Two mainstream practices exist for regional-scale fragility analysis: (1) the archetype approach and (2) the parameterized approach. Archetype fragility models are developed for a small number of representative structures and then assigned to similar assets within the portfolio (Porter and Cho, 2013; Silva et al., 2019). While this approach is convenient and has historical precedent, it captures heterogeneity only coarsely, which may lead to biased or misleading loss and performance estimates (Rincon and Padgett, 2024). In contrast, parameterized fragility models explicitly incorporate variability in structural characteristics, site conditions, and system configurations by treating them as conditioning parame-

ters. This formulation enables flexible fragility models that capture portfolio heterogeneity more rigorously and yield finer-grained and more reliable damage assessments. Parameterized fragility models have been developed for several asset types—such as bridges (Ghosh et al., 2013; Misra and Padgett, 2019), buildings (Seo et al., 2012; FEMA, 2020), and wood distribution poles (Mohammadi Darestani and Shafieezadeh, 2019)—but remain scarce for critical power infrastructure.

In particular, transmission towers have received limited attention in this regard. Although single-structure and archetype-based fragility models exist (Cai et al., 2019; Dikshit and Alipour, 2023; Fu et al., 2019; Ma et al., 2021a; Macedo et al., 2024; Tian et al., 2020), to date there have been no parameterized fragility models that capture the broad heterogeneity of tower portfolios. This gap limits the accuracy and fidelity of network-level risk and resilience assessments for power systems under hurricane hazards. A key barrier to developing such models is the lack of suitable surrogate analytical models. Traditional finite element (FE) models for towers represent hundreds of individual members to simulate member buckling under wind loads (Mohammadi Darestani et al., 2020; Ma et al., 2021a). While accurate, these high-fidelity models are computationally prohibitive for portfolio-scale analyses. The development of efficient, physics-based surrogate models is therefore essential to enable scalable and realistic fragility modeling of large tower portfolios.

This dissertation aims to advance a multi-scale framework for efficient and realistic hurricane risk assessment of transmission tower portfolios and networks. Specifically, the objectives are threefold: **(1) To develop physics-based surrogate analytical models** for lattice transmission towers that accurately capture their dominant failure modes while greatly reducing modeling and computational demands. **(2) To establish parameterized class fragility models** for transmission towers under hurricane winds, leveraging the surrogate models to efficiently propagate uncertainty and capture inter-structure variability. **(3) To examine the implications of fragility model choice** on network-scale hurricane

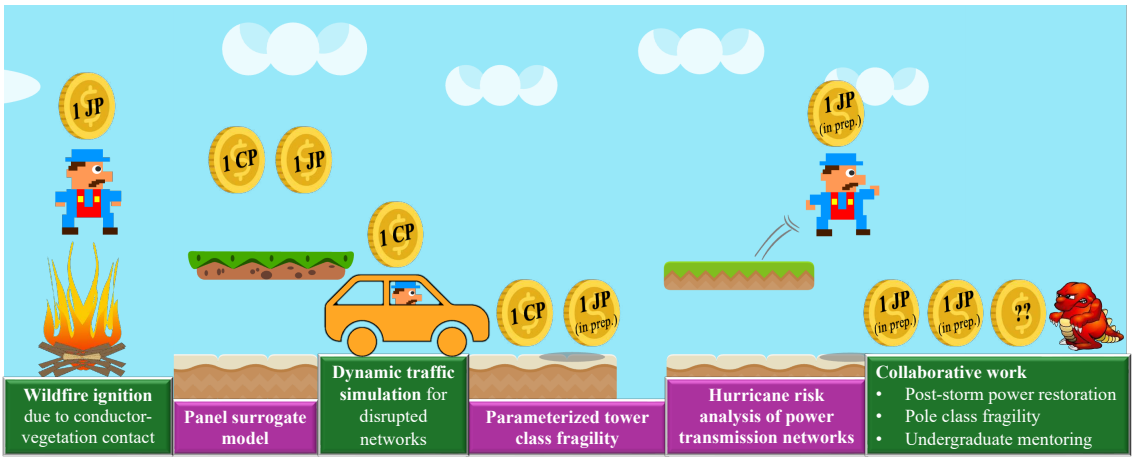

Figure 1.1: Overview of research activities conducted during the Ph.D. program. Green boxes denote research work not explicitly discussed in the following chapters, while purple boxes indicate the studies presented in this dissertation. 'JP' refers to journal papers, and 'CP' refers to conference papers.

risk assessment by comparing alternative modeling practices (parameterized, mean, and archetype models) and evaluating their impact on system-level performance metrics.

1.2 Comprehensive overview of doctoral research

During the Ph.D. program, the author engaged in a variety of research tasks and projects spanning multiple hazard types (e.g., wildfire, earthquake, and hurricane wind), infrastructure systems (e.g., transportation and electric power), and stages of the resilience modeling framework (i.e., hazard, fragility, and recovery). Figure 1.1 provides an overview of all research activities undertaken during the Ph.D. program. This dissertation focuses on the three research activities highlighted in purple boxes. The topics shown in green boxes in Figure 1.1 are briefly described in this chapter but are not presented in detail in subsequent chapters.

The first research task focused on understanding **wildfire ignition caused by conductor–vegetation contact under strong wind conditions**. During high-wind events with dry weather, electric power systems can become sources of catastrophic wildfires, with conduc-

tor–vegetation contact recognized as a major ignition mechanism. To support operational decision-making—such as vegetation management and preventive power shutoffs—there is a pressing need for accurate wildfire risk analysis. In this study, the ignition mechanism was investigated by modeling the dynamic swaying of transmission line conductors toward nearby vegetation, leading to potential flashover. The limit state was defined as the conductor encroaching into a prescribed minimum vegetation clearance. The stochastic characteristics of the dynamic displacement response of a multi-span transmission line were derived through efficient spectral analysis in the frequency domain, and the encroachment probability at specific locations was estimated by solving a first-excursion problem. Unlike static-equivalent models often used in practice, this approach demonstrated that random wind buffeting significantly contributes to conductor displacement under turbulent wind conditions. Neglecting this dynamic component can lead to substantial errors in ignition risk estimation. The analysis also revealed that ignition probability is highly sensitive to vegetation clearance, wind intensity, and the duration of strong wind events, underscoring the importance of high-resolution data for accurate prediction. This research proposed a mechanistic and probabilistic methodology for efficient and accurate estimation of wildfire ignition probability, advancing the capability for wildfire risk assessment in power systems. The work was published in *Scientific Reports (Nature Portfolio)* (Wang and Bocchini, 2023).

The author also had the opportunity to apply several concepts and tools originally studied for power networks to other infrastructure systems and hazards. In particular, she contributed to an interdisciplinary project in collaboration with researchers from Electrical and Computer Engineering to develop machine learning algorithms for traffic prediction. Her main contribution focused on **integrating dynamic traffic simulations to model post-disaster conditions in disrupted transportation networks**. Specifically, she analyzed the response of a large transportation network in San Francisco subjected to both small-scale

disturbances (e.g., protests) and large-scale events (e.g., earthquakes). Part of this research was published in the *Conference Proceedings of IABMAS 2024* (Wang et al., 2024).

In addition to her main research efforts, the author also contributed to **several collaborative projects**. Notably, the author co-led a study on post-storm power recovery, where she and her collaborators conducted expert surveys and interviews to collect information on the restoration of transmission assets after hurricanes. This work is ongoing, with data collection largely completed. The author is also a co-author of a paper on the fragility modeling of transmission steel poles, leveraging her expertise in developing class fragility models. Furthermore, throughout the Ph.D. program, the author has been actively involved in undergraduate research mentoring. She has mentored two REU students and three Lehigh undergraduate students, guiding them in research that has led to conference presentations and, in some cases, journal publications.

1.3 Outline of the dissertation

This dissertation is organized into three core chapters, each addressing a key component of the overall research framework.

Chapter 2 introduces the physics-based surrogate modeling approach for lattice transmission towers. Panels are defined as the basic structural components, and their limit state and engineering demand parameters are established to capture the dominant buckling failure mode. Surrogate beam-column formulations and response surface metamodels are developed and validated against high-fidelity FE models, enabling efficient and accurate panel-based tower analysis.

Chapter 3 refines the framework for developing parameterized class fragility models and applies it to a representative class of transmission towers in the Florida network. Using

the surrogate models and dynamic time history analysis, parameterized hurricane fragility models are derived. Sensitivity analysis is carried out to quantify the influence of key tuning parameters and sources of uncertainty.

Chapter 4 extends the analysis to the network scale. Within a probabilistic simulation framework, three fragility analysis practices—parameterized fragility, mean fragility , and archetype fragility—are compared to assess their implications for network-level hurricane risk. The Florida transmission network is analyzed under Hurricanes Irma (2017) and Michael (2018), and the results are evaluated against historical damage data.

Finally, **Chapter 5** summarizes the findings, discusses the broader implications for infrastructure risk and resilience analysis, and highlights the research contributions.

Chapter 2

Physics-based surrogate models of panels for portfolio analysis of transmission towers under hurricanes

2.1 Introduction

This study aims to provide a new approach to structural modeling of power transmission towers for large-scale risk and resilience analysis. The proposed approach balances the need to accurately capture the main mechanical failure mode of these structures (i.e., leg buckling) and the need to have few parameters for direct probabilistic simulation of large tower portfolios in a region (e.g., the entire east coast of Florida, affected by a hurricane). Risk and resilience assessments have become essential for decision-making in both the public and private sectors, such as federal funding allocation, public policy making, and catastrophe modeling for insurance portfolio management (Mitchell-Wallace et al., 2017; Schofer et al., 2021; U.S. Department of Transportation, 2023). A key component of the risk and resilience modeling framework is the fragility analysis (or damage analysis) for which fragility functions are commonly used (Cimellaro et al., 2010). The fragility functions, often represented as fragility curves, reflect the effect of various sources of uncertainty and predict the damage levels of physical assets probabilistically (Melchers and Beck, 2018). At the regional or network scale, as opposed to the single structure scale, uncertainty is compounded by the heterogeneity in the portfolios of structures that can exhibit diverse structural configurations, such as bridges in transportation networks (FHWA, nd) and transmission towers in power networks (Fang et al., 1997).

There are two mainstream practices for regional-scale fragility analysis—employing a few archetype fragility functions and employing parameterized fragility functions. An archetype fragility function is developed for a selected archetype structure that is assumed to be representative of an entire subset of the portfolio (Porter and Cho, 2013; Silva et al., 2019). Once the archetype structure is selected, the procedure to derive the archetype fragility is essentially the same as for conventional single structure fragility, which yields a fragility model conditioned on the intensity measure(s) only. Despite their wide availability and the legacy of being adopted in many contexts, archetype fragilities cannot capture important subtleties in portfolio loss predictions and may lead to unreliable conclusions (Rincon and Padgett, 2024). On the other hand, a growing body of researchers (Ghosh et al., 2013; Misra and Padgett, 2019; Mohammadi Darestani and Shafieezadeh, 2019; Seo et al., 2012) have focused on developing flexible fragility models that are parameterized by a vector of variables (e.g., structural features, site characteristics, system configurations, and material properties). Such parameterized fragilities can be tailored to capture the portfolio heterogeneity, thus providing more granular and reliable damage assessment at the regional scale. However, parameterized fragility models are scarce and only available for very few types of structures. In particular, electric power transmission networks play a critical role in the modern society, yet hurricane events have manifested and continue to highlight the vulnerability of transmission towers (NERC, 2018; U.S. Department of Energy, 2013; Schweikert et al., 2019). Therefore, there is the urgent need of parameterized fragility models of transmission towers for better supporting the risk and resilience analysis of transmission networks.

Structural fragility development is a mature field, and indeed fragility models of single or archetype transmission towers are available in the literature (Cai et al., 2019; Dikshit and Alipour, 2023; Du and Hajjar, 2022; Fu et al., 2019; Ma et al., 2021a; Macedo et al., 2024; Miguel et al., 2023; Padilha Alves et al., 2024; Tian et al., 2020; Xue et al., 2020). In

contrast, the development of portfolio-oriented fragility models for transmission towers entails modeling and analyzing a large number of towers of a variety of structural configurations; hence, the usual approach, affordable for deriving (a few) archetype fragilities, can be prohibitively expensive in these cases. For hurricane wind load analysis, transmission towers have been traditionally modeled at the member level because the primary failure mode is the buckling of steel angle members (Ma et al., 2021a; Mohammadi Darestani et al., 2020). That is, hundreds of members (legs, bracings, etc.) would be explicitly included in the finite element (FE) model. This high-fidelity modeling approach not only makes the tower models expensive to create and analyze but also is laborious to adapt for modeling various structural configurations. It could be argued that one of the most important factors hindering the derivation of parameterized tower fragilities is the lack of appropriate surrogate models for efficient modeling of tower portfolios.

In the context of portfolio or regional analysis, physics-based surrogates (also known as reduced order models or low-fidelity models) are typically adopted to alleviate the modeling complexity and computational cost (Misra and Padgett, 2019; Nielson, 2005; Padgett, 2007; Patsialis and Taflanidis, 2020). For example, bridges have been customarily modeled as structural systems consisting of several types of components, where each component is encapsulated by a few modeling parameters despite its internal complexity. Different from the purely data-driven surrogate models, the physics-based surrogate models aim to simplify the physics-based description of the original high-fidelity FE models through some form of abstraction and/or condensation. The desired features shared by these simplified yet rigorous surrogate models are: (1) the surrogate model should describe the mechanical behavior of the subject component with sufficient accuracy and capture the important limit states (LSs), so as to inform subsequent loss and recovery modeling; (2) the formulation and implementation of the surrogate model should provide high efficiency for FE model creation and analysis; and (3) the surrogate model should be general enough to model

the various structural configurations observed in the portfolios. Concerning the simplified models of transmission towers, past studies used the lumped mass model or a monolithic elastic cantilever beam model for earthquake load analysis (Chen et al., 2016; Gong and Zhi, 2020; Li et al., 2005). However, these oversimplified models are not suitable for wind load analysis as they fail to capture the buckling-induced tower failure mechanism.

To fill the noted gaps, this study develops physics-based surrogate models of panels for analyzing portfolios of transmission towers under hurricanes. Buckling is the dominant failure mode in transmission towers. This study specifically focuses on leg buckling, as it can trigger global instability and, in turn, tower collapse. In pursuit of efficient probabilistic simulation at the portfolio scale, model reduction is achieved based on a novel abstraction: panels are treated as the basic components of the tower (Section 2.2.1). Section 2.2.2 outlines the variation in panel characteristics observed across existing tower portfolios, while Section 2.2.3 introduces the high-fidelity FE model employed throughout the study. For the panel component, the limit state and engineering demand parameters (EDPs) are defined, all centered on capturing the leg buckling (Section 2.2.4). An analytical surrogate model is then developed to represent the panel's mechanical behavior and compute the relevant EDPs (Section 2.2.5). Section 2.3 presents the development of a metamodel, which addresses the need for consistent simulation of panel capacity and demand. Section 2.4 details the results of the metamodel. Finally, Section 2.5 presents the validation and an example application of the proposed surrogate model. The proposed approach enables panel-level FE modeling and panel-based failure analysis of towers.

This work offers value across at least three use cases, represented by the three main boxes in Figure 2.1. First, it introduces a methodology for developing surrogate panel models applicable to various types of lattice steel towers. In this study, the methodology is applied to self-supporting, suspension, and tangent towers with double circuits and a vertical crossarm configuration (SST2V). However, it can also be used to create surrogate

models for other types of transmission towers or even for triangular telecommunication towers. Second, the work shows how to develop wind fragility curves for individual transmission towers, leveraging the surrogate models. Specifically, an analyst aiming to develop a fragility model for any particular tower within the SST2V class can use the surrogate panel models calibrated in this study. By inputting the specific parameters for the panels of the investigated tower, the analyst can leverage the resulting surrogate to improve the efficiency of probabilistic simulations and FE analyses. Finally, the third and ultimate use case is the development of fragility models for tower portfolios, to support regional-scale analysis. For instance, an analyst can use the surrogate panel models to derive a parameterized class fragility model for all SST2V towers. This can be achieved by exploring several archetype towers and blending their results (Porter and Cho, 2013), by conducting design of experiments to explicitly examine the effect of varying each parameter (Mohammadi Darestani and Shafieezadeh, 2019), or by applying any other technique for class fragility development. In all these cases, the proposed surrogate model can facilitate the probabilistic simulation by reducing the number of relevant structural parameters and substantially accelerate the FE analyses.

2.2 Methodology for developing physics-based surrogate analytical models for panels

2.2.1 Abstraction of panels as basic components

A transmission line consists of two distinct systems: the wire system (e.g., conductors, ground wires, insulators), and the structural support system (e.g., lattice towers, poles). The electrical function governs the configuration of the wire system, and in turn the design of the supporting structures (Catchpole and Fife, 2014). Figure 2.2a shows two typical

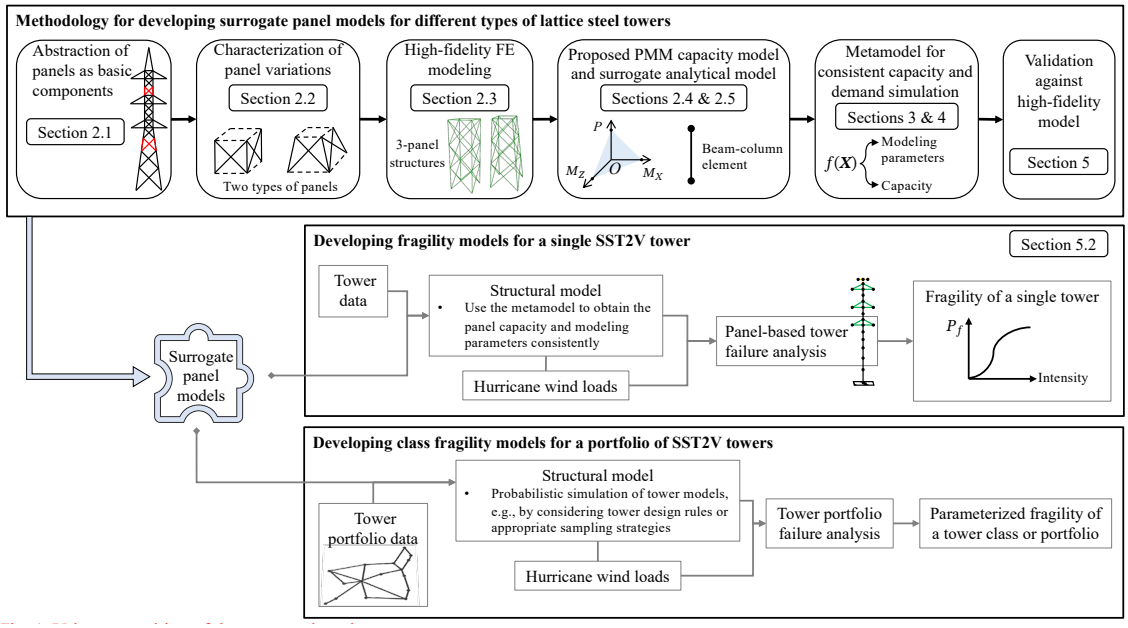

Figure 2.1: Value proposition of the presented work and the structure of the chapter.

transmission towers used respectively in the three-phase single-circuit transmission lines and double-circuit transmission lines. In particular, this study focuses on the double-circuit towers that are commonly found in both high-voltage lines (69 to 230 kV) and extra-high-voltage lines (345 kV and above). In the context of portfolios of towers, the validity of abstracting panels as the basic components can be argued from two perspectives: the design and construction perspective, and the mechanical perspective.

In practice, transmission towers are usually designed and constructed with the 'tower family' concept, which leads to standardization and modulization of towers project-wide (Britton and Bouslog, 2015; Kalaga and Yenumula, 2017). A lattice tower is generally comprised of a basic body, a body extension, and a leg extension, as illustrated in Figure 2.2b for a double-circuit tower. The basic body exists in all towers and is made up of a straight body—with peak(s) and crossarms attached to it—and an inclined body. Being optional, the body extension and leg extension may be added to the basic body to achieve the desired tower height (Fang et al., 1997). From the design and construction perspective, the panel (see Figure 2.2b) can be identified as the modular unit shared by towers along a

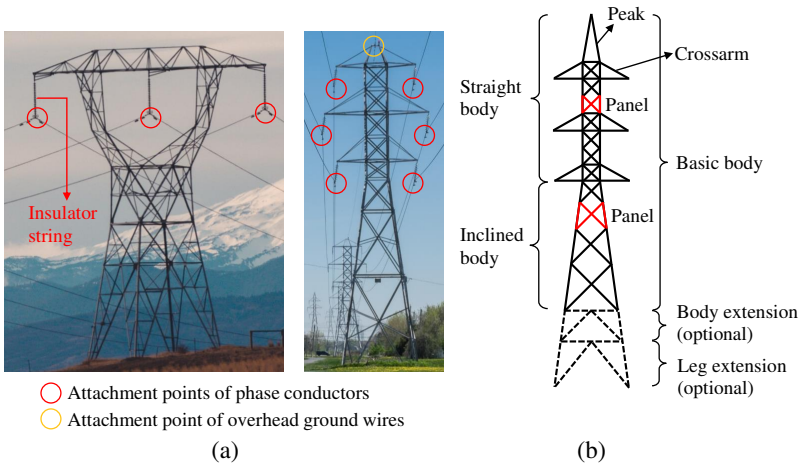

Figure 2.2: (a) Single-circuit transmission tower (left) and double-circuit transmission tower (right), adapted from images on Unsplash (Muhr, nd; Jarry, nd); (b) Illustration of the composition of a tower and the panels thereof.

power line or, in general, by portfolios or classes of towers.

Taking the mechanical perspective, a panel constitutes a basic unit for capturing the failure modes of transmission towers. As illustrated in Figure 2.3a, there are mainly three types of members in a tower: legs, diagonal bracings, and redundant bracings, for which steel equal angles (see Figure 2.3b) are predominantly used. The legs and diagonal bracings are the primary members that carry and transfer the vertical and shear loads to the tower foundation. The redundant (or secondary) bracings are used to reduce the unbraced lengths of the primary members by providing intermediate support to them (ASCE, 2015). Figure 2.3c shows the idealized load paths indicated by the tensile or compressive member forces under different load cases, considering only axial loads inside the angle members (i.e., space truss assumption). The axial load and bending moment are primarily taken by the legs whereas the shear load and torsional moment are mainly carried by the diagonal bracings. The primary failure mechanism of transmission towers is partial failure or collapse caused by member buckling (Dikshit and Alipour, 2023; Tapia-Hernández and Sordo, 2017; Ma et al., 2021a; Mohammadi Darestani et al., 2020). Based on its ability to capture the full unbraced buckling lengths of the members, a panel stands as a self-contained and effec-

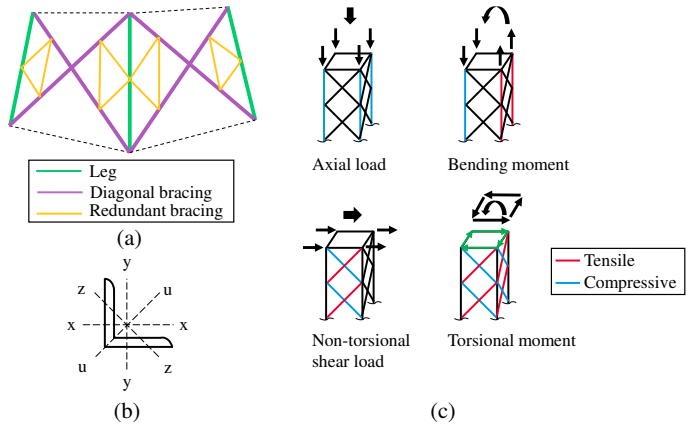

Figure 2.3: (a) Tower members illustrated using a panel in the inclined body; (b) Angle section with equal legs; (c) Load paths under different load cases illustrated using panels isolated from the straight body.

tive scope for surrogate modeling (Wang et al., 2023). Lastly, it is worth noting that the panel concept defined in Figure 2.2b may differ from other works where 'panel' refers to an arbitrary segment of the tower.

2.2.2 Characterization of panel variations

With panels abstracted as the basic components, this subsection summarizes the variations of panels that are observed in portfolios of towers. A panel design routine is then presented in compliance with the design standard requirements and industry practice. As done for other types of structures (Misra and Padgett, 2019; Nielson, 2005), understanding the characteristics and variations of the components is essential for developing surrogate analytical models and capacity models that are applicable to various structural configurations across portfolios. Such understanding is also useful for selecting the appropriate strategies to propagate uncertainties. In particular, this study focuses on transmission towers of square section (in plan view) instead of the less commonly used triangular or rectangular sections. First, the panels present in the tower basic body can be divided into two types: the inclined type that constitutes the inclined body, and the straight type found in the straight body. For

both types, the panel variations can be characterized by several aspects, including topology, geometry, size, connections, etc.

- Topology: the topology of a panel refers to the configuration of its constituent members and is usually designed based on the engineer's experience (de Souza et al., 2019). The double warren (also known as double 'X') system is the most commonly used bracing system throughout the world (Kravitz, 1985). Figure 2.4 illustrates the topology where the double warren system is used in all four faces of the panel. The system is known to perform better when the angle at the intersection of diagonal bracings (θ in the figure) is close to the value of 90° (de Souza et al., 2016). Starting with the basic double warren bracing system, redundant bracings may be added as needed, thus forming various topologies.

- Geometry: the panel geometry refers to its dimensions in the three-dimensional (3D) space. As shown in Figure 2.4, the panel geometry can be described by the top width (w_t), the bottom width (w_b), the leg slope (α_p), and the vertical height (h_v). The leg slope of the inclined type is around 4° according to common design practice, while the straight type has $\alpha_p = 0°$ (Fang et al., 1997; de Souza et al., 2016). Fixing both θ and α_p to their typical values (i.e., $\theta = 90°$, $\alpha_p = 4°$ for inclined type or 0° for straight type), the panel geometry can be fully determined upon knowing one geometric dimension from which all other dimensions can be derived. For convenience, the panel top width (w_t) was selected as the independent geometric dimension in this study.

- Size: the size of a panel refers to the cross-sectional sizes (or profiles) of the steel members used therein. Single steel equal angles (see Figure 2.3b) are predominant in transmission towers due to their market accessibility and construction convenience. Within a panel, typically all legs share the same size and all diagonal bracings share

the same size. In the United States, towers have been generally made of ASTM A36 steel since 1960 (ASCE, 2015; Kalaga and Yenumula, 2017). Table A.1 lists 51 commonly used angle sizes in the United States according to PLS-TOWER (Power Line Systems, nd) which is the industry-leading tower design software. Note that all the 51 sections satisfy the minimum thickness requirement ($t \geqslant 1/8$ inch) and the maximum width-to-thickness ratio requirement ($w/t \leqslant 25$) (ASCE, 2015).

- Connection: bolted connections (or joints) in transmission towers are normally designed as bearing type connections and exhibit considerable variations. Depending on the connecting members, the connections can be classified into leg-to-leg connections, bracing-to-leg connections, and bracing-to-bracing connections (see Figure 2.5a). Many researchers found that bolt slippage can have a significant impact on the tower performance (Jiang et al., 2017; Mohammadi Darestani et al., 2020; de Souza et al., 2019). The joint slippage behavior is affected by many factors, such as the number of bolts and the construction clearance. Figure 2.5b illustrates the four-phase slippage model that is used as the basis in this study (Ungkurapinan, 2000).

- Lastly, it is worth noting that apart from the above-mentioned macroscale panel variations, there are also other variations (such as yield stress, Young's modulus) that have been traditionally considered in the context of a single structure (Dikshit and Alipour, 2023).

Based on the variations above, a panel design routine was developed in this study that completes the pattern design of redundant bracings and determines the buckling lengths of the primary members. As shown in Figure 2.6, for a panel of a given type, the geometry and size are first determined; then the pattern of redundant bracings is determined through topology design. To this end, common bracing patterns were translated into a set of predefined rules, and the limiting slenderness ratios for legs and diagonal bracings are checked

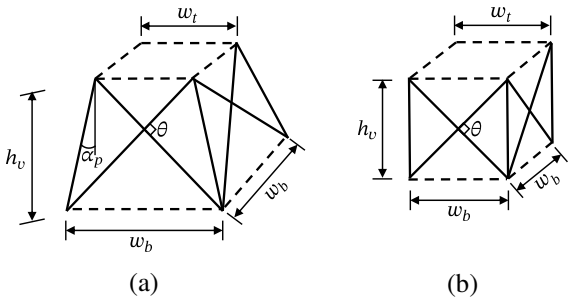

Figure 2.4: Illustration of panel topology (showing only primary members) and geometry: (a) Inclined type; (b) Straight type.

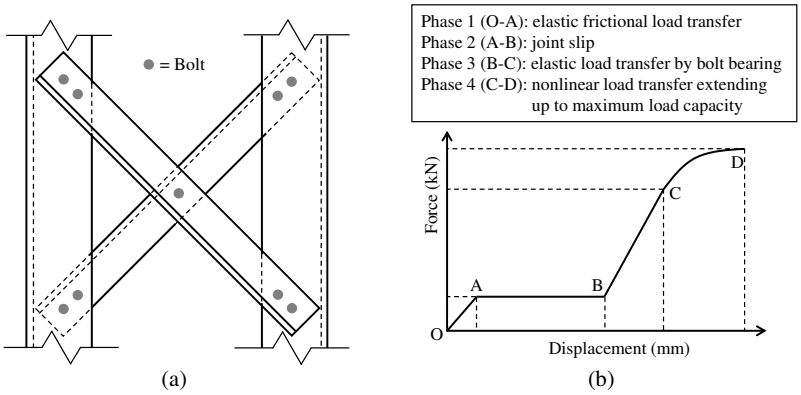

Figure 2.5: (a) Typical bolted connections; (b) Force-displacement diagram for tension joints and simple joints (no gusset plates or splice angles). Both plots are not necessarily drawn to scale and are mainly for illustration purposes.

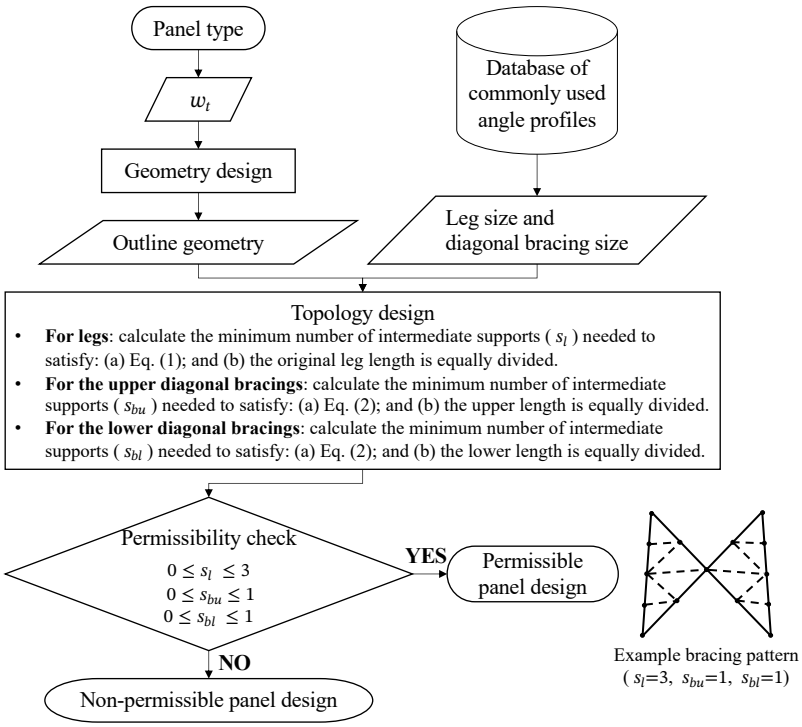

Figure 2.6: Flowchart of the panel design routine.

using Equation (2.1) and Equation (2.2), respectively (ASCE, 2015):

$$\frac{L}{r} \leqslant 150 \tag{2.1}$$

$$\frac{KL}{r} \leqslant 200 \tag{2.2}$$

where L is the unbraced length (m); r is the radius of gyration (m^4); and K is the effective length coefficient. The effective length (KL) shall be determined based on the end conditions (ASCE, 2015). Note that a panel design obtained by this routine is agnostic about the tower as well as the (design) loads because no capacity check is performed. This routine helps to ensure that the generated panel designs are reasonable and consistent with characteristics observed in tower portfolios. It is integrated into the design of experiments (Section 2.3.1), where panel characteristics are varied, and any non-permissible designs are

excluded from further analysis.

2.2.3 High-fidelity finite element modeling of panels

High-fidelity FE models were employed in this work as benchmarks for the proposed panel capacity model (Section 2.2.4), the proposed surrogate analytical model (Section 2.2.5), the derivation of the metamodel (Section 2.3), as well as the validation and application (Section 2.5). The first and most fundamental modeling choice concerns the approach used for buckling analysis. In general, two approaches are available. The first approach relies on the Structural Stability Research Council (SSRC) formula to estimate the compressive capacity of angle members, incorporating the concept of effective length (ASCE, 2015). While this approach shows good agreement with extensive test results, it is an approximate approach. The second approach involves directly modeling the realistic buckling behavior of angle members. This entails significant modeling complexity—including residual stresses, initial out-of-straightness, among other high-fidelity features—as well as increased FE analysis challenges. This approach has recently gained increasing popularity due to its higher accuracy and rigor (Mohammadi Darestani et al., 2020). In particular, the derivation of the metamodel in this study involves modeling and analyzing hundreds of 3-panel structures with varying configurations (e.g., size, geometry, and topology). The difficulty of directly modeling buckling behavior is further compounded by the need to handle such a large number of structurally distinct cases. As a result, the direct modeling approach was deemed impractical in this context and was not pursued. Instead, this study adopted the first approach (see details in Section 2.2.4); despite being less accurate, it provides a reliable approximation of member buckling capacity and reflects a practical trade-off between accuracy and feasibility.

With OpenSees as the chosen FE platform (McKenna et al., 2010), the features of the high-fidelity FE models are summarized below. As mentioned earlier, the redundant brac-

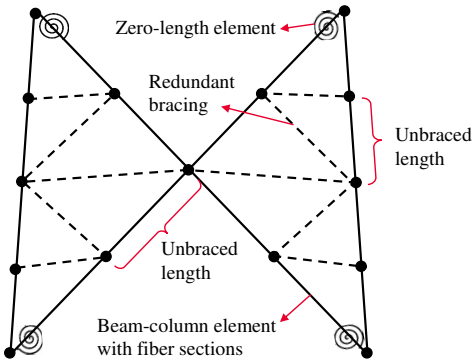

Figure 2.7: High-fidelity finite element model illustrated for a complex bracing pattern.

ings are used—when necessary—to reduce the unbraced buckling lengths of primary members and do not carry any significant load (referred to as zero-load members). In practice, it is customary to not include the redundant members in the tower analysis and this study adopted the same approach (Power Line Systems, nd; de Souza et al., 2016). Even though the redundant bracings were not explicitly included in the FE model (see Figure 2.7), their effects were accounted for by setting the correct buckling lengths of primary members in calculating their buckling capacities. It is worth noting that this modeling simplification was made to facilitate the exploration of various structural configurations. Notably, it aligns with the use of an effective length-based approach for assessing buckling capacity. However, if a direct modeling approach for buckling were adopted, explicitly modeling the redundant bracings would be essential, as they can play an important role in maintaining structural stability and influencing deformations under ultimate load conditions.

The primary members were modeled by force-based beam-column elements (as opposed to truss elements) to account for the bending moments that are present in real towers. In order to consider the interaction between the axial force and bending moment, fiber sections were utilized where each fiber was modeled by the bilinear steel material. One detail worth mentioning is that a 3D rotation procedure was employed so as to correctly specify the orientations of the local axes of angle members (see Figure 2.3b).

The flexible connections (or joints) were modeled using zero-length elements, but not all connections need to be modeled this way. Tower structures are typically subdivided into smaller sections for transport and erection purposes (Kalaga and Yenumula, 2017), which governs the positions of leg-to-leg connections. The legs are continuous for most panels, while some panels include leg-to-leg connections. The leg-to-leg connections are normally lap splices where both flanges are bolted with multiple bolts. This type of connection can be assumed rigid as it transfers the bending moment fully (Ma et al., 2021a). Since panels without leg-to-leg connections are the most common both within individual towers and across the portfolio, these connections were omitted during the surrogate model development. However, it should be noted that this simplification neglects cases where leg-to-leg connections are present and may introduce slippage effects—particularly under tension, where increased deflection may occur due to separation between angle members. In such cases, results may be affected, and separate studies may be warranted to investigate this type of panels, especially for towers with many leg-to-leg connections or where leg members are prone to large tension. Moreover, depending on the realized bracing pattern, the connections at the intersection of diagonal bracings can become very complex (such as the case shown in Figure 2.7). With the redundant bracings and the connections thereof already omitted from the model, for simplicity, this study further neglected the connections at the diagonal intersection. As a result, only the flexible connections between the diagonal bracings and the legs were considered, which still captures what is arguably most important slippage effect, because the diagonal bracings are the primary load-bearing members under shear loads.

While joint eccentricities were neglected, the joint slippage behavior (as depicted in Figure 2.5b) was modeled using the parallel material approach proposed by Mohammadi Darestani et al. (2020). Note that the joint failure was not considered herein since it is extremely rare in reality (Ma et al., 2021a). To account for the semirigid behavior of the connections con-

sisting of more than one bolt, the rotational stiffness was modeled according to the method suggested by Jiang et al. (2017). In addition, the geometric nonlinearities can be considered via the corotational geometric transformation.

2.2.4 Proposed PMM capacity model

Being physics-based, the abstracted new 'panel component' entails defining the limit states (LSs) and engineering demand parameters (EDPs) as for any conventional structural component. However, the LSs and EDPs should be defined at the panel level, encompassing all the constituent members. This section first discusses the panel failure modes and then defines one LS and three EDPs for a panel, following which the limit capacity model is proposed.

The panel failure modes essentially depend on the failure of individual members due to yielding or buckling. Although yielding could occur, independent studies have found that buckling is the dominant failure mode (Dikshit and Alipour, 2023; Mohammadi Darestani et al., 2020). The leg buckling especially can lead to global instability of transmission towers and in turn the tower collapse. Based on personal communication with experts in tower testing and their field observations, legs almost always fail in compressive buckling, whereas leg tension failure (extremely rare) may occur only under abnormal circumstances such as serious corrosion or conductor galloping.

The limit state considered in this study is the collapse of the panel, which in turn will lead to partial or, more likely, total collapse of the tower. This panel failure limit state corresponds to the failure of any of the legs in compression. Recall that legs mainly carry the axial and bending moment loads on the panel (see Figure 2.3). Therefore, this study proposes using the axial load and the two bending moments (PMM for short) as the EDPs to quantitatively capture the panel failure upon leg buckling. The compression capacity (P_c)

of an angle member can be calculated based on the SSRC formula which is also adopted in the design standard (ASCE, 2015):

$$P_c = F_a \cdot A_g \tag{2.3}$$

$$F_a = \begin{cases} \left[1 - \frac{1}{2}\left(\frac{KL/r}{C_c}\right)^2\right] \cdot F_{cr}; & \frac{KL}{r} \leqslant C_c \\ \frac{\pi^2 E}{\left(\frac{KL}{r}\right)^2}; & \frac{KL}{r} > C_c \end{cases} \tag{2.4}$$

$$C_c = \pi\sqrt{\frac{2E}{F_{cr}}} \tag{2.5}$$

where A_g is the gross cross-sectional area (m^2); F_a is the allowable compressive stress (Pa); E is the modulus of elasticity and it is usually taken as 200 GPa; F_{cr} is the critical stress (Pa); and C_c is the critical slenderness ratio that separates the elastic and inelastic buckling. The critical stress (F_{cr}) reflects the reduction of material's yield stress (F_y) based on the width-to-thickness ratio (w/t) of the section and can be obtained by:

$$F_{cr} = \begin{cases} F_y; & \frac{w}{t} < \frac{80\Psi}{\sqrt{F_y}} = \left(\frac{w}{t}\right)_{\lim} \\ \left[1.677 - 0.677\frac{w/t}{(w/t)_{\lim}}\right] \cdot F_y; & \left(\frac{w}{t}\right)_{\lim} \leqslant \frac{w}{t} \leqslant \frac{144\Psi}{\sqrt{F_y}} \\ \frac{0.0332\pi^2 E}{(w/t)^2}; & \frac{w}{t} > \frac{144\Psi}{\sqrt{F_y}} \end{cases} \tag{2.6}$$

where $\Psi = 2.62$ for F_y in MPa. Note that here the effective lengths (KL) of members consider the effects of redundant bracings (omitted in the FE model) as well as the end conditions.

Moreover, the values of the EDPs (PMM) corresponding to the failure limit state can be referred to as the limit capacities of the panel, which form a surface in the 3D space illustrated in Figure 2.8. The panel failure depends on the failure of the leg subjected to the highest compression. This compression force arises mainly from the combined axial

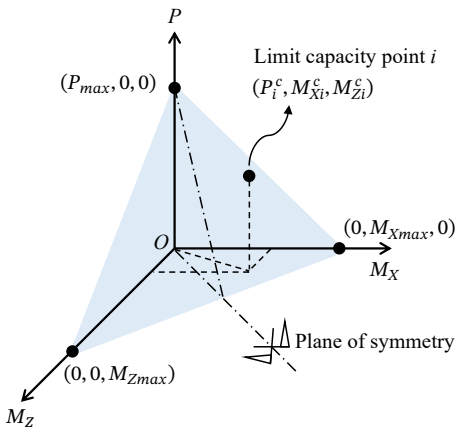

Figure 2.8: Illustration of the PMM limit capacity surface for a panel.

and bending loads, which would result in the panel's limit capacity surface being a plane in linear mechanics. In reality, the activation of the nonlinear joint behavior causes the PMM capacity surface to not be exactly a plane. However, the deviation from a perfect plane is minimal and can be considered negligible for practical purposes. This hypothesis is supported by a numerical investigation, where the PMM capacity surfaces were constructed point by point using 3-panel structures (Figure 2.9). This setup allows more realistic consideration of the boundary conditions of the panel (as in a real tower). The design of the 3-panel structures can be divided into two logical steps. First, the middle panel (panel of interest) is designed using the design routine introduced in Section 2.2.2. Second, assuming that the top panel and the bottom panel share the same leg size and the same bracing size as the middle panel, the other two panels are designed accordingly. The 3-panel structures were modeled with the same high-fidelity modeling approach described in Section 2.2.3. The bottom nodes of the bottom panel are fixed, while the top panel has no constraints. A computer code was written to automate the design and the FE model creation of the 3-panel structures for both the straight type and the inclined type.

For calculating the limit capacity surface, a number of loading patterns need to be analyzed. Each loading pattern—consisting of three resultant loads (F_Y, M_X, M_Z) applied

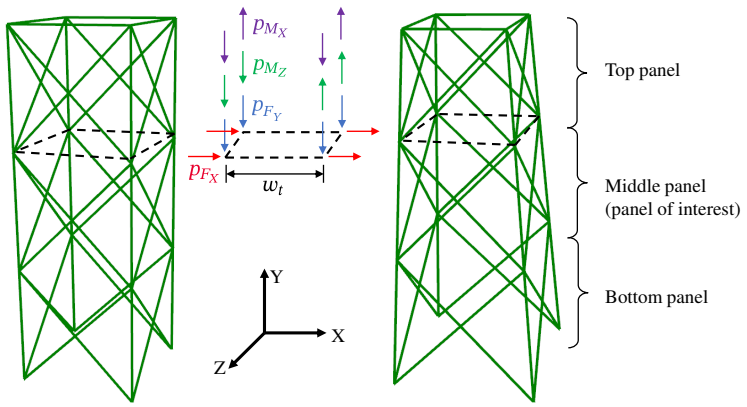

Figure 2.9: Illustration of the 3-panel structures and the load application: (a) straight type; (b) inclined type.

at the top of the middle panel—can be determined as follows:

$$F_Y = 4 \cdot p_{F_Y} = -P \tag{2.7}$$

$$M_X = 2 \cdot p_{M_X} \cdot w_t \tag{2.8}$$

$$M_Z = 2 \cdot p_{M_Z} \cdot w_t \tag{2.9}$$

where p_{F_Y}, p_{M_X}, and p_{M_Z} are the constituent nodal loads for F_Y, M_X, and M_Z respectively; and w_t is the top width of the middle panel. Applying the loads directly to the middle panel allows more convenient control for computing the failure surface. This results in low, though non-zero, stresses in the top panel because the structure is statically indeterminate. However, the top panel still serves a role in constraining the displacements of the middle panel. Note that the three resultant loads are constructed such that $F_Y \leqslant 0$, $M_X \geqslant 0$, and $M_Z \geqslant 0$ as per the coordinate system shown in Figure 2.9. Further, $P = -F_Y$ was introduced so that the limit capacity surface can be conveniently presented as non-negative (see Figure 2.8). Figure 2.10 gives the flowchart that can be used to compute the PMM limit capacity surface for a panel. This study used the displacement-controlled static analysis for all the load analyses mentioned therein. Note that the symmetry of the capacity surface

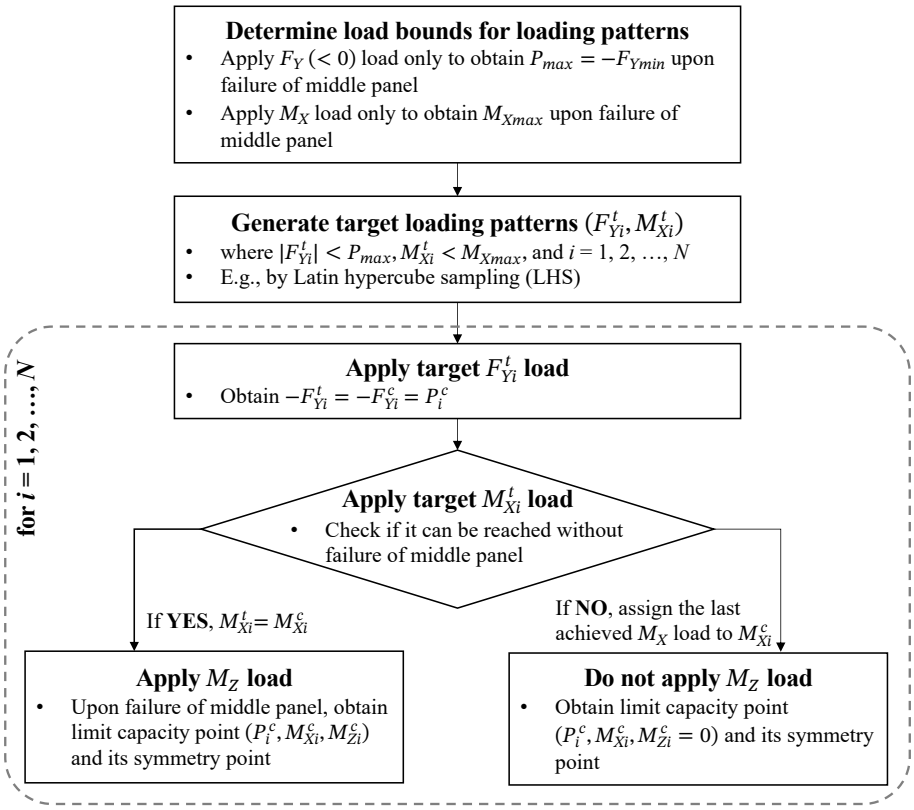

Figure 2.10: Flowchart for calculating the PMM limit capacity surface point by point. Superscripts *c* and *t* indicate capacity and target respectively.

(thanks to the symmetry of the panel) was leveraged in the process.

The PMM capacity surfaces for both straight and inclined panels were built point by point using the high-fidelity model, and their fit to planes was evaluated for accuracy (see Appendix B for details). The coefficients of determination (R^2) were found to be near 1, confirming that the limit capacity surfaces are well characterized by planes. Recognizing that $M_{X\max} = M_{Z\max}$, the PMM capacity plane can be fully defined by $P_{\max}$ and $M_{X\max}$, as follows:

$$\frac{P}{P_{\max}} + \frac{M_X}{M_{X\max}} + \frac{M_Z}{M_{X\max}} = 1 \tag{2.10}$$

A quantitative comparison study further reveals that significant discrepancies (exceeding 30%) in $P_{\max}$ and $M_{X\max}$ may arise when realistic beam-column behavior, connection effects, and member interactions are neglected (see Appendix B). Therefore, the high-fidelity

approach should be used as the basis for accurately determining $P_{\max}$ and $M_{X\max}$, as described in the first step of Figure 2.10. $P_{\max}$ and $M_{X\max}$ represent the panel-level loads at which individual legs reach their buckling capacity; this anchors the panel capacity plane in leg-level buckling. In the remainder of this chapter, the terms 'limit capacity surface' and 'limit capacity plane' are used interchangeably.

2.2.5 Proposed surrogate analytical model

As mentioned earlier, it is practically unfeasible to use the high-fidelity models for performing large-scale (e.g., thousands of towers) FE analysis. To begin with, the creation of the high-fidelity FE model for a transmission tower is rather time-consuming (at least multiple days) and the model is very computationally expensive to analyze (Ma et al., 2021a). This modeling approach is also too cumbersome to adapt for modeling the various structural configurations present in tower portfolios. Moreover, the complexity of the high-fidelity model, in terms of the nature (e.g., node location) and number of the input random parameters, makes it challenging to perform probabilistic simulations in a Monte Carlo fashion. For example, fragility models for bridge *classes* are typically derived leveraging FE models with a few dozen random variables (Karamlou and Bocchini, 2015; Padgett and DesRoches, 2007), whereas using the high-fidelity model for tower *class* fragilities would require sampling hundreds or thousands of random variables. This, in turn, hinders the advancement and diffusion of uncertainty modeling of tower portfolios. The PMM limit capacity model presented above enables the tower collapse failure analysis to be performed at the panel level. This section further proposes the panel-oriented surrogate analytical models for computing the desired EDPs. The mechanical behavior of panels under various sources of loads is first discussed (Section 2.2.5.1), following which Section 2.2.5.2 presents the formulation of the surrogate analytical model together with the calibration of the shear-related modeling parameter.

2.2.5.1 Mechanical behavior of panels

A self-supporting transmission tower behaves like a cantilever from the foundation. The forces transmitted from the upper tower to a panel can be calculated by equilibrium. As indicated in Figure 2.3c, these forces can be summarized as resultant forces acting through the centroid of the panel top. During wind events, the various sources of loads for the considered double-circuit towers are shown in Figure 2.11, and they include the loads transmitted from wires (i.e., conductors and overhead ground wires) and the loads directly applied on the tower body. The loads transmitted from the wires are usually represented as concentrated vector loads at the attachment points and can be decomposed into three components: vertical loads (L_V), transverse loads (L_T), and longitudinal loads (L_L). For tangent suspension towers—comprising almost 90% of the towers in transmission lines yet being most vulnerable to wind hazards—the longitudinal loads are negligible (Fang et al., 1997; Ma et al., 2021a). This is because the insulator strings can swing freely along the longitudinal direction and thus release the tower from the unequal tension (if any) in the two adjacent spans. In addition to the self-weight, the tower body is directly subjected to wind loads which are typically calculated at selected heights along the tower (see Figure 2.11) and applied as nodal loads in the transverse and longitudinal directions respectively (Dikshit and Alipour, 2023; Ma et al., 2021a). Depending on the direction of the wind loads, a panel may be under various combinations of axial, shear, bending and torsion loads.

Under the axial load and/or bending load, the behavior of the panel is governed by the four legs which are the primary resisting members (Wang et al., 2023). It is reasonable to assume that the axial load produces equal compression forces in four legs while the bending load produces equal compression in two legs on one side and equal tension in the other two legs. Past studies showed that little or no yielding of steel material may occur before the towers fail from buckling (Dikshit and Alipour, 2023; Mohammadi Darestani et al., 2020).

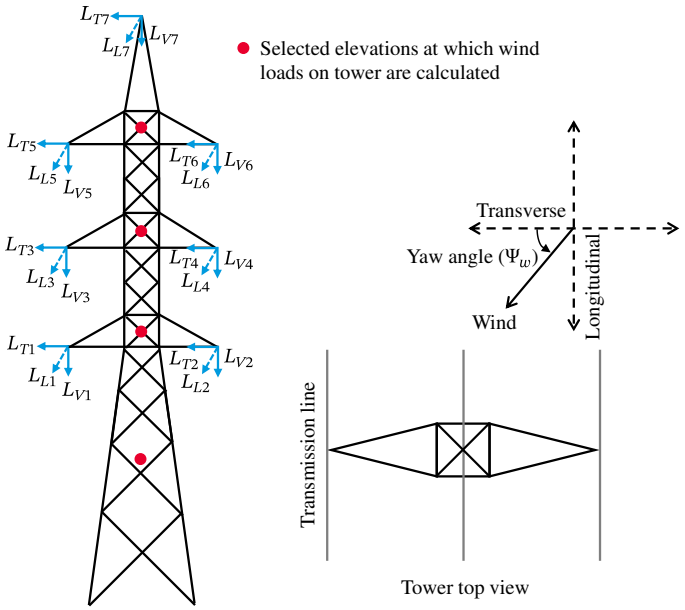

Figure 2.11: Illustration of the loads pertaining to a double-circuit tower.

Therefore, the legs and in turn the panel exhibit almost linear elastic behavior before the failure limit state of the panel.

Considerable shear loads on the panel can be generated by the transverse loads (L_T) transmitted from wires as well as the wind loads directly acting on the tower. The shear load is mainly carried by the diagonal bracings in the two faces that are parallel to the shear direction. The slippage at the bracing-to-leg connections can have an important impact on the shear behavior of the panel. Figure 2.12 shows two example shear load-displacement relationships obtained with the high-fidelity model for a straight panel and an inclined panel. With the 3-panel structure (see Figure 2.9), the shear resultant (F_X) was constructed from four nodal loads (p_{F_X}) and can be calculated as:

$$F_X = 4 \cdot p_{F_X} \tag{2.11}$$

The shear displacement ($\overline{U}_X$) for the middle panel (panel of interest) was determined as the difference between the average displacement of the top four nodes and the average displace-

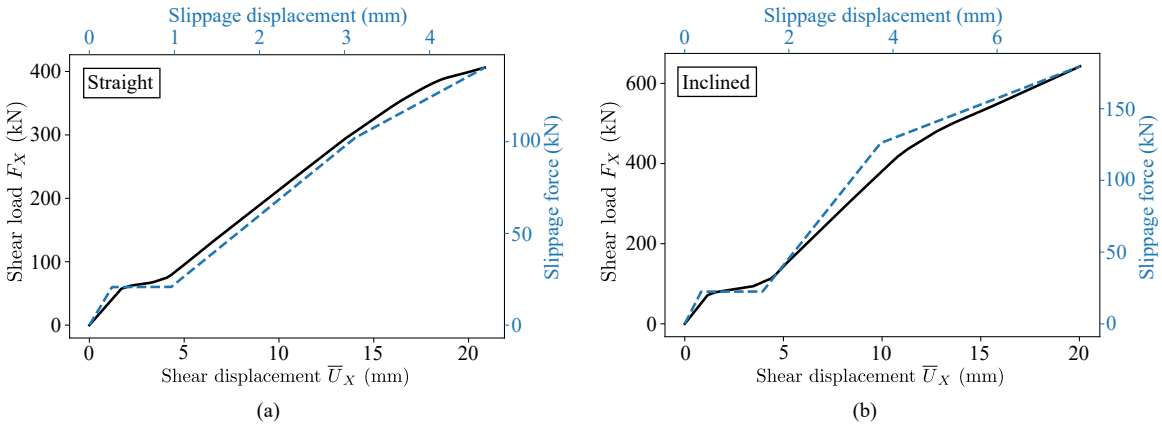

Figure 2.12: Shear load-displacement relationships and concurrent slippage responses: (a) straight type; (b) inclined type. Different slippage modeling parameters were used in the two example panels, hence the different slippage responses.

ment of the bottom four nodes. The shear load analysis was performed with displacement control until any connection associated with the middle panel reaches its maximum load capacity (i.e., point D in Figure 2.5b). It is evident from Figure 2.12 that the panel's shear behavior inherits the nonlinearity from the slippage response. It is worth noting that the joint slippage can increase the second-order P-Δ effect, especially at the tower level (Jiang et al., 2017), hence affecting the computed EDPs (PMM). In real transmission towers, joint slippage can occur at low load levels. In fact, most bolted joints in service function in the bolt bearing phase (i.e., Phase 3 in Figure 2.5b) (Ungkurapinan, 2000). Therefore, it is necessary to consider the slippage effect on the panel's shear behavior in the surrogate analytical model in order to compute the desired EDPs (PMM) accurately.

With the longitudinal loads (L_L) absent from the tangent suspension towers, torsional loads can only be generated by the yawed winds (i.e., $\Psi_w \neq 0^\circ$ or 90°) on the tower body, as shown in Figure 2.11. The torsional load is primarily carried by the bracings in all four faces of the panel. Similarly to the shear behavior, the torsional behavior of the panel is subject to the slippage effect at the bracing-to-leg connections. However, compared to the shear loads that are largely generated by the loads transmitted from the wires, the torsional loads (when present) are much smaller. Moreover, the panel's torsional rotation does not

meaningfully affect the considered EDPs (PMM). Thus, the panel's torsional behavior and the slippage impact therein are not as relevant in the formulation of the surrogate analytical model—this behavior can be approximated as linear.

2.2.5.2 Model formulation and parameter calibration

The formulation of the surrogate analytical model should incorporate the aforementioned mechanical behavior of the panels but also recognize that retaining all nonlinearities associated with the high-fidelity model offers little advantage in computing the desired EDPs. Therefore, this study proposes using one 3D shear deformable elastic beam-column element for surrogate modeling of one panel (straight or inclined). The proposed formulation can be implemented using existing elements available in OpenSees (McKenna et al., 2010) or any other finite element software. As shown in Figure 2.13, four modes of force-deformation responses are condensed into four corresponding stiffness parameters. Each force-deformation response refers to the sectional stress-strain resultant relationship of the corresponding mode. Note that the (surrogate) beam-column element section is only an abstract representation of the real panel section. The beam-column section is doubly symmetric (inherited from the actual panel) about the local y and z axes and yet amorphous. As mentioned in Section 2.2.5.1, panels exhibit almost linear elastic axial behavior thanks to the negligible material nonlinearity before panel failure. Therefore, the sectional axial force-deformation response can be taken as linear elastic, and the sectional axial stiffness (K_{sa}) for both panel types can be obtained by:

$$K_{sa} = EA = E \cdot 4 \cdot A_{\text{leg}} \tag{2.12}$$

where A represents the area of the abstract section and is calculated as the sum of the sectional areas of the four corner legs (A_{leg}).

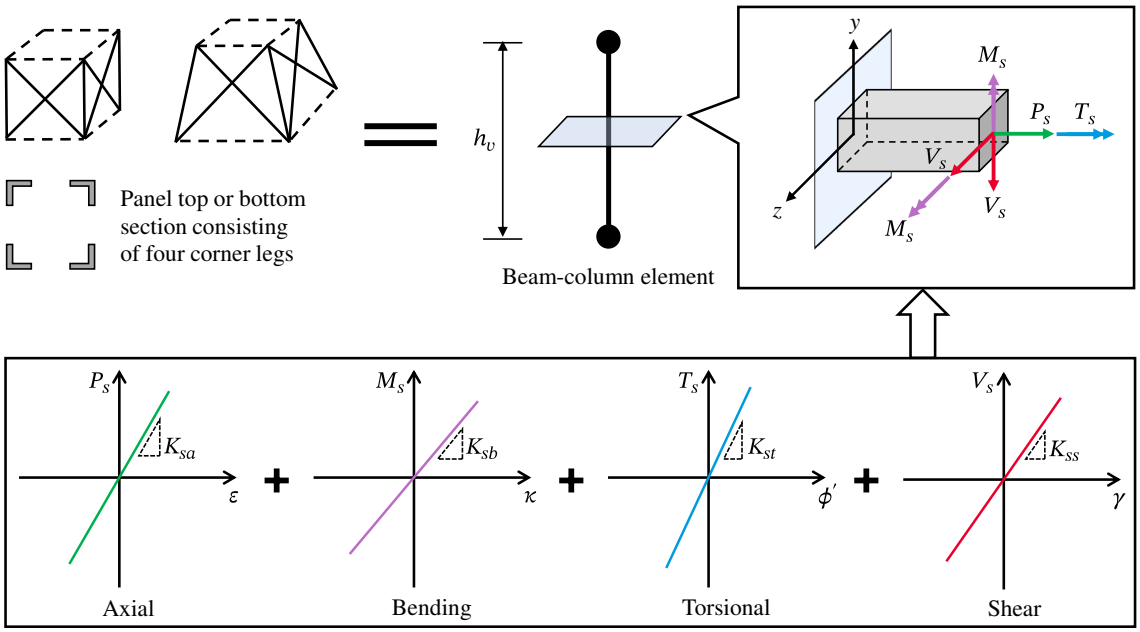

Figure 2.13: Proposed formulation of the surrogate analytical model.

Similarly, the panel's bending behavior is also close to linear elastic until failure, and it is governed by the four legs. The sectional bending stiffness (K_{sb}) can be computed by Equations (2.13)-(2.15):

$$K_{sb} = EI = E \cdot \frac{I_t + I_b}{2} \tag{2.13}$$

$$I_t = 4 \cdot \left[I_{\text{leg}} + A_{\text{leg}} \left(\frac{w_t}{2} \right)^2 \right] \tag{2.14}$$

$$I_b = 4 \cdot \left[I_{\text{leg}} + A_{\text{leg}} \left(\frac{w_b}{2} \right)^2 \right] \tag{2.15}$$

where I is the second moment of area of the abstract section and is calculated as the average of I_t and I_b; I_t and I_b are respectively the second moments of area of the panel top section and the panel bottom section (see Figure 2.13), both of which are determined using the parallel-axis theorem; and I_{leg} is the second moment of area of a single leg section. Note that $I_b = I_t$ for panels of the straight type, since $w_t = w_b$.

Although the panel's torsional behavior is not as relevant in computing the desired EDPs (PMM), a torsional stiffness is required by the 3D formulation in order to prevent

the local rigid-body spinning. To this end, the linear elastic torsional force-deformation response was adopted in this study. Assuming that the torsional stiffness is exclusively provided by the diagonal bracings, the sectional torsional stiffness (K_{st}) for both panel types can be calculated by the following equations (Tabet, 2009):

$$K_{st} = GJ = E \cdot A_{\text{brace}} \cdot \sqrt{2} \frac{w_{\text{avg}}^4 \cdot h_v}{\left(\sqrt{w_{\text{avg}}^2 + h_v^2}\right)^3} \tag{2.16}$$

$$w_{\text{avg}} = \frac{w_t + w_b}{2} \tag{2.17}$$

where G is the shear modulus of the steel material and can be taken as 77 GPa; J is the torsional moment of inertia of the abstract section; A_{brace} is the sectional area of a single bracing; and w_{avg} is the average width of the panel.

To account for the nonlinear slippage effect on the panel's shear behavior, a calibration procedure was employed herein for determining the sectional shear force-deformation response, as shown in Figure 2.14. Although the shape of the panel's shear load (F_X)-displacement ($\overline{U}_X$) relationship resembles that of the slippage response, the former does not show four phases as clearly as the latter (see Figure 2.12). In fact, the slippage modeling parameters bear considerable variations, as will be discussed in Section 2.3.1. As a consequence, the F_X-$\overline{U}_X$ relationships lack a standard shape, which poses a big challenge for calibration. With the proposed surrogate model formulation, this study adopted a simplified linear elastic shear force-deformation response, where the sectional shear stiffness (K_{ss}) was calibrated based on one target point on the F_X-$\overline{U}_X$ relationship. The specified calibration target ($\overline{U}_X^t$, F_X^t) is the transition point at the onset of the last nonlinear segment of the shear relationship, as illustrated in Figure 2.14. This target point was selected because it approximately corresponds to the end of the bolt bearing phase which most bolted joints function in (Ungkurapinan, 2000). In this way, the calibrated K_{ss} is close to the true value achieved when the panel starts approaching failure. The resulting linear shear

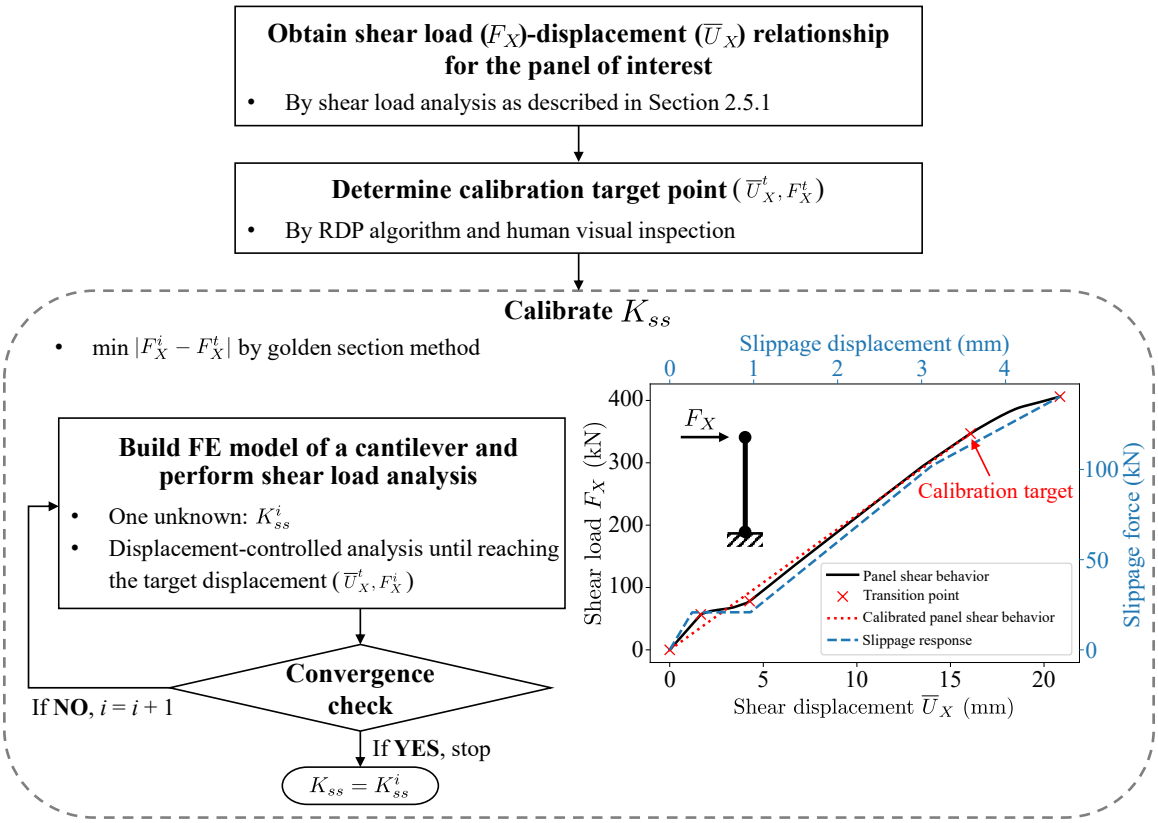

Figure 2.14: Calibration procedure for determining K_{ss}.

relationship is overall close to the actual nonlinear shear relationship. To determine the calibration target point for an F_X-$\overline{U}_X$ relationship, several transition points (typically two to five points) were first identified via the Ramer-Douglas-Peucker (RDP) algorithm (Douglas and Peucker, 1973). Then the correct transition point (as defined above) was manually selected by visual inspection. As shown in Figure 2.14, a cantilever implemented with the proposed surrogate model formulation was utilized to calibrate the K_{ss} (the only unknown), for which the golden section method was employed. As will be explained in Section 2.3, the results of this calibration were used only to train the metamodel that is provided as one of the main outcomes of this study, and analysts will not need to repeat the manual procedure for this class of towers in the future.

In summary, the four stiffness parameters are rigorously anchored in the panel's mechanical behavior with careful simplifications and assumptions. Despite its linear element

formulation, the surrogate model is specifically calibrated to capture two key aspects of the nonlinear responses of transmission towers. First, the shear stiffness parameters are calibrated to optimally balance the pre- and post-slippage stiffness. Second, the panel capacity is calibrated to detect any combination of axial force and bending moments (PMM) that would lead to leg instability in the high-fidelity model. Thus, the proposed surrogate is not a simplistic linearization that disregards the nonlinear portion of the response; rather, it is a linear model calibrated to closely approximate the essential nonlinear features. Most importantly, it captures the leg buckling failure through a PMM capacity surface that is calibrated using a fully nonlinear reference model. A validation study demonstrating the performance of the proposed surrogate model is presented in Section 2.5.

2.3 Metamodel for consistent capacity and demand simulation

Section 2.2 addresses the first part of the proposed framework for portfolio analysis of transmission towers—establishing the PMM capacity plane model and the surrogate analytical model for the abstracted two types of panel components. This section focuses on the development of a metamodel which is motivated by the need of consistent simulation of panel capacity and demand. At the component level, the component's response (or demand placed on it) should be compared with its capacity for assessing the component damage, which can then be translated into the damage of the overall structural system. While the components' responses usually come from the FE analysis, the components' capacities may be obtained by two approaches. The first approach is to sample the components' capacities from separately prescribed (joint) probability distributions. For example, capacity estimates were introduced for bridge components based on experimental results, surveys, and assumptions (Nielson, 2005; Padgett, 2007). The second approach is to more rigorously

compute the components' capacities as a function of relevant structural parameters.

For the abstracted panel components, the first approach is hampered by the lack of data to characterize the panels' limit capacity surfaces, specifically $P_{\max}$ and $M_{X\max}$ as per Equation (2.10). Moreover, in the context of portfolios of towers, each of the two types of panels exhibits considerable variations (recall Section 2.2.2), and in turn the range of the panel capacities can be very large. In this case, independent sampling of the panel capacity without reconciling the underlying panel modeling parameters is likely to lead to unrealistic demand-capacity pairs and thus misleading analysis results. In fact, the same two issues are also faced when defining the panel surrogate modeling parameters (i.e., K_{sa}, K_{sb}, K_{st}, K_{ss}). Therefore, a procedure is needed for the consistent probabilistic simulation of panel capacity and demand instead of treating them separately. To this end, this study adopted the second approach and introduced a dual-purpose metamodel. Specifically, the same set of random samples for basic structural properties is used to compute both the panel capacity and the surrogate modeling parameters, which guarantees the consistency of panel demand-capacity pairs. The metamodel can be mathematically represented as:

$$\hat{Y} = f(\boldsymbol{X}) \tag{2.18}$$

where $\hat{Y}$ is the prediction of the metamodel, which can be a parameter of the limit capacity surface of the panel or of the surrogate analytical model; $\boldsymbol{X}$ represents a vector of structural input parameters. For practical purposes, two versions of the model have been calibrated: f_{str} for straight panels and f_{inc} for inclined panels. When not specified, f will indicate both models in the remainder of the text. The development of the metamodel is detailed in the following two subsections.

2.3.1 Design of experiments

Based on the panel variations discussed in Section 2.2.2, this study considered 11 input variables for training the metamodel, as shown in Table 2.1. Encompassing both macro- and micro-levels, these input variables were selected because they capture the most important factors determining the panel capacity and demand. To generate data for training the metamodel, a sampling protocol or design of experiments (DoE) is typically used. The Latin hypercube sampling (LHS) technique was employed herein to strategically cover the design space, and the *SMT* Python library was utilized to handle the mixed-variable sampling (Saves et al., 2024). The ranges of the 11 variables that were used to generate the training data are also provided in Table 2.1. Note that the two types of panels are associated with different ranges for w_t, while they share the same ranges for the other variables. The ranges of w_t cover the vast majority of the panels that can be found in real transmission towers. Variables s_{leg} and s_{brace} are integers representing standardized angle sections, which are sorted in ascending order by sectional area (see Table A.1). Bolted connections can vary in terms of bolt count and clearance levels, leading to differing slippage response curves. The force and displacement values at the controlling points of these curves (see points A to D in Figure 2.5b) are the variables determining the connection behavior, as given in Table 2.1 (Mohammadi Darestani et al., 2020; Ungkurapinan, 2000). For the six parameters that follow lognormal distributions, the minimum and maximum values were calculated as the inverse cumulative distribution function (CDF) at probabilities of 1% and 99%, respectively. Concerning the ASTM A36 steel that dominates the transmission tower inventory of the United States, the range of its yield stress was similarly defined by the inverse CDF at probabilities of 1% and 99%.

Table 2.1: Variables and associated ranges used in the DoE.

Variable	Description	Type	Minimum	Maximum	Notes
Geometry					
w_t	Panel top width (mm)	Continuous	1000.0 (straight), 1000.0 (inclined)	2500.0 (straight), 5820.0 (inclined)	Type-dependent
Size					
s_{leg}	Angle size of legs	Discrete	1	51	See Table A.1
s_{brace}	Angle size of bracings	Discrete	1	51	See Table A.1
Connection					
Force @ A	Load at onset of slip (kN)	Continuous	11.89	32.55	$LN(20.14, 4.41)$
Force @ C	Load at onset of plasticity (kN)	Continuous	74.20	126.47	$LN(97.51, 11.21)$
Force @ D	Maximum load (kN)	Continuous	136.28	181.81	$LN(157.71, 9.78)$
Phase 1	Displacement at elastic frictional load transfer (mm)	Continuous	0.13	0.44	$LN(0.25, 0.065)$
Phase 2	Slippage length (mm)	Continuous	0.31	2.33	$U(1.32, 0.58)$
Phase 3	Displacement at elastic load transfer (mm)	Continuous	1.01	2.83	$LN(1.73, 0.39)$
Phase 4	Displacement at nonlinear load transfer (mm)	Continuous	1.45	4.26	$LN(2.55, 0.60)$
Material					
F_y	Yield stress (MPa)	Continuous	228.80	363.93	$LN(290.0, 29.0)$

Note: LN = lognormal (mean, standard deviation); U = uniform (mean, standard deviation).

2.3.2 Polynomial response surface metamodel

For each sample realization of the 11 input variables of a given panel type, the 3-panel structure was designed via the panel design routine described in Figure 2.6 and Section 2.2.4. Samples resulting in non-permissible designs were discarded, while high-fidelity FE models were automatically created for the remaining valid designs. With the high-fidelity model, the PMM limit capacity surface was obtained as described in Section 2.2.4, and the modeling parameters of the surrogate analytical model were derived using the method presented in Section 2.2.5.2.

The proposed metamodel takes the form of a second-order polynomial response surface for each output quantity $\hat{Y}$, which was selected for its interpretability, efficiency, and accessibility. To limit complexity and prevent overfitting, the number of input parameters for the metamodel should be kept small. More importantly, when using the metamodel for probabilistic simulations, samples of its input parameters need to be generated. If this number is too large, the benefits of using the metamodel and the surrogate panel model would be negated in comparison to using the high-fidelity model. For the purpose of feature selection, a sensitivity analysis was first conducted to rank the importance of all 11 input variables. Based on this ranking, the number of input features was varied (e.g., top four, five, or six), and the resulting metamodels were evaluated in terms of accuracy and complexity. It was found that using the top five features provided overall the best trade-off between predictive performance and model complexity.

Therefore, this study pre-selected five input parameters (out of 11) for metamodel fitting: the panel top width (w_t, unit: mm), the sectional area of legs (A_{leg}, unit: mm^2), the sectional area of bracings (A_{brace}, unit: mm^2), the slippage length or Phase 2 (l_{slip}, unit: mm), and the yield stress of ASTM A36 steel (F_y, unit: MPa). These parameters cover all four aspects of the DoE (see Table 2.1). The top width captures the overall geomet-

ric size of the panel. The indices of angle sections (s_{leg}, s_{brace})—previously mentioned in Section 2.3.1—are replaced here with the corresponding angle areas (A_{leg}, A_{brace}) because the area is physically meaningful and can better inform the metamodel. Out of the seven slippage modeling parameters, only the slippage length was selected; it has the most important effect on the nonlinear shear behavior of the panel and bears the largest dispersion (coefficient of variation = 0.44). Finally, F_y directly captures the material's influence on the capacity of the panel. Upon knowing w_t, A_{leg}, and A_{brace}, three stiffness parameters of the surrogate analytical model—K_{sa}, K_{sb}, and K_{st}—can be readily calculated by Equations (2.12), (2.13), and (2.16). Therefore, only the K_{ss} needs to be provided by the metamodel to fully characterize the surrogate panel model for demand analysis. The input vector ($\boldsymbol{X}$) of the metamodel and the quadratically expanded predictor space ($\boldsymbol{X}'$) are expressed as follows:

$$\boldsymbol{X} = [w_t, A_{\text{leg}}, A_{\text{brace}}, l_{\text{slip}}, F_y] \tag{2.19}$$

$$\begin{aligned}\boldsymbol{X}' = [&w_t, A_{\text{leg}}, A_{\text{brace}}, l_{\text{slip}}, F_y, w_t A_{\text{leg}}, w_t A_{\text{brace}}, w_t l_{\text{slip}}, w_t F_y, A_{\text{leg}} A_{\text{brace}}, A_{\text{leg}} l_{\text{slip}}, A_{\text{leg}} F_y,\\ &A_{\text{brace}} l_{\text{slip}}, A_{\text{brace}} F_y, l_{\text{slip}} F_y, w_t^2, A_{\text{leg}}^2, A_{\text{brace}}^2, l_{\text{slip}}^2, F_y^2]\end{aligned} \tag{2.20}$$

As customary, the original representation of the predictors (as given in $\boldsymbol{X}'$) was standardized before performing the regression analysis. For each predictor, the centering and scaling is given by:

$$Z_j = \frac{X_j' - \mu_j}{\sigma_j} \tag{2.21}$$

where Z_j is the j^{th} standardized predictor; X_j' is the j^{th} original predictor in $\boldsymbol{X}'$; μ_j and σ_j are the mean and standard deviation of X_j' and can be calculated from the samples. The standardized predictors Z_j can be collected in vector $\boldsymbol{Z}$. The polynomial response surface

metamodel in terms of the standardized predictors is now written as:

$$\hat{Y} \in [P_{\max}, M_{X\max}, K_{ss}] = f(\boldsymbol{X}) = \theta_0 + \sum_{j=1}^{n=20} \theta_j Z_j \tag{2.22}$$

where $\boldsymbol{\theta} = [\theta_0, \theta_1, \ldots, \theta_n]$ is the coefficient vector. In summary, for consistent simulation of the panel capacity and demand, the metamodel prediction ($\hat{Y}$) is one of three quantities: $P_{\max}$ and $M_{X\max}$ for determining the PMM limit capacity plane, and K_{ss} for surrogate modeling of the panel. In total, six sets of coefficients ($\boldsymbol{\theta}$) need to be learnt for the two types of panels.

Finally, ridge regression was employed for fitting the metamodel, because it can handle robustly the pairwise correlation between predictors and affords the minimum variance in the resulting coefficient estimates (Hoerl and Kennard, 2000; Misra and Padgett, 2019). To determine the best value of the regularization parameter (α)—a hyperparameter of the ridge regression encoding the regularization strength—the common practice is to apply cross-validation. In this study, the leave-one-out cross-validation was performed on the training dataset to search the optimum α within the range of $[10^{-10}, 10^{10}]$; the best model was selected using the coefficient of determination (R^2) as the scoring parameter. The performance of the model was then evaluated on the previously unseen testing dataset. The obtained metamodel and the associated evaluation are presented in Section 2.4.

2.4 Results of the metamodel

With the DoE scheme described in Section 2.3.1, large batches of FE analyses were carried out to generate sample data for training the polynomial response surface metamodel. To achieve stability in the metamodel forms, a convergence study was performed by generating a series of panel samples of increasing sample sizes (i.e., $100, 200, \ldots$), where each sample realization comprises 11 input variables for a given panel type. A sample size of 500 was

Table 2.2: Metamodel training setup and results.

Type	Purpose	$\hat{Y}$	Sample size	Optimum α	R^2 on training set	R^2 on testing set
Straight	Capacity	$P_{\max}$	500	0.1	0.993	0.987
		$M_{X\max}$	500	0.1	0.990	0.985
	Demand	K_{ss}	500	1.0	0.855	0.858
Inclined	Capacity	$P_{\max}$	483	1.0	0.964	0.965
		$M_{X\max}$	483	1.0	0.901	0.904
	Demand	K_{ss}	483	1.0	0.866	0.862

Note: The training-testing split is set at $75\% - 25\%$.

found sufficient for both types of panels. Table 2.2 summarizes the setup for the metamodel training and some key results. For the inclined type, 17 samples led to non-permissible panel designs and were disregarded; hence the sample size is 483.

To shed further light on the panel capacities and shear stiffnesses, the sample data used for metamodel training are presented in Figure 2.15 using swarm and violin plots. The figure shows that the ranges of $P_{\max}$, $M_{X\max}$, and K_{ss} observed for all sample cases are very large for both types of panels. This confirms that, for either panel type, independent sampling on these ranges is likely to lead to unreasonable tower models and unrealistic panel demand-capacity pairs. As mentioned, the use of the proposed metamodel provides the necessary consistent simulation of panel capacity and demand. It is important to note that the panel samples were strategically generated to cover the design space for better informing the metamodel. As a result, the sample sets of $P_{\max}$, $M_{X\max}$, and K_{ss} are not necessarily representative of their realistic distributions. To obtain the realistic distributions or statistics of component modeling parameters and capacities, detailed inventory data or comprehensive experimental data are required (Misra and Padgett, 2019; Nielson, 2005). The datasets (i.e., characteristics of the sample panels and associated sample capacity and stiffness) are portfolio-agnostic, so is the derived metamodel. The metamodel is effectively applicable to any panel of either type within the scope defined by Table 2.1; thus, tower design requirements can be easily incorporated afterwards for the purpose of generating

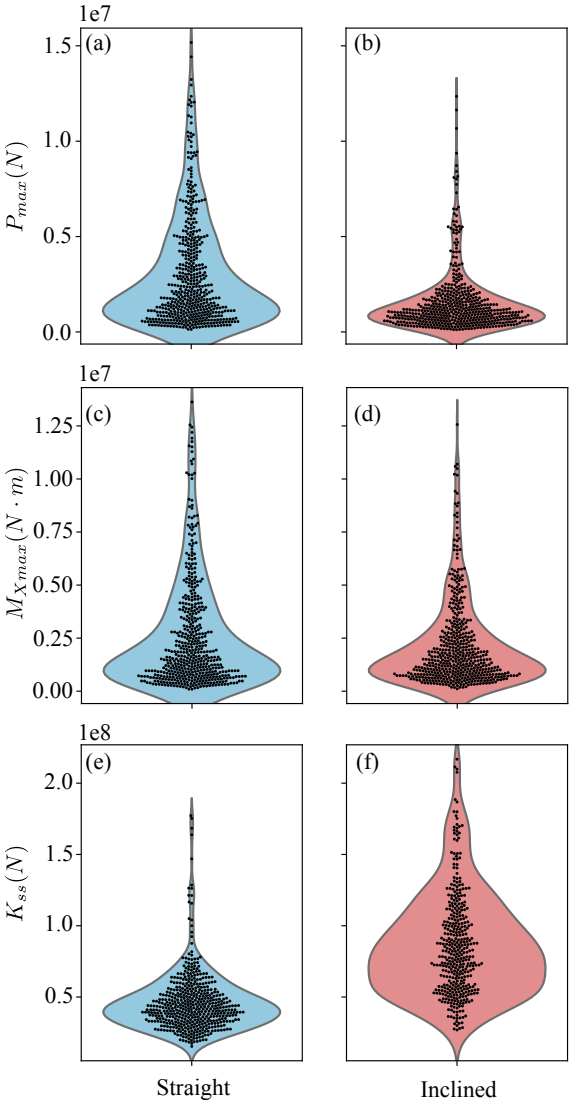

Figure 2.15: Sample data used for training the metamodel: (a) straight, $P_{\max}$; (b) inclined, $P_{\max}$; (c) straight, $M_{X\max}$; (d) inclined, $M_{X\max}$; (e) straight, K_{ss}; (f) inclined, K_{ss}. Each black dot in the swarm plot represents a sample. The width of the violin is proportional to the probability density at a certain value of the vertical variable, as estimated by kernel smoothing.

realistic tower models, such as for the second and third use cases in Figure 2.1.

The six sets of coefficients calibrated for the metamodel in Equation (2.22) are presented in Appendix C. With only five structural input parameters (w_t, A_{leg}, A_{brace}, l_{slip}, F_y), the response surface metamodel, in place of the high-fidelity FE model, can be used to compute $P_{\max}$ and $M_{X\max}$ (for determining the PMM limit capacity plane) and K_{ss} (for surrogate modeling of the panel) efficiently and consistently. To evaluate the performance of the metamodel, a metric must be selected, such as the coefficient of determination (R^2) or root mean squared error (RMSE). This study adopted R^2—indicating the proportion of explained variance—because it is more informative and does not have the interpretability limitations present in other metrics (Chicco et al., 2021). For better and intuitive understanding, Figure 2.16 shows the predicted values versus the actual values (on the testing set only) as well as the R^2 scores on both the training set and testing set. The diagonal line represents the ideal case when the predicted value is equal to the actual value. As observed from Figure 2.16a-d, the metamodel has good accuracy in the capacity prediction for both types of panels. In addition, the R^2 scores on the training and testing sets are close, which means that the metamodel does not suffer from overfitting.

In comparison, the metamodel shows somewhat lower accuracy in the K_{ss} prediction (see Table 2.2 and Figure 2.16e-f). It is tempting to attribute the lower accuracy to the choice of only including the slippage length (out of seven slippage modeling parameters) in the input parameters ($\boldsymbol{X}$). However, a test analysis incorporating one additional slippage modeling parameter (i.e., adding Force @ A, Force @ C, Force @ D, Phase 1, Phase 3, or Phase 4 one at a time, as defined in Table 2.1) showed an insignificant improvement in accuracy for K_{ss} prediction, with the best achieved $R^2 = 0.877$. In fact, unlike the $P_{\max}$ and $M_{X\max}$ samples, the K_{ss} samples were obtained via an additional calibration procedure (see Figure 2.14), which introduced some noise into the fitting. The accuracy of K_{ss} prediction is possibly constrained by the inherent limitations of a second-order polynomial response

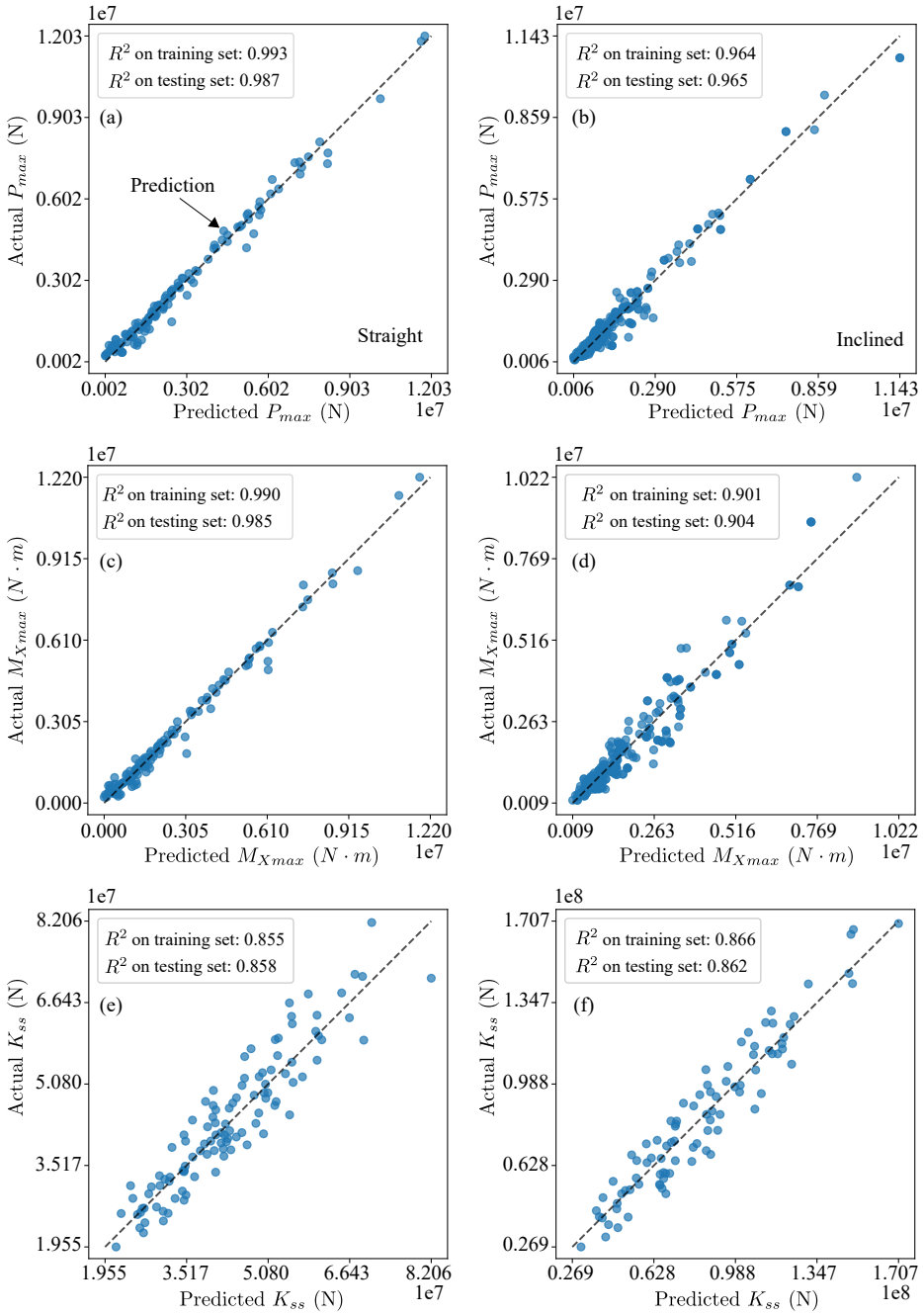

Figure 2.16: Performance evaluation of the metamodel: (a) straight, $P_{\max}$; (b) inclined, $P_{\max}$; (c) straight, $M_{X\max}$; (d) inclined, $M_{X\max}$; (e) straight, K_{ss}; (f) inclined, K_{ss}.

surface metamodel. Given that the accuracy gain from adding one more parameter is not justified by the cost (seven additional terms in the metamodel), the use of five input parameters is preferred and upheld. While the R^2 scores for the K_{ss} prediction are less ideal than those for $P_{\max}$ and $M_{X\max}$, they are still considered acceptable based on similar work

in the field (Misra and Padgett, 2019; Segura et al., 2020). Essentially, the shear behavior described by K_{ss} influences the desired EDPs (PMM) indirectly (see Section 2.2.5.1). When assessing the metamodel's performance in a broader context, such as portfolio analysis, the prediction error becomes negligible compared to other prevalent sources of error or uncertainty (e.g., load uncertainty, structure-to-structure uncertainty). In conclusion, the developed metamodel demonstrates sufficient accuracy for simulating the capacity and demand of both types of panels.

2.5 Validation and application

To perform tower failure analysis at the 'panel component' level, the demand placed on each panel (or panel response) should be compared to its limit capacity. The panel failure LS function can be expressed as:

$$\ell_i = P_{PMM_i}(M_{X,i}, M_{Z,i}) - P_i \tag{2.23}$$

where $i = 1, 2, \ldots, k$ for a tower consisting of k panels; $P_{PMM_i}(M_{X,i}, M_{Z,i})$ represents the axial force capacity of panel i, as determined from the PMM limit capacity plane under the bending moments $M_{X,i}$ and $M_{Z,i}$; and P_i denotes the axial force demand on panel i. For a given panel, the metamodel can be used to obtain its PMM limit capacity plane and the modeling parameter K_{ss} consistently. The demand is computed through FE analysis using the proposed surrogate analytical model. The panel-oriented surrogate modeling concept and formulation are rigorously developed based on the mechanical behavior of the panels. However, in view of the assumptions and simplifications introduced therein, the accuracy of the surrogate analytical model in computing the desired EDPs (PMM) needs to be assessed. Some notable assumptions and simplifications include the estimation of parameters such as K_{sa}, K_{sb}, and K_{st}; the calibration of parameter K_{ss}; and the formulation and implementation

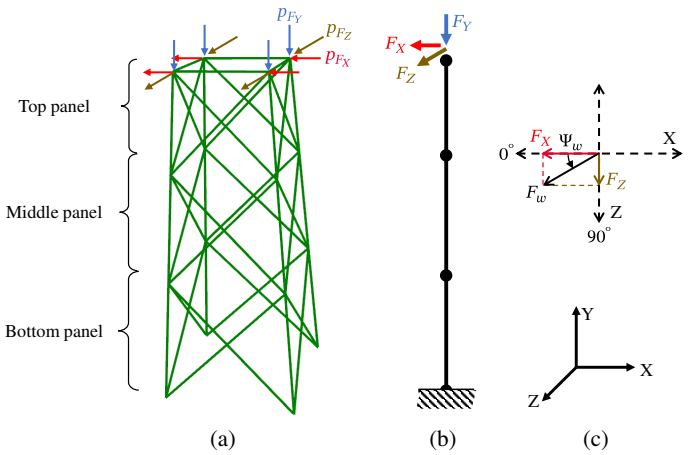

Figure 2.17: Validation setup illustrated with a 3-panel structure of the inclined type: (a) high-fidelity model; (b) surrogate model; (c) decomposition of yawed wind loads.

of the beam-column element. Therefore, a numerical validation campaign was conducted for both types of panels using 3-panel structures (Section 2.5.1). Then, fragility curves for a full tower were derived using both the high-fidelity model and the surrogate model to examine discrepancies in the fragility assessment (Section 2.5.2).

2.5.1 Validation by 3-panel structures

As illustrated in Figure 2.17, this part utilized 3-panel structures, where the middle panel was considered for accuracy assessment while the top and bottom panels served to diffuse the load and constraint effects, respectively. The high-fidelity model (Figure 2.17a) was used as the benchmark for the surrogate model (Figure 2.17b) that consists of three beam-column elements. To mimic the case of yawed wind load (F_w), four different wind directions were considered (i.e., $\Psi_w = 0°, 15°, 30°, 45°$), as shown in Figure 2.17c. A vertical load (F_Y) was included and was set to $-\frac{1}{2}P_{\max}$ of the middle panel. The vertical and horizontal loads were applied to the top node of the surrogate model and split evenly among the top four nodes of the high-fidelity model ($F_X = 4 \cdot p_{F_X}$, $F_Y = 4 \cdot p_{F_Y}$, $F_Z = 4 \cdot p_{F_Z}$). Note that, for fair comparison of the computational efficiency, displacement control (displacement increment = 0.001 mm) was used in the wind load analysis for both the surrogate

model and the high-fidelity model. However, the former has the potential to achieve faster performance because it can remain numerically stable even with large displacement or load increments. Specifically, the validation analysis can be described as four logical steps:

1. Sample panels and create FE models: with the DoE scheme presented in Section 2.3.1, 50 middle panels were sampled for each panel type. For each permissible middle panel (50 for the straight type while 49 for the inclined type), a high-fidelity model and a surrogate model were created for the corresponding 3-panel structure. In particular, the metamodel derived in Section 2.4 was utilized to obtain the surrogate modeling parameter K_{ss} and the PMM limit capacity plane (essentially $P_{\max}$ and $M_{X\max}$) for each panel.

2. Perform FE analysis for the surrogate model: the vertical load F_Y was first applied and held constant. Then, depending on the considered wind direction, the yawed wind load (i.e., F_X and F_Z) was applied incrementally while the failure assessment was performed for all three panels in the structure. The analysis stopped upon the failure of any of the three panels and the achieved load level $(F_X, F_Y, F_Z)_f$ was recorded.

3. Perform FE analysis for the high-fidelity model: the same load level $(F_X, F_Y, F_Z)_f$ was reached by first applying the vertical load F_Y and then the yawed wind load.

4. Postprocess the structural responses and compare: in addition to the EDPs (PMM), the displacement responses (U_X, U_Y, U_Z) and computation time were also investigated. For the surrogate model, the EDPs (PMM) and displacement responses can be easily retrieved from the element responses since a single element models one panel. For the high-fidelity model, the EDPs (PMM) with respect to a panel were calculated as the resultant forces acting through the centroid of the panel top using the relevant element responses. The displacement responses were calculated as the average

of the nodal displacements at the panel top. Lastly, focusing on the final state—corresponding to the load level $(F_X, F_Y, F_Z)_f$—the EDPs and displacement responses given by the high-fidelity model and the surrogate model were compared.

Although the main goal is to validate the accuracy of the surrogate analytical model in computing the EDPs (PMM), this global validation process serves also for the validation of the metamodel used in Step 1. This is because the panels within the 99 3-panel structures were unseen by the metamodel (derived using a sample size of 500). Therefore, the results and accuracy of the surrogate model should be interpreted considering these coupled effects. A total of 50 straight-type 3-panel structures and 49 inclined-type 3-panel structures were analyzed across four wind directions, using both the high-fidelity and surrogate models. All numerical analyses were completed using a desktop computer (CPU type: Intel Xeon CPU E5-1620 v3 @ 3.50 GHz, RAM: 32.0 GB). Figure 2.18 compares the computation time between the high-fidelity model and the surrogate model, where each box plot mixes the two panel types and the four wind directions. The computation time shown in the figure includes the time for FE model creation (Step 1) and for FE analysis (Step 2 or 3). However, the model creation is automated and takes almost negligible time, so the time primarily reflects the FE analysis complexity. Figure 2.18a-b show that the high-fidelity models take much more computation time (mean = 42.0 minutes, median = 19.3 minutes) than the surrogate models (mean = 1.4 minutes, median = 0.7 minutes). Overall, the surrogate models are more than 20 times faster than the high-fidelity models, as shown by the pair-wise time ratio (mean = 26.1, median = 22.6) in Figure 2.18c.

Figure 2.19 compares the structural responses computed by the high-fidelity model and the surrogate model for two example 3-panel structures: one straight-type and one inclined-type. For the two examples shown, the surrogate model presents very good accuracy in both the EDPs and displacement responses compared to the high-fidelity model. Similar results were observed for the other sample structures. Finally, Figure 2.20 summarizes the results

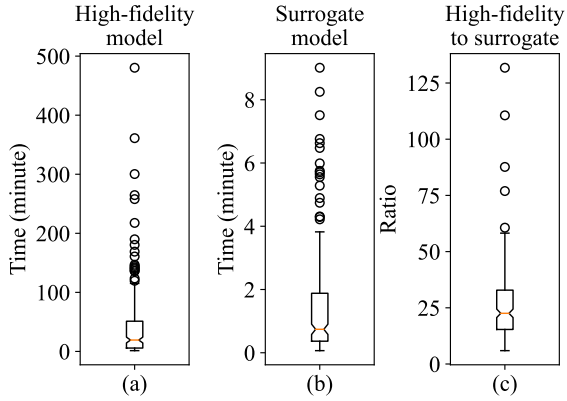

Figure 2.18: Comparison of computation time: (a) high-fidelity model; (b) surrogate model; (c) time ratio between the high-fidelity model and the surrogate model.

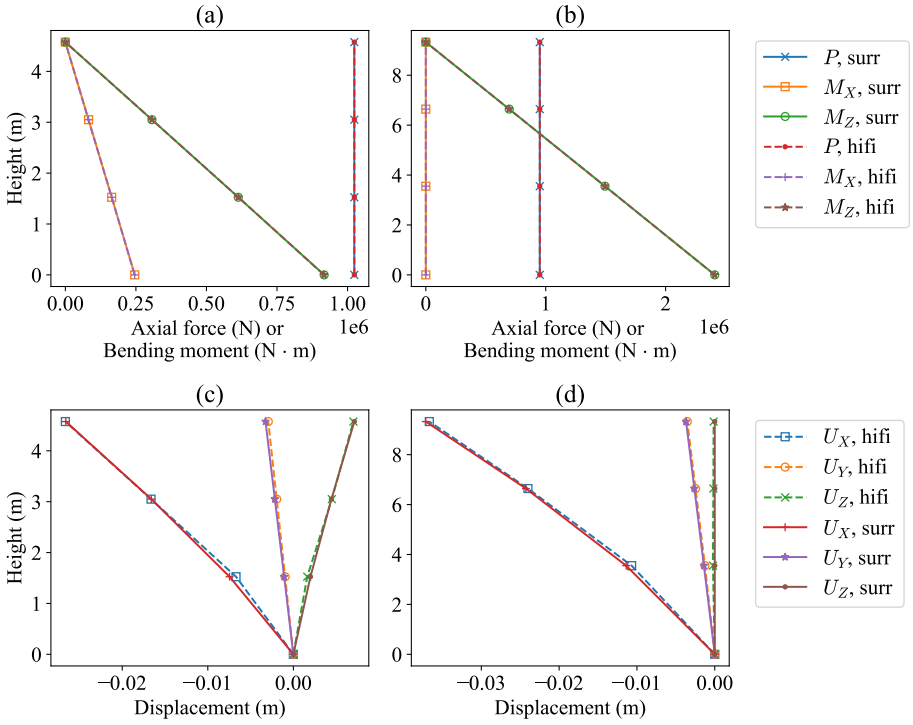

Figure 2.19: Example comparison of 3-panel structural responses: (a) force and (c) displacement responses of straight panels with $\Psi_w = 15°$; (b) force and (d) displacement responses of inclined panels with $\Psi_w = 0°$. The 'hifi' and 'surr' are shorthand for high-fidelity and surrogate respectively.

of all validation analyses in terms of the percentage difference which is determined as:

$$\text{Percentage difference} = \frac{|r_{\text{surr}} - r_{\text{hifi}}|}{|r_{\text{hifi}}|} \cdot 100\% \tag{2.24}$$

where r_{surr} is the structural response (i.e., P, M_X, M_Z, U_X, U_Y, U_Z) from the surrogate model; and r_{hifi} is the corresponding response from the high-fidelity model. The results shown in Figure 2.20 are for the middle panels only whose boundary conditions are best represented. The percentage difference in the EDPs is illustrated by box plots; the percentage difference in the displacement responses is illustrated by the violin plots and swarm plots, where the hues of the dots are mapped with the absolute values of the corresponding high-fidelity displacement responses (see the legend). Each plot aggregates both panel types and the four wind directions while the last plot further combines the results of the two lateral displacement responses.

The percentage difference in the EDPs is negligibly small: for P, mean = 0.016%, median = 0.013%; for M_X, mean = 0.83%, median = 0.74%; and for M_Z, mean = 0.47%, median = 0.31%. The percentage difference in the displacement responses shows slightly larger magnitude and dispersion: for U_Y, mean = 2.73%, median = 2.57%; for U_X and U_Z, mean = 4.17%, median = 3.25%. The larger discrepancies occur in cases where the displacements are very small, as indicated by the colors of the dots. In these instances, the percentage difference may appear to be large, even though the absolute difference between the responses of the two models is effectively very small. This issue is relevant to the top portion of the plot for U_X and U_Z, as well as the entire plot for U_Y.

In summary, with the high-fidelity model as benchmark, the above results validate that the proposed surrogate analytical model (and implicitly the metamodel) has satisfactory accuracy in computing the EDPs (PMM) and displacement responses. Meanwhile, the surrogate model also offers significant simplicity and efficiency in FE model creation and

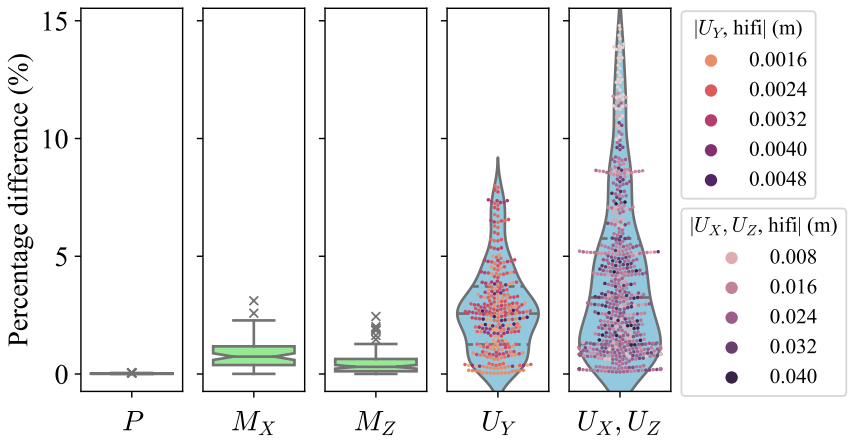

Figure 2.20: Percentage difference of structural responses regarding the middle panels.

computation.

2.5.2 Application in a full tower model

Given that nonlinear effects tend to amplify with increasing panel count, the performance of the proposed surrogate model within the context of a full-height tower was investigated. The assessment was twofold: first, pushover analyses were performed under transverse and longitudinal load cases, and the resulting load-displacement curves were compared; second, fragility curves under stochastic hurricane wind loads derived by the high-fidelity model and the surrogate model were compared.

The tangent suspension tower used for validation is of height 15.22 m, and the angle sections of the various members are given in Figure 2.21a. For the purpose of comparing the high-fidelity and surrogate models, the angle sections were assigned without following a formal tower design process. Additionally, the top straight panel was assumed to serve as the peak of the tower and support the ground wire. Figure 2.21a shows the high-fidelity model of the tower, where the slippage parameters and yield stress were set to their mean values listed in Table 2.1. The capacities of the angle members were calculated by Equation (2.3). Figure 2.21b shows the surrogate model of the tower. The metamodel input

data for all eight panels within the tower—and in turn the FE model and the panel capacities—were treated as known and deterministic. In addition to the basic body composed of the straight and inclined panels, the crossarms and peak need to be modeled in order for the loads at the attachment points to be transmitted to the tower body. Assuming that the peak and crossarms do not fail, this study models them with the elastic Bernoulli beam-column element available in OpenSees (McKenna et al., 2010). As illustrated in Figure 2.21b, each crossarm is modeled with two elements using the same stiffnesses (K_{sa}, K_{sb}, K_{st}) as the panel that it is attached to. The peak (i.e., the top panel) is modeled with one element that share the same stiffnesses (K_{sa}, K_{sb}, K_{st}) as panel 8. As a result, the tower is effectively modeled by a series of beam-column elements, with each panel surrogate paired with the consistent PMM capacity.

For the purpose of load calculations, the tower was assumed to support six phase conductors (Bluebird: unit weight = 2.511 lb/ft or 36.62 N/m, diameter = 1.762 inch or 4.48 cm) and one overhead ground wire (3/8 HS: unit weight = 0.273 lb/ft or 3.984 N/m, diameter = 0.36 inch or 0.914 cm). The spans ahead of and behind the tower were assumed to be equal (span length = 600 ft or 182.9 m) and level. The wind loads were calculated using the static equivalent gust wind loads model which can provide a reasonable hurricane wind load pattern (ASCE, 2016; Mohammadi Darestani et al., 2020). The expression for the wind force (F) is the following:

$$F = (0.613 \cdot K_z \cdot K_d \cdot K_{zt} \cdot K_e \cdot V^2) \cdot G \cdot C_f \cdot A_p \tag{2.25}$$

where K_z is the velocity pressure exposure coefficient; K_d, K_{zt} and K_e are respectively the directionality factor, the topographic factor and the elevation factor, and they are taken as 1 (Mohammadi Darestani et al., 2020); V is the 3-second gust wind speed at 10 m above ground; G is the gust effect factor; C_f is the force coefficient; and A_p is the area projected on the plane perpendicular to the wind direction. K_z reflects the effect of height (z) and

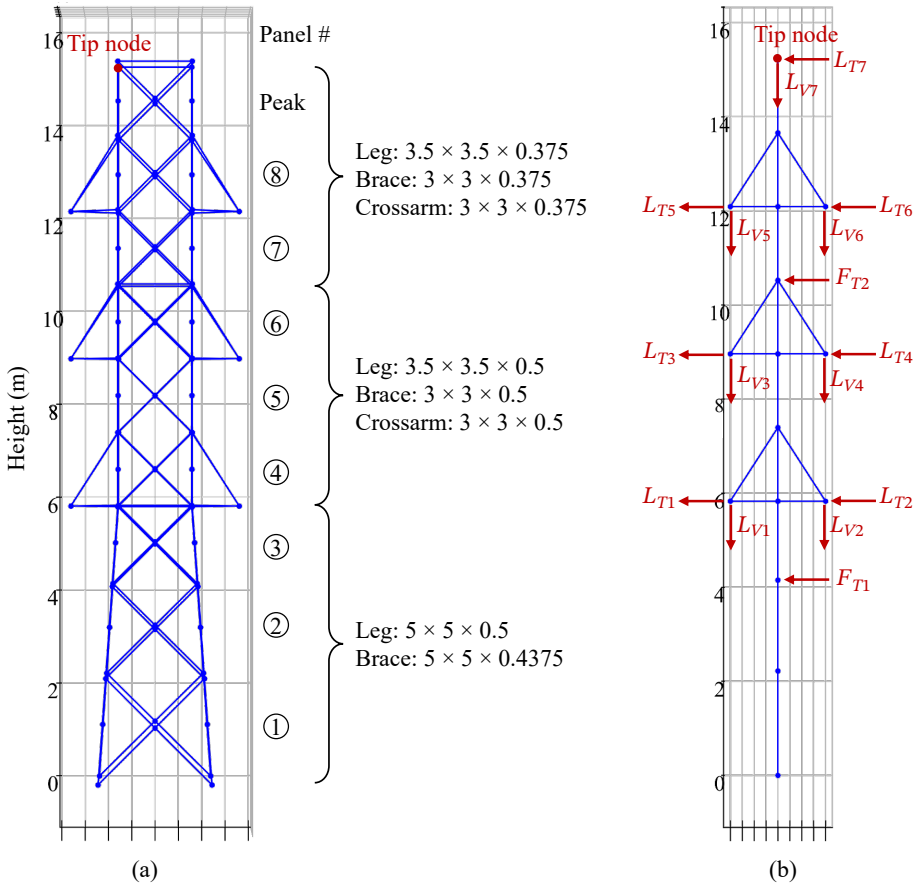

Figure 2.21: (a) High-fidelity tower model; (b) Surrogate tower model, and an illustration of the transverse wind load case (the loads are not drawn to scale). Note that the dimensions of the angle profiles are in inches, and further information on these profiles can be found in Table A.1

terrain and can be calculated as:

$$K_z = 2.01 \left(\frac{\max(4.75, z)}{z_g} \right)^{\frac{2}{\alpha}} \tag{2.26}$$

where $\alpha = 9.5$ and $z_g = 274.32$ m, assuming exposure category C.

Three uncertain variables (K_z, G, and C_f) were considered, for which probabilistic models from the literature were adopted (Ellingwood and Tekie, 1999). Specifically, K_z follows a Normal distribution with mean calculated by Equation (2.26) and coefficient of variation (c.o.v.) equal to 0.16; G also follows a Normal distribution with mean equal to 0.85 and c.o.v. equal to 0.11; and C_f follows a Normal distribution with mean set to 1 for wires or calculated by $4\Phi^2 - 5.9\Phi + 4$ for tower body (where Φ is the solidity ratio) and the c.o.v. equal to 0.12. Figure 2.21b illustrates the load application for the case of transverse wind. As mentioned earlier, the longitudinal loads (L_L) at the attachment points are negligible and thus taken as zero. The wind-induced transverse loads (L_T) are determined using Equation (2.25). The vertical loads (L_V) are calculated as the weight of the wire supported plus the weight of the associated hardware assembly. Moreover, the direct wind loads on the tower (F_T) are calculated segment-wise by Equation (2.25) and are applied at the nodes closest to the points where the loads are calculated. I.e., in the high-fidelity model, each F_T load is evenly distributed among the associated four nodes.

Pushover analyses were performed for two load cases: transverse and longitudinal. The wind load profiles were determined assuming a wind speed of $V = 60\,\mathrm{m/s}$, with the three uncertain variables set to their mean values. The pushover analyses for both the high-fidelity and surrogate models were carried out using displacement control. At each analysis step, failure checks were executed: the high-fidelity model assessed leg member failure based on individual capacities, while the surrogate model evaluated panel failure according to Equation (2.23). The analyses were terminated upon the occurrence of any leg failure in

the high-fidelity model or any panel failure in the surrogate model.

Figure 2.22 presents the load-displacement relationships for the two load cases, where the displacement corresponds to the transverse or longitudinal displacement recorded at the tip node. As expected, the surrogate model produces linear load-displacement curves, while the high-fidelity model exhibits nonlinear behavior due to slippage and other nonlinear effects. Nonetheless, the relationships given by the surrogate model remain in good agreement with those of the high-fidelity model across both load cases. For the transverse load case, the high-fidelity tower failed at a load factor of 2.9, with a corresponding tip displacement of 119 mm. The failure occurred in one of the compressive legs in the bottom panel. Although the other compressive leg on the same side did not fail simultaneously, it was very close to failure. In comparison, the surrogate tower failed at a load factor of 3.1, with a tip displacement of 129 mm. The failure occurred in the bottom panel, which aligns with the failure location observed in the high-fidelity model. For the longitudinal load case, where wind only induces loads on tower body, higher load factors were required to cause failure. The high-fidelity tower failed at a load factor of 12.1 with a tip displacement of 107 mm. Similar to the transverse case, one compressive leg in the bottom panel failed, while the other compressive leg was near failure. The surrogate tower reached failure at a load factor of 13.3 with a tip displacement of 128 mm. The failure occurred in the bottom panel, consistent with the failure location in the high-fidelity model. In both load cases, the results from the surrogate model were close to those of the high-fidelity model. The discrepancy in the load factor at failure is 7% for the transverse case and 10% for the longitudinal case. While such difference would be unacceptable for the study of an individual tower, it is well within the range of approximations done for portfolio fragility model development. It is worth highlighting that the pushover analysis for each loading condition took over 30 minutes on an Apple M3 processor, whereas the surrogate model completed the same analysis in just a few seconds on the same hardware.

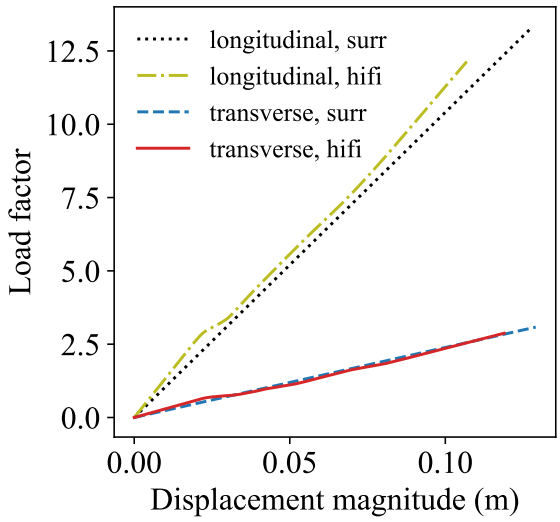

Figure 2.22: Comparison of load-displacement relationships.

For the purpose of fragility curve derivation, the 3-second gust wind speed was selected as the intensity measure (IM), and the fragility curves were derived for the transverse wind direction. Following an approach similar to that presented by Shinozuka et al. (2000), 500 IM levels were randomly sampled within the range of [80, 130] m/s using LHS. At each IM level, three wind load samples were generated based on the aforementioned distributions, and corresponding static equivalent wind analyses were performed. For each analysis, the tower response was recorded as either failure or survival, thus providing a set of fragility observations. In total, 1500 FE analyses were conducted for both the high-fidelity model and the surrogate model. The fragility curves were fitted assuming a LN distribution, with the median (θ_c) and standard deviation (β_c) estimated by the maximum likelihood method.

The fragility curve derived from the high-fidelity model had parameters ($\theta_c = 94.7$, $\beta_c = 0.00354$), while that from the surrogate model had ($\theta_c = 97.9$, $\beta_c = 0.00246$). The median values—the IM level with 50% probability of failure (P_f)—indicate a 3.2 m/s shift, or a 3.4% discrepancy; the standard deviations show a 30.5% discrepancy. It should be noted that the variation in θ_c generally has the first-order effect on fragility values, whereas that in β_c has the second-order effect (Shinozuka et al., 2000; American Nuclear Society,

1982). For instance, Baker (2015) indicated that a c.o.v. between 0.06 and 0.08 for θ_c, and between 0.20 and 0.40 for β_c, may be acceptable for seismic fragility estimates of buildings. Similarly, previous work suggested that a 5% difference in the median and dispersion would be adequate for seismic fragility estimates of bridges (Padgett and DesRoches, 2007). Therefore, the discrepancy between the fragility curves derived by the surrogate model and the high-fidelity model is in line with the level of accuracy generally expected in these applications, and is deemed acceptable, especially given the intended use of the surrogate model for portfolio-scale analysis.

2.5.3 Limitations and future studies

It should be noted that the proposed surrogate panel model employs a linear element formulation and yet accounts for nonlinear effects. For example, the calibration of the shear stiffness reflects the connection behavior, with consideration of potential slippage. This type of approximation works very well for panels exhibiting modest nonlinear behavior, but it may become inaccurate in cases of strongly nonlinear response. Moreover, the defined failure LS and EDPs are focused specifically on capturing leg buckling, which can trigger global instability and ultimately tower collapse. While this is the most common failure mode, it must be acknowledged that other members can fail, and intermediate failure modes (e.g., partial collapse) may occur, which would not be captured well by the proposed surrogate. This limitation is particularly relevant for other classes of towers (e.g., tension towers), which are designed to resist longitudinal loads and may experience failure primarily in bracing members rather than legs. Finally, the metamodel is trained based on the configurations provided in Table 2.1, and caution should be exercised when applying it to extrapolated scenarios beyond this training set.

When developing a computational model for probabilistic simulation, three key objectives are typically sought: (1) mechanical accuracy; (2) a small number of modeling pa-

rameters, which facilitates the probabilistic calibration of the input; and (3) computational efficiency, which enables analysts to run extensive cases and investigate effectively the probabilistic space. Traditional models of transmission towers (called 'high-fidelity models' herein) offer a trade-off among these goals that largely favors mechanical accuracy, at the expense of the other two goals. This trade-off is ideal when studying a single tower, and such models are indeed commonly used in that context. This study introduces a new computational model (called 'surrogate') that strikes a different balance: it achieves extremely low computational cost and a small number of modeling parameters, at the expense of some potential loss of accuracy. This different balance is particularly appealing when studying portfolios of towers, such as all transmission towers in the Florida power system. In such cases, computational speed is essential, and the ability to calibrate just a small set of probabilistic model parameters to capture structural variability across the portfolio makes the effort practical.

Moreover, in the context of portfolio analysis, a small loss of accuracy at the individual structure level becomes tolerable, because aggregate results are less sensitive to the response of individual structures (Rincon and Padgett, 2024). Indeed, the results show that the model's ability to capture structural stiffness and capacity is not affected by bias (see Figure 2.16). Therefore, individual under- and over-estimations may offset each other across the portfolio. For a global assessment of the expected monetary loss in transmission lines due to a hurricane, this level of accuracy is entirely appropriate, and the simplicity of the model makes large-scale analyses feasible. Different types of decisions call for different modeling strategies; this study introduces a new class of models for towers, specifically tailored to support portfolio-level decision-making.

In this sense, one major contribution of this work—beyond the specific surrogate model presented—is a rational procedure for developing and evaluating mechanical models that are particularly suitable for large-scale probabilistic analysis. This procedure can be ex-

tended to develop alternative models that offer different trade-offs or target other structural systems. For example, future studies could explore the use of nonlinear beam elements as panel surrogates. While such models would entail a modest increase in computational cost and roughly twice the number of modeling parameters, they may yield higher accuracy. Similarly, the procedure could be adapted to develop panel-based surrogate models for telecommunication towers, following the same calibration strategy and performance assessment steps presented in this study.

2.6 Concluding remarks

This study abstracts panels as the basic components of transmission towers and proposes physics-based surrogate models of panels, which enables efficient panel-level finite element modeling of towers and panel-based tower failure analysis under hurricane winds. In contrast to existing studies that conventionally used the high-fidelity, member-level modeling approach for deriving archetype tower fragilities, the proposed approach targets the need of modeling and analyzing heterogeneous portfolios of towers in the context of regional-scale analysis. The methodology described can be applied to all types of lattice steel towers. With a focus on the panels in double-circuit transmission towers, the failure limit state (LS), engineering demand parameters (EDPs), and the surrogate analytical model (via the beam-column element formulation) are coherently established. Further, a polynomial response surface metamodel is introduced for consistent simulation of panel capacity and demand. The accuracy and efficiency of the proposed surrogate analytical model are examined for the cases of 3-panel structures and a full-tower example.

Specifically, two types of panels (i.e., straight and inclined) were abstracted as the basic components from the construction and mechanical perspectives. The broad variations of panels in the scope of portfolios of towers were characterized from the aspects of topology,

geometry, size, connection, etc. Throughout the study, the high-fidelity, 3-panel structure models with connection details were utilized as the reference or benchmark. This study defined the panel failure LS as corresponding to the leg buckling and proposed using the axial load and two bending moments (PMM) as the EDPs. A batch of numerical experiments revealed that the PMM limit capacity surfaces for both types of panels are planes in the 3D space. Moreover, retaining all nonlinearities associated with the high-fidelity model offers little advantage in computing the desired EDPs. Thus, this study proposed using one 3D elastic beam-column element for surrogate modeling of one panel, where the axial, shear, bending and torsional modes are condensed into four corresponding stiffness parameters. Furthermore, a response surface metamodel was developed to translate the usual and known structural properties of panels into the surrogate modeling parameters and PMM capacity planes, while overcoming the potential issue of unrealistic demand-capacity pairs inherent to the direct sampling approach.

The proposed surrogate analytical model showed good accuracy with negligibly small percentage difference in the computed EDPs compared to the high-fidelity model. In the full-tower fragility curve estimation, the use of the surrogate tower facilitated the probabilistic simulation by using a small set of parameters, and the computational cost was minuscule (e.g., a finite element analysis required only several seconds). In the considered example, the surrogate model introduced a 3.4% discrepancy in the median parameter of the estimated fragility curve. This level of error renders the model inappropriate for the study of individual structures and their reliability. However, the complexity of portfolio-scale analyses and the need to limit the computational cost of each finite element evaluation make some level of compromise in accuracy common in practice.

As a persistent challenge faced by the research community in regional risk assessment, the availability and fidelity of data (or information) often poses huge constraints even if low-fidelity structural models are used. The aforementioned features offered by the pro-

posed surrogate model, as well as the consistent simulation of panel capacity and demand, require the metamodel input data for all panels of each sample tower, which is not trivial. Tower inventory data can ideally be obtained from utility companies or reconstructed using a tower design module. Alternatively, such lack of data essentially presents a source of epistemic uncertainty, whose effect can be accounted for via rigorous uncertainty characterization and propagation. Sensitivity studies can help explore the role of information fidelity and the relative importance of associated uncertainties, thereby guiding efforts in data collection and uncertainty treatment (Nielson and DesRoches, 2006; Padgett and DesRoches, 2007).

Chapter 3

Parameterized class fragility model for transmission towers under hurricane wind

3.1 Introduction

Risk and resilience assessment has increasingly shifted from the scale of individual structures to regional or network scales, which involve heterogeneous portfolios containing hundreds or even thousands of assets (structures) (Silva et al., 2019). Such portfolios inherently exhibit inter-structure variability (also known as structure-to-structure variability). Fragility analysis is a key component of risk and resilience modeling frameworks. In practice, fragility models—also termed fragility functions or fragility curves—are widely used to predict the damage levels of physical assets (Melchers and Beck, 2018). At the regional scale, however, fragility modeling must account not only for the load uncertainty and intra-structure uncertainty (also known as within-structure uncertainty), but also for the additional complexity of inter-structure uncertainty.

Two mainstream families of approaches exist for fragility modeling: archetype fragilities and parameterized (class) fragilities, distinguished primarily by how they address inter-structure uncertainty. The archetype approach is more common, largely due to its similarity to single-structure fragility development and historical precedent, while parameterized fragilities remain less studied. Archetype fragilities are developed by selecting a few representative (or index) structures from the portfolio or class, then deriving a fragility model for each. This procedure follows the conventional single-structure framework, accounting only

for intra-structure and load uncertainty. In application, each archetype fragility is assigned to the subset of the portfolio it best represents. However, this approach has notable drawbacks. First, it provides only a coarse representation of portfolio fragility, capturing heterogeneity at low resolution, which can mislead downstream risk and recovery assessments (Rincon and Padgett, 2024). Second, the selection of representative archetypes is typically based on basic structural characteristics (e.g., via clustering or classification) rather than directly on damage/fragility outcomes (Porter and Cho, 2013; Silva et al., 2019). As a result, it is difficult to ensure that the chosen archetypes truly represent the 'mean' fragility of their subsets, leaving potential bias in the results. In contrast, parameterized fragility models explicitly characterize and propagate inter-structure uncertainty. Rather than relying on a few representative structures, this approach involves probabilistic simulation of hundreds or thousands of structures, depending on portfolio heterogeneity. These fragilities are expressed as functions of a vector of parameters, such as structural features, site conditions, system configurations, and material properties. This parameterization enables flexible fragility models that capture heterogeneity more rigorously and provide finer-grained and more reliable regional damage assessments. Parameterized fragility models have been developed for classes of bridges (Ghosh et al., 2013; Misra and Padgett, 2019), wood distribution poles (Mohammadi Darestani and Shafieezadeh, 2019), and buildings (Seo et al., 2012; FEMA, 2020).

Despite progress in some asset classes, parameterized fragility models remain scarce—and in many cases absent—for critical infrastructure such as lattice transmission towers used in electric power networks. Historical hurricanes have repeatedly shown the vulnerability of these towers (NERC, 2018; U.S. Department of Energy, 2013; Schweikert et al., 2019). While many studies have developed single-structure or archetype-based fragilities for transmission towers (Cai et al., 2019; Dikshit and Alipour, 2023; Fu et al., 2019; Ma et al., 2021a; Macedo et al., 2024; Tian et al., 2020), to the best of our knowledge, no param-

eterized fragility models exist for transmission towers. This gap limits the quality of risk and resilience assessments for power transmission networks and, by extension, other interdependent infrastructure systems. A major challenge in developing class fragility models for transmission towers is the lack of suitable surrogate models. Traditionally, towers have been analyzed using high-fidelity finite element (FE) models of varying complexity, where hundreds of members were explicitly modeled to capture member-level buckling failures (Mohammadi Darestani et al., 2020; Ma et al., 2021a) While appropriate for single-tower analysis, these models are impractical for class fragility development. High-fidelity models are computationally expensive, demand detailed input data that are infeasible to collect at the portfolio scale, and are not well suited for efficient probabilistic simulation. Chapter 2 introduced physics-based surrogate models of lattice panels, enabling efficient panel-level FE modeling of towers and panel-based failure analysis under hurricanes. This approach provides a pathway toward portfolio-oriented, parameterized fragility models for transmission towers (Wang and Bocchini, 2025b).

Building on the aforementioned surrogate models, this chapter presents the derivation of parameterized fragility models for a general class of transmission towers under hurricane winds, using dynamic analysis. Section 3.2 outlines an eight-step framework for developing parameterized class fragility models, following a well-established approach, but also introducing several original details and recommendations for best practice. In Section 3.3, we demonstrate the framework through an application to the Florida transmission line portfolio, a region highly prone to hurricanes. We propose an efficient method for modeling tower–line systems. For uncertainty modeling of the tower class, we introduce a novel approach that transforms the uncertainty in transmission line design variables into uncertainty in surrogate-compatible modeling parameters via a design module and conversion step. Furthermore, we present a strategy for efficient and sufficient uncertainty propagation, based on hierarchy of the uncertainties. The results of the parameterized fragility

models are then presented, along with sensitivity analysis and discussion. Section 3.4 concludes with a summary of the main contributions and findings.

3.2 Development of parameterized class fragility models

This section revisits the framework for developing parameterized class fragility models, with a focus on analytical fragilities derived by structural analysis. The framework consists of eight common steps, as shown in Fig. 3.1. For clarity, each step is presented in a dedicated subsection, with the corresponding application demonstrated in Section 3.3. Fragility curve development is a broad topic, and modeling choices at each step can be highly asset- and hazard-dependent. Our goals are: (1) to present the framework at a high level, independent of specific hazards or assets, by clearly identifying the general task of each step and introducing formal mathematical notations where appropriate; and (2) to highlight typical modeling choices and practices, supported by illustrative examples, while pointing out associated challenges and potential pitfalls.

When modeling a portfolio of assets, a large number of input parameters (or variables) are typically involved. In the context of fragility development, these parameters can be broadly divided into four types, which will be used throughout this chapter. For clarity, the definition and notation of each type are briefly summarized below, while more detailed explanations are provided in the following subsections.

- Type I: Parameters used for asset classification, denoted as vector $\boldsymbol{X}^{\mathrm{I}} = [X_1^{\mathrm{I}}, X_2^{\mathrm{I}}, \ldots, X_{n_1}^{\mathrm{I}}]$. These may be quantitative (e.g., number of stories) or qualitative (e.g., construction material) structural characteristics and must be available to the analyst, as they are required to apply the developed fragility model. A specific set of Type I parameters defines a class of assets with shared characteristics but still some inter-structure variability. For instance, in seismic damage assessment, highway bridges are classified

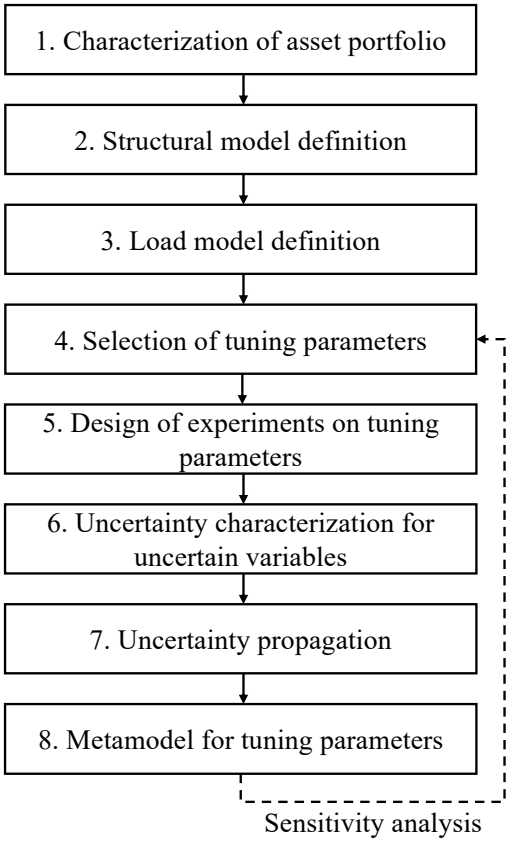

Figure 3.1: Common steps for developing portfolio-oriented, parameterized fragility models. The dashed line indicates the optional revision/iteration process informed by sensitivity analysis.

by characteristics such as girder material (FEMA, 2020).

- Type II: Parameters used to tune the (class) fragility model, often referred to as *tuning parameters*, denoted as vector $\boldsymbol{X}^{\mathrm{II}} = [X_1^{\mathrm{II}}, X_2^{\mathrm{II}}, \ldots, X_{n_2}^{\mathrm{II}}]$. Also these must be known by the analyst, who has to specify their values to adjust the fragility model. Type II parameters can be seen as a way to define more granular subclasses within a Type I class, offering flexible (and potentially infinite) combinations rather than a few fixed categories. For instance, seismic fragility models of highway bridge classes are parameterized by span length and skew angle, among others (FEMA, 2020).

- Type III: Parameters are assumed to be unknown by the analyst and treated as random variables, denoted as vector $\boldsymbol{X}^{\mathrm{III}} = [X_1^{\mathrm{III}}, X_2^{\mathrm{III}}, \ldots, X_{n_3}^{\mathrm{III}}]$. Their uncertainties are propagated and embedded in the fragility model. Examples include material strengths and damping ratio.

- Type IV: Parameters that are fixed at deterministic nominal or conventional values, denoted as vector $\boldsymbol{X}^{\mathrm{IV}} = [X_1^{\mathrm{IV}}, X_2^{\mathrm{IV}}, \ldots, X_{n_4}^{\mathrm{IV}}]$. These either exhibit negligible variability or have minimal impact on the outcome. For example, a strain-hardening ratio of 0.01 is a widely accepted default for modeling bilinear steel material.

Lastly, there is the intensity measures IM, capturing the intensity of the hazard event at the site of the asset. Sometimes multiple intensity measures are used for the same fragility model (e.g., gust wind speed and direction). Some modelers consider the intensity measure(s) part of the Type II variables, but given its special role, in this study we prefer to treat IM as a separate class of variables. For a given asset class, the parameterized fragility for a certain limit state is expressed as the conditional probability $P_{f|\boldsymbol{X}^{\mathrm{II}};IM}$. This formulation is distinct from traditional fragility models, $P_{f|IM}$, which are conditional only on IM. Sometimes, parameterized fragility models are also referred to as 'multi-dimensional' or 'multivariate'. Once the tuning parameters are specified ($\boldsymbol{X}^{\mathrm{II}} = \boldsymbol{x}^{\mathrm{II}}$), the tailored fragility

$P_{f|\boldsymbol{X}^{\mathrm{II}}=\boldsymbol{x}^{\mathrm{II}};IM}$ reduces to the familiar two-dimensional fragility curve, with intensity measure on the horizontal axis and probability of reaching or exceeding a given limit state on the vertical axis. It is often desirable to represent fragility models with an analytical model, such as the lognormal (Mohammadi Darestani and Shafieezadeh, 2019; FEMA, 2020) or logistic (Misra and Padgett, 2019; Rincon and Padgett, 2024) cumulative distribution functions (CDF). In such cases, the parameters of the analytical curve are expressed as functions of the tuning parameters (i.e., Type II variables). For example, if the lognormal CDF is chosen as analytical representation of the fragility curve, the probability of reaching or exceeding a certain limit state at $IM = im$ and with tuning parameters $\boldsymbol{X}^{\mathrm{II}} = \boldsymbol{x}^{\mathrm{II}}$ is given by:

$$P_{f|\boldsymbol{X}^{\mathrm{II}}=\boldsymbol{x}^{\mathrm{II}};IM=im} = \Phi\left(\frac{\ln\left(im/\theta(\boldsymbol{x}^{\mathrm{II}})\right)}{\beta(\boldsymbol{x}^{\mathrm{II}})}\right) \tag{3.1}$$

where $\Phi(\cdot)$ is the standard normal CDF; $\theta(\boldsymbol{x}^{\mathrm{II}})$ and $\beta(\boldsymbol{x}^{\mathrm{II}})$ denote the median of the lognormal distribution and the standard deviation of the associated normal distribution, respectively. Both θ and β are expressed as functions of the tuning parameters; thus, parameterizing a class fragility requires identifying the functional relationships between the Type II variables and the fragility curve parameters. In most cases, these relationships are obtained by calibrating separate models ('metamodels'), such as polynomial response surfaces. The estimates of the fragility curve parameters obtained by these models are denoted as $\hat{\theta}(\boldsymbol{x}^{\mathrm{II}})$ and $\hat{\beta}(\boldsymbol{x}^{\mathrm{II}})$.

3.2.1 Step 1: Characterization of asset portfolio

For developing portfolio-oriented fragility models, characterizing the portfolio of assets is essential. However, data on entire portfolios are often difficult to obtain and may even be inaccessible for security reasons in the case of critical infrastructure. Common sources of portfolio data include: (1) public inventory data, such as the National Structure Inven-

tory (U.S. Army Corps of Engineers, Hydrologic Engineering Center, 2025) and National Bridge Inventory (FHWA, nd); (2) targeted data collection using field surveys (Porter and Cho, 2013); (3) proprietary data purchased from vendors; (4) synthetic inventory data generated using statistical or simulation-based methods (Deierlein et al., 2020). In practice, portfolio data are often incomplete or imperfect, necessitating imputation. The availability and fidelity of data directly influence (key) modeling choices, such as the selection of tuning parameters and portfolio modeling, as will be discussed later.

Once portfolio data are available, understanding and characterizing the heterogeneity of assets within the portfolio is a critical step. This typically involves classifying or clustering assets based on salient structural characteristics—Type I parameters ($\boldsymbol{X}^{\mathrm{I}}$). A given portfolio may consist of a single class or, more commonly, multiple classes.

3.2.2 Step 2: Structural model definition

This work focuses on analytical fragility models, which entail physics-based, mechanical representations of structural response, in contrast to non-analytical fragility models derived from expert judgment or post-event damage observations. The appropriate analytical approach depends on the asset and hazard type, and the modeler must decide among options such as dynamic versus static analysis, linear versus nonlinear, or closed-form versus FE models (Silva et al., 2019). Because closed-form solutions are rarely available and typically rely on restrictive assumptions, FE models are most often required. Accordingly, the following discussion of structural and load model definitions focuses on FEM-based analysis.

For portfolio- or regional-scale analysis, models of varying complexity can be used, ranging from high-fidelity models to simplified or surrogate models. Choosing the appropriate model is both important and nontrivial. The choice should be guided by three main

factors. First, the model must compute the relevant engineering demand parameters (EDPs) and capture the governing failure modes and limit states (LSs). High-fidelity models generally provide more detailed and accurate response quantities, but simplified models can also capture key behaviors and deliver comparable accuracy when carefully calibrated (Patsialis and Taflanidis, 2020; d'Aragona et al., 2020; Wang and Bocchini, 2025b). Second, the number of models required to represent portfolio heterogeneity must be balanced against computational cost. High-fidelity models are time consuming to build and analyze, and this makes them particularly suitable for archetype-based fragility studies, which rely on only a few representative structures. In contrast, parameterized fragility modeling, as pursued here, often involves hundreds or thousands of structural realizations, where simplified or surrogate models become essential to enable large-scale simulations while still capturing portfolio heterogeneity. Third, and sometimes overlooked, is the information (data) required to construct the simulation model. A higher-complexity model offers little benefit if it requires input data that are not available with sufficient confidence for the application at hand. Any potential gains in simulation accuracy are often offset by the large uncertainties introduced when assigning poorly known parameter values for the entire portfolio. Thus, the complexity of the model should be commensurate with the type and quality of data available (Lu et al., 2020; Yi et al., 2025).

In general, high-fidelity nonlinear models excel in mechanical adequacy but face limitations in computational tractability and data demands. Simplified models, while less detailed, can provide practically useful results and perform well in these latter aspects, making them favorable for portfolio-scale applications. For example, the number of parameters needed to meaningfully represent different asset classes is typically moderate, ranging from a few units to a few dozen (Nielson, 2005; Patsialis and Taflanidis, 2020), whereas the number of modeling parameters in high-fidelity models can easily be in the hundreds.

In the field of class fragility curve development, models with a relatively high level

of simplification and surrogation have been preferred. For example, for bridge fragility development, it is customary to use finite element models that capture the behavior of complex structural components with zero-length finite elements. For instance, the complex geometry and mechanics of a bridge abutment dissolves into only a couple of parameters controlling its active and passive stiffness. This simplifies the generation of random bridge samples while preserving the ability to correctly capture the structural response (Nielson, 2005).

3.2.3 Step 3: Load model definition

Loads can be static or dynamic, with corresponding analyses carried out using static procedures or dynamic time history analysis (DTHA). Despite its higher computational cost, dynamic analysis is preferred because it explicitly captures load duration, transient effects, and event-to-event variability, whereas static analysis largely misses these aspects and can yield biased results. For dynamic loads, either recorded or synthetic time histories may be employed, such as ground motions (Wen and Wu, 2001; Ancheta et al., 2014) or wind velocity histories (Khazaali et al., 2022).

Fragility development requires analyses over a range of hazard intensities to bring the structure to relevant damage or failure states. A key question in this step is which intensity measure to use.While the literature on earthquakes provides extensive discussion and criteria for intensity measure selection (Padgett et al., 2008; Giovenale et al., 2004)—such as efficiency, practicality, and hazard computability—studies for other hazards (e.g., hurricanes, hail, floods, wildfires) remain comparatively limited. Nevertheless, many of these criteria are transferable across hazards. In the context of regional analysis, the criterion of hazard computability is particularly important; it refers to the level of effort required to obtain the probabilistic hazard or hazard curve. If a fragility model depends on an unavailable intensity measure, its use becomes infeasible or requires conversions that may introduce

error and bias. For example, hurricane wind intensity maps are typically expressed in 1-min maximum sustained wind speed (MSWS), consistent with the Saffir–Simpson scale (Wikipedia contributors, 2025c). Using alternative intensity measures such as the 3-sec gust or hourly mean wind speed requires conversion factors (SEA et al., 2010), which are often unreliable and can produce large errors (Khazaali et al., 2022). Thus, 1-min MSWS is the preferred intensity measure for hurricane wind fragility development on the basis of hazard computability.

3.2.4 Step 4: Selection of tuning parameters

For a given asset class defined by Type I variables, once the structural and load models have been selected, all model parameters are identified. These parameters can then be categorized into Types II, III, and IV based on the definition given earlier. Type IV parameters—fixed at nominal or conventional values—are usually straightforward to assign (e.g., gravitational acceleration, mesh size in FE models). In contrast, both Type II and Type III parameters exhibit variability that can have a meaningful influence on fragility outcomes. Therefore, their effects should be captured in the class fragility model, albeit in different ways.

The selection of Type II parameters (user-specified tuning parameters) should respect the principle that they are known by analyst using the fragility curves. These parameters are explicitly included in the class fragility expression ($P_{f|\boldsymbol{X}^{\mathrm{II}},IM}$) to tailor the model to subclass characteristics. In practice, the number of Type II parameters is typically limited to only a few. For example, five tuning parameters were used in wind fragility models for wood poles (Mohammadi Darestani and Shafieezadeh, 2019), and four tuning parameters were specified in the seismic fragility models for highway bridges (FEMA, 2020). Notably, while fragilities could in theory be parameterized with respect to Type III parameters, this approach undermines practical usability—similar to the hazard computability issue (Sec-

tion 3.2.3)—because users would need to estimate values for these unknown parameters. Instead, Type III parameters are transparent for the user of the fragility curves, even though their uncertainty is rigorously propagated and incorporated in the fragility model (see Section 3.2.6).

It should be noted that the influence of Type II and Type III parameters on fragility outcomes is often unclear beforehand, so their categorization and treatment partially rely on engineering judgment. A more rigorous approach is to use sensitivity analysis to systematically assess parameter influence and adjust their treatment accordingly (see Section 3.2.8).

3.2.5 Step 5: Design of experiments on tuning parameters

As noted earlier, parameterization of the class fragility model aims to establish functional relationships between the tuning parameters and the distribution parameters. These relationships are typically approximated using metamodeling methods, which require a set of input-output pairs. Exploring the entire input space $\boldsymbol{X}^{\mathrm{II}}$ is often infeasible or unnecessary. Therefore, design of experiments (DoE) is commonly used to strategically cover the input space and generate the required input–output pairs. Specifically, a set of n_s samples $\mathscr{X} = \{\boldsymbol{x}_1^{\mathrm{II}}, \ldots, \boldsymbol{x}_{n_s}^{\mathrm{II}}\}$, with $\boldsymbol{x}_i^{\mathrm{II}} \in \mathbb{R}^{n_2}$, is obtained from the DoE, and the corresponding outputs are evaluated for each design point. In our lognormal case, the outputs are $\boldsymbol{\vartheta} = [\theta_1, \ldots, \theta_{n_s}]$ and $\boldsymbol{\beta} = [\beta_1, \ldots, \beta_{n_s}]$, yielding input–output pairs $\{\mathscr{X}, \boldsymbol{\vartheta}\}$ for $\hat{\theta}(\boldsymbol{x}^{\mathrm{II}})$ and $\{\mathscr{X}, \boldsymbol{\beta}\}$ for $\hat{\beta}(\boldsymbol{x}^{\mathrm{II}})$.

A wide range of DoE techniques exists, from classical methods such as factorial and central composite designs to modern approaches like Monte Carlo sampling and Latin hypercube sampling (LHS). The choice of technique depends on factors including the number of inputs, the size of the design space, and the characteristics of the underlying functions (Viana et al., 2021). It is important to note that, unlike real-world experiments affected

by noise and inherent variability, computer simulations are deterministic: repeated runs with the same inputs produce identical outputs. Randomized DoE methods (e.g., LHS) can introduce variability in the design to mimic real-world effects. However, this should not be confused with the randomness used in uncertainty propagation, which serves to sample input distributions and propagate uncertainty through the model. Deterministic DoE (e.g., factorial designs) is equally valid and, in many cases, preferred due to its transparency and simplicity.

3.2.6 Step 6: Uncertainty characterization for uncertain variables

The uncertainty characterization step involves, for each i^{th} Type II DoE point $\boldsymbol{x}_i^{\text{II}}$, defining the joint distribution of the n_3 Type III parameters $\boldsymbol{X}^{\text{III}}$ (treated as uncertain variables). This distribution is denoted by $F^i_{\boldsymbol{X}^{\text{III}}}(\boldsymbol{x}^{\text{III}})$, $i = 1, 2, \ldots, n_s$. The joint distributions enable direct sampling for efficient probabilistic simulation to propagate uncertainty (see Section 3.2.7). Below we highlight three important aspects of uncertainty characterization in the portfolio context.

First, the joint distribution $F^i_{\boldsymbol{X}^{\text{III}}}(\boldsymbol{x}^{\text{III}})$ generally differs across DoE points, since each set of tuning parameters corresponds to a different ensemble of structures with potentially distinct inter-structure variability. Thus, the distribution should be characterized for each DoE point. It is generally advisable to keep the number of DoE points (n_s) and the dimension (n_3) at tractable levels. Second, uncertainty characterization at the portfolio scale requires careful consideration of information fidelity, as some 'translation' is often needed to move from available data to the mechanical parameters required by the simulation models. For instance, while available building data may include the number of stories, construction material, or design code specification, the mechanical model requires parameters such as stiffnesses and masses. This translation inevitably introduces uncertainty—interpreted as information fidelity—arising from incomplete data and/or the choice of translation method

(Yi et al., 2025). Different strategies exist for this process. Heuristic or data-driven rule-sets are often used to map common descriptions of buildings into mechanical parameters of reduced-order models (d'Aragona et al., 2020; Lu et al., 2020). Other studies have relied on experimental data, surveys, or simplifying assumptions to derive parameters for bridge classes (Nielson, 2005; Padgett, 2007). Wang and Bocchini (2025b) presented a regression-based approach that translates raw attributes of lattice structures (e.g., geometric dimensions, member areas) into surrogate-compatible modeling parameters (e.g., stiffnesses, capacities), informed by large-scale numerical simulations.

A third important, yet often overlooked, aspect of uncertainty characterization is the damage (or limit state) dependency among components of multi-component structural systems. Consider a system with $n_c > 1$ components, and let $\boldsymbol{\ell}$ denote the composite of component limit states within the system:

$$\boldsymbol{\ell} = \begin{bmatrix} \ell_1 \\ \ell_2 \\ \vdots \\ \ell_{n_c} \end{bmatrix} = \begin{bmatrix} C_1 - D_1 \\ C_2 - D_2 \\ \vdots \\ C_{n_c} - D_{n_c} \end{bmatrix} = \mathbf{C} - \mathbf{D} \tag{3.2}$$

where ℓ_j denotes the limit state of the j^{th} component, and $\ell_j \leq 0$ indicates that the component has reached the specified limit state; C_j denotes the capacity of the j^{th} component, collected in the capacity vector $\mathbf{C}$; D_j denotes the response (or demand) of the j^{th} component, collected in the demand vector $\mathbf{D}$. The system limit state is given by $\mathscr{L} = \phi(\boldsymbol{\ell})$, where ϕ is a function determined by the system configuration (e.g., series, parallel). Component damage dependency is generally considered from two perspectives: demand dependency (Gokkaya et al., 2017; Chen et al., 2022; Goda and Tesfamariam, 2015) and capacity dependency (Baker et al., 2024; Chen et al., 2024). Ultimately, these two aspects should be integrated to ensure realistic assessment of component and system damage; neglecting this

can lead to serious bias (Xie, 2025). In simple terms, capturing component damage dependency requires a dependence (or correlation) structure that accounts for both demands (**D**, or upstream mechanical modeling parameters) and capacities (**C**) across all components and damage states. A common approach for representing the dependency structure among variables is to use a copula (Chen et al., 2022; Goda and Tesfamariam, 2015). The sought joint distribution $F^i_{\boldsymbol{X}^{\mathrm{III}}}(\boldsymbol{x}^{\mathrm{III}})$ can be expressed using a copula as:

$$F^i_{\boldsymbol{X}^{\mathrm{III}}}(\boldsymbol{x}^{\mathrm{III}}) = \mathbb{C}^i\left(F^i_{X_1^{\mathrm{III}}}(x_1^{\mathrm{III}}),\ F^i_{X_2^{\mathrm{III}}}(x_2^{\mathrm{III}}),\ \ldots,\ F^i_{X_{n_3}^{\mathrm{III}}}(x_{n_3}^{\mathrm{III}})\right) \tag{3.3}$$

where copula $\mathbb{C}^i$ is the function that links the marginals $F^i_{X_1^{\mathrm{III}}}(x_1^{\mathrm{III}}), \ldots, F^i_{X_{n_3}^{\mathrm{III}}}(x_{n_3}^{\mathrm{III}})$ of the random vector $\boldsymbol{X}^{\mathrm{III}}$ to its joint CDF $F^i_{\boldsymbol{X}^{\mathrm{III}}}$. Various types of copulas exist, among which the Gaussian copula is commonly used and requires a linear correlation matrix (Lataniotis et al., 2015). It should be noted that characterizing joint distributions often relies on simulation or even expert judgment, as direct empirical data remain elusive (especially for capacity-related parameters).

3.2.7 Step 7: Uncertainty propagation

The characterized uncertainties—both intra- and inter-structure—together with load uncertainty, need to be propagated and embedded in the fragility model. To this end, correlated samples can be generated directly based on the joint distribution $F^i_{\boldsymbol{X}^{\mathrm{III}}}(\boldsymbol{x}^{\mathrm{III}})$; let the sample size be denoted by n_v. Let n_l denote the number of loads (static or dynamic) paired with each structure. The total number of FE analyses required is then $n_v \cdot n_l$.

Procedures originally developed for single-structure fragility derivation, such as incremental dynamic analysis and multiple stripes analysis (Baker, 2015), can be generalized to class-level fragility derivation with appropriate accommodation of inter-structure uncertainty. A key modeling choice is how large n_v and n_l should be (the so-called structure-load

pairing problem) to ensure that uncertainty is sufficiently propagated—so that the resulting fragility model (or its parameters) stabilizes with minimal computational cost. Addressing this requires understanding the relative dominance among different sources of uncertainty. The guiding principle is straightforward: given a fixed computational budget, prioritizing the propagation of the dominant source of uncertainty is the most effective and efficient strategy. For most realistic asset classes, inter-structure uncertainty tends to dominate (Silva et al., 2019). This implies that, under resource constraints, allocating more samples to n_v (structures) rather than n_l (loads) is generally the more efficient choice. Section 3.3.7 demonstrates how to rigorously determine the uncertainty hierarchy and use it to strategically guide uncertainty propagation.

Finally, for the i^{th} Type II DoE point $\boldsymbol{x}_i^{\text{II}}$, once the structural analysis data are collected, we fit them to the selected lognormal distribution to obtain (θ_i, β_i). Depending on how the structural analysis data are obtained, different parameter estimation techniques may fit, such as the method of moments or maximum likelihood method (Baker, 2015; Shinozuka et al., 2000).

3.2.8 Step 8: Metamodel for tuning parameters

The last step is to construct the functional relationships $\hat{\theta}(\boldsymbol{x}^{\text{II}})$ and $\hat{\beta}(\boldsymbol{x}^{\text{II}})$ using the input–output pairs $\{\mathscr{X}, \boldsymbol{\vartheta}\}$ and $\{\mathscr{X}, \boldsymbol{\beta}\}$, respectively. For this purpose, various metamodeling techniques can be employed. The best metamodel is typically unknown in advance. Therefore, it is common practice to train and compare multiple metamodels before selecting the optimal one (Ghosh et al., 2013). This process has become relatively straightforward, facilitated by popular machine learning packages such as *scikit-learn* (Pedregosa et al., 2011). Commonly used metamodels include, but are not limited to, polynomial response surface (PRS), random forest (RF), Extreme Gradient Boosting (XGBoost), and support vector regression (SVR) (Murphy, 2012). PRS models are simple and interpretable

but may struggle with highly nonlinear relationships and have been regularly used in parameterized fragility studies (Mohammadi Darestani and Shafieezadeh, 2019; Misra and Padgett, 2019). Both RF and XGBoost are tree-based ensemble models capable of capturing nonlinearities and interaction effects. SVR is a kernel-based method that extends support vector machines to regression problems, with different kernel choices such as linear or radial basis functions (RBF). These four metamodels are also applied in the Application section.

To evaluate and compare the performance of different metamodels, appropriate goodness-of-fit measures should be selected, such as the coefficient of determination (R^2) and mean absolute percentage error (MAPE). The R^2 quantifies the proportion of variance in the dependent variable that is explained by the independent variables. The MAPE measures the relative discrepancies between predicted and observed values, offering a standardized metric for model performance. Metamodels with good predictive performance are characterized by high R^2 and low MAPE. Once the best metamodel is selected—i.e., the functional relationships of the tuning parameters are established—the parameterized fragility model is obtained.

A further, beneficial step is sensitivity analysis (SA), which provides insight into the relative influence of the Type II parameters (those exposed for tuning) and even Type III parameters (those embedded in the fragility model). The results can inform adjustments to parameter categorization or uncertainty treatment, facilitating model refinement. This represents an ideal iterative workflow for fragility development, as illustrated in Fig. 3.1. For instance, if certain Type III parameters are found to have minimal impact on the final fragility, they can be fixed at median or nominal values (i.e., Type IV), thereby simplifying uncertainty propagation (Padgett and DesRoches, 2007). Numerous approaches are available for performing sensitivity analysis. These can be classified into sample-based methods (e.g., input/output correlation), linearization methods (e.g., perturbation method), and

global methods (e.g., Sobol' sensitivity indices, Kucherenko sensitivity indices) (Marelli et al., 2019). In this study, three sensitivity metrics are considered (see Section 3.3.9.2) and are described below.

Let V denote a general output, which can be certain structural response or failure fraction. Let $\mathbf{U}$ represent the general input random vector, which may include Type II and Type III parameters. Two correlation-based sensitivity measures are commonly used due to their simplicity: the linear correlation coefficient and the Spearman's rank correlation coefficient. These measures remain applicable even when the input variables are dependent. The linear correlation coefficient ρ_i between the i^{th} input and the output is defined as:

$$\rho_i \overset{\text{def}}{=} \rho(U_i, V) = \frac{\mathbb{E}[(U_i - \mu_i)(V - \mu_V)]}{\sigma_i \sigma_V} \tag{3.4}$$

where $\mu_i \overset{\text{def}}{=} \mathbb{E}[U_i]$ and $\mu_V \overset{\text{def}}{=} \mathbb{E}[V]$; σ_i and σ_V are the corresponding standard deviations. However, linear correlation is known to be inaccurate in the presence of strong nonlinear dependence between variables. A more robust alternative is the Spearman's rank correlation coefficient (ρ_S), which relies on monotonicity. It is defined as the linear correlation between the ranks:

$$\rho_i^S \overset{\text{def}}{=} \rho_S(U_i, V) = \rho(R_i, R_Y) \tag{3.5}$$

While input/output correlation coefficients can provide insight into the influence of individual inputs on the output, they cannot capture interactive effects among inputs. Global sensitivity analysis is therefore preferred, as it considers the entire input domain. Sobol' sensitivity indices (Sobol, 2001) are perhaps the best-known global method, but they are only valid under the restrictive assumption of independent input variables. For dependent input variables, alternatives such as ANalysis of COVAriance (ANCOVA) sensitivity indices (Xu and Gertner, 2008) and Kucherenko sensitivity indices (Kucherenko et al., 2012) have been proposed. Both generalize Sobol' indices to the dependent case and are based

on variance decomposition. In this study, the Kucherenko indices are adopted. The two major variance-based sensitivity indices with respect to one input variable U_i are the first-order index, which represents the effect of U_i alone, and the total index, which includes the interaction effects between U_i and other inputs.

3.3 Application

This section applies the above framework to develop parameterized fragility models for a general class of lattice transmission towers, focusing on the electric transmission network in hurricane-prone Florida. The following Sections 3.3.1 – 3.3.8 are structured according to the eight steps of the framework, while the derived fragility models and sensitivity analysis results are presented in Section 3.3.9.

3.3.1 Florida transmission line portfolio and representative tower class

Fig. 3.2 shows the transmission lines in Florida, spanning five voltage levels from 69 kV to 500 kV (Homeland Infrastructure Foundation-Level Data (HIFLD), 2022). The total line lengths by voltage level are presented in Fig. 3.3, where it can be seen that 230 kV lines account for the largest share. A transmission line consists of two subsystems: the wire system (e.g., conductors, ground wires, insulators) and the structural support system (e.g., lattice towers, poles). This study focuses on the fragility of the structural support system, while fragilities of the wire system can be found in dedicated studies such as Ma et al. (2020). Transmission line supporting structures can be broadly grouped into four types: single poles, double poles (H-frames), self-supporting towers, and guyed towers. This classification is coarse, as further distinctions (e.g., angle versus tangent, suspension versus tension) are possible (Kalaga and Yenumula, 2017). Among these, single poles, double poles, and self-supporting towers are the most common (see Fig. 3.4), while guyed

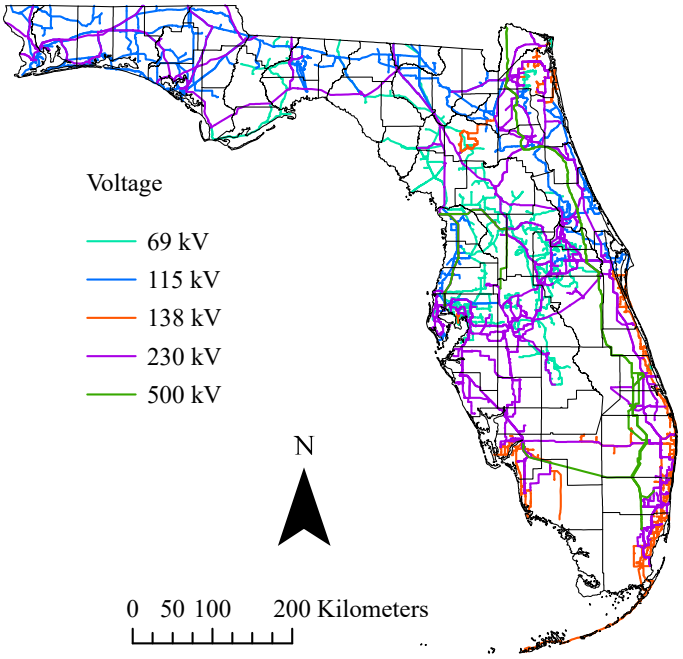

Figure 3.2: Geographic distribution of transmission lines in Florida by voltage level.

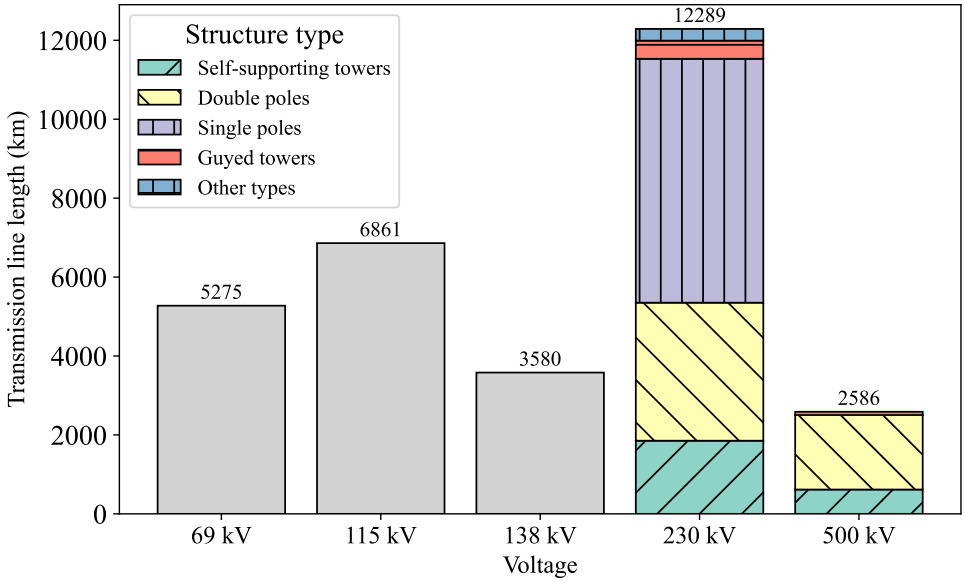

Figure 3.3: Transmission line lengths by voltage level. For 230 kV and 500 kV lines, the total lengths are further decomposed by structure type, as indicated in the legend.

Figure 3.4: Examples of transmission line supporting structures: a single pole, a self-supporting tower, and a double pole.

towers are less frequently used. Generally, poles dominate across transmission voltages due to their low cost and ease of construction, whereas lattice towers are more often used in higher-voltage lines that entail long spans and heavy loads.

While the dataset (Homeland Infrastructure Foundation-Level Data (HIFLD), 2022) provides basic information such as geographic location, voltage, and line length, it does not include details of the specific supporting structures. Because this study focuses on lattice towers, we collected additional structural data, restricting attention to higher-voltage transmission lines (230 kV and 500 kV) in Florida. The objectives were twofold: (1) to document structural characteristics and (2) to characterize portfolio heterogeneity. To this end, we performed GIS-based visual mapping using Google Earth Pro (Google LLC, nd) to document supporting structures along the transmission lines. For each line, we identified the support type, number of circuits, and cross-arm arrangements through visual inspection, and we measured span lengths between adjacent towers using built-in measurement tools.

The structural composition for the 230 kV and 500 kV lines is summarized in Fig. 3.3. For 230 kV lines, single poles, double poles, and self-supporting towers are most prevalent, whereas for 500 kV lines, double poles and self-supporting towers dominate.

In this application, we focus on a representative class of self-supporting towers: suspension and tangent towers with double circuits and a vertical crossarm configuration (SST2V). This class is common and particularly vulnerable to hurricane winds; an example tower is shown in Fig. 3.4. Towers in this class also exhibit substantial structure-to-structure variability.

3.3.2 Efficient modeling of tower-line system

Fig. 3.5(a) shows a schematic of the tower-line system for the selected class of transmission towers, together with the orientation of the hurricane wind loads. High-fidelity models consisting of hundreds of members have traditionally been used to simulate such tower-line systems (Mohammadi Darestani et al., 2020; Ma et al., 2021a; Dikshit and Alipour, 2023). As discussed in Section 3.2.2, these models are computationally expensive, require detailed input data that are impractical to collect at the portfolio scale, and are unsuitable for efficient probabilistic simulation. This study proposes an efficient modeling approach for transmission tower-line systems. As illustrated in Fig. 3.5(b), the methodology is comprised of two parts: (1) treating cables as loads by directly simulating time histories of end forces at the attachment points rather than modeling the cables explicitly in the FE model; (2) representing panels as the basic structural components using physics-based surrogate analytical models, rather than modeling hundreds of individual members. Detailed descriptions of the two parts are provided below.

Recognizing that the cables, including both overhead ground wires (OHGW) and conductors, act as loads on the supporting towers, we treated the cables and the turbulent wind

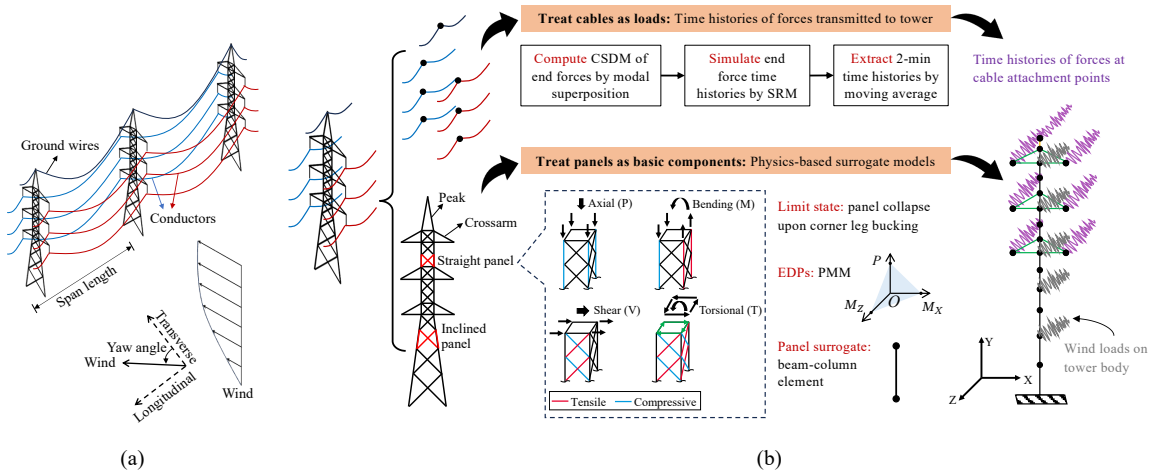

Figure 3.5: (a) Schematic of a transmission tower-line system under hurricane winds. (b) Efficient modeling of the transmission tower-line system (partially adapted from Wang and Bocchini (2025b)). All models considered are 3D although shown here in 2D for simplicity. Loads at cable attachments and on the tower body are shown schematically; in simulations, they are decomposed into three Cartesian directions. Illustrations are not to scale.

acting on them as applied loads, directly representing the forces transmitted at the attachment points. Previous studies have shown that the wind-induced response of cables can be approximated analytically using a modal superposition method, given that the behavior of the cables can be linearized around the static mean wind response (Wang et al., 2017a; Ma et al., 2021a; Wang and Bocchini, 2023). For details, readers are referred to these references. In this study, we extended this approach for class-scale modeling, accommodating any wire system configuration within the tower class. The implementation allows for variations in conductor and OHGW type, number of peaks (i.e., number of OHGWs), attachment point arrangement (vertical and horizontal), cable tension, span length, yaw angle, wind intensity, among others. The methodology primarily involves calculating the cross-spectral density matrix (CSDM) of the modal displacement vector:

$$\boldsymbol{S}_q(f) = \boldsymbol{H}(f)\,\boldsymbol{S}_Q(f)\left[\boldsymbol{H}^*(f)\right]^T \tag{3.6}$$

where $\boldsymbol{H}(f)$ is the transfer matrix encapsulating the structural properties of the cables linearized at their mean-wind state; f denotes frequency (Hz); $\boldsymbol{S}_Q(f)$ denotes the CSDM of

the generalized force vector and is a function of the wind spectrum and coherence function (Wang et al., 2017a). Invoking modal participation coefficients and performing further transformations allows computation of the CSDM of the end forces at all (seven or eight) attachment points, $\boldsymbol{S}_r(f)$. At each attachment, three force components along three directions—transverse, longitudinal, and vertical—are considered. With $\boldsymbol{S}_r(f)$, time history samples of the end forces can be generated via the spectral representation method (SRM) (Ma et al., 2021a; Deodatis, 1996), resulting in an ensemble of $7 \cdot 3 = 21$ (single-peak) or $8 \cdot 3 = 24$ (double-peak) correlated time histories.

For modeling the lattice transmission towers, this study adopts physics-based surrogate models of panels, which allows efficient panel-level FE modeling and panel-based tower failure analysis under hurricane winds (Wang and Bocchini, 2025b). As illustrated in Fig. 3.5(b), each tower can be effectively modeled by a series of beam-column elements, with each element capturing the mechanical behavior of one panel. Each panel (straight or inclined) is described using six abstract parameters: panel height (h_p), panel mass (m_p), axial stiffness (K_{sa}), bending stiffness (K_{sb}), torsional stiffness (K_{st}), and shear stiffness (K_{ss}). Crossarms and peak(s) are also included to transfer loads from the attachment points to the panels. For each 'panel component', the failure limit state is defined as corresponding to the buckling of any of the legs in compression. This can be quantitatively captured by three EDPs: the axial force (P) and the two bending moments (M_X, M_Z), collectively referred to as PMM. The PMM capacity surfaces are well approximated as planes (see Fig. 3.5(b)) and can be fully characterized by two quantities: $P_{\max}$ and $M_{X\max}(= M_{Z\max})$. The EDPs are obtained from FE analysis, while the PMM capacity planes are determined consistently via polynomial response surface metamodels (Wang and Bocchini, 2025b). The panel-oriented surrogate modeling approach is well suited for the tower class under study, and it captures the main mechanical failure mode of lattice transmission towers (i.e., leg buckling) which can trigger tower collapse. The approach has been rigorously cali-

brated and validated against high-fidelity models and demonstrates comparable accuracy in computing EDPs and fragility derivation (Wang and Bocchini, 2025b). The surrogate model enables highly efficient model creation and computation. This efficiency is especially valuable at the portfolio scale, where simulations of hundreds or thousands of towers are required. Furthermore, the surrogate model relies on only a small number of modeling parameters. As a result, we only need to calibrate a small set of probabilistic model parameters to capture structural variability across the portfolio. This greatly facilitates the uncertainty characterization and probabilistic simulation for uncertainty propagation (see Section 3.3.6).

3.3.3 Dynamic wind load analysis

First, we selected the 1-min MSWS as the intensity measure, primarily due to its hazard computability (recall Section 3.2.3). As shown in Fig. 3.5(b), the wind-induced loads consist of loads transmitted from the cables at the attachment points, and wind loads acting directly on the tower body. The simulated end force time histories are long ($>$ 60 min). Following the recommendation of Ma et al. (2021a), we extracted 2-min time histories that contain the one minute of turbulence associated with the MSWS. This 2-min window was identified using the moving average technique, representing the period of maximum dynamic loading on the tower (the most critical period during a hurricane). The load histories were then applied at the attachment points as nodal loads.

In addition to the cable-transmitted forces, wind also imposes direct loads on the tower body. For this purpose, we used the synthetic repository of wind velocity time histories developed by Khazaali et al. (2022). This repository provides wind samples across a broad range of intensities and up to a height of 60 m, which sufficiently covers typical transmission towers. Specifically, in consistency with the duration of the end force time histories, we used the 2-min long wind velocity time histories. These samples are organized by 1-min

MSWS, ranging from 19 m/s to 85 m/s in 1 m/s increments. To compute the wind loads on tower body, the tower is typically divided into segments (each consisting of multiple panels). The dynamic wind load on segment k at time t is then calculated as follows (Ma et al., 2021a; Wong and Miller, 2010):

$$F_{d,k}(t) = Q\left[V_{w,k}(t) - V_k(t)\right]^2 \left[1 + 0.2\sin^2(2\Psi)\right] \left(C_{\mathrm{ft},k} A_{\mathrm{mt},k} \cos^2\Psi + C_{\mathrm{fl},k} A_{\mathrm{ml},k} \sin^2\Psi\right) \tag{3.7}$$

where Q denotes the air density coefficient; $V_{w,k}(t)$ denotes the wind velocity fluctuation at time t regarding segment k; $V_k(t)$ is the velocity at the centroid of segment k at time t and is obtained from FE analysis; Ψ is the yaw angle; $C_{\mathrm{ft},k}$ and $C_{\mathrm{fl},k}$ represent the transverse and longitudinal force coefficients for segment k, respectively; $A_{\mathrm{mt},k}$ and $A_{\mathrm{ml},k}$ represent the net areas of segment k in the transverse and longitudinal directions, respectively. It should be noted that the wind load here is computed using the difference between the wind velocity fluctuations and the velocity of the tower components, a simplified approach commonly used to account for aerodynamic damping (Holmes, 2007; Yasui et al., 1999). Moreover, Eq. (3.7) gives the resultant force, which was then decomposed into transverse and longitudinal directions based on the yaw angle. As customary, the calculated wind loads on each segment were applied at the node closest to the segment's centroid.

Dynamic time history analysis was performed in OpenSees (McKenna et al., 2010) to apply the two wind-induced loads with a time step of 0.01 sec. The Newton-Raphson algorithm was adopted for the solution procedure, and the Newmark average-acceleration method was employed as the integrator. Convergence was checked using the relative energy increment criterion with a tolerance of 10^{-5}. At each time step, the demand placed on each panel (or panel response) was compared to its limit capacity. The failure limit state of the j^{th} panel in the tower is determined by:

$$\ell_j = P_{\mathrm{PMM}_j}(M_{X,j},\, M_{Z,j}) - P_j \tag{3.8}$$

where $j = 1, 2, \ldots, n_c$ for a tower consisting of n_c panels; $P_{\text{PMM}_j}(M_{X,j},\ M_{Z,j})$ represents the axial force capacity of panel j, as determined from the PMM limit capacity plane under the bending moments $M_{X,j}$ and $M_{Z,j}$; and P_j denotes the axial demand on panel j. Given that panel failure can trigger global instability and ultimately tower collapse, the tower (a multi-component system) limit state is determined by treating it as a series system (Wang and Bocchini, 2025b):

$$\mathscr{L} = \cup\, \ell_j \leq 0 = \min(\ell_1,\ \ldots\ ,\ \ell_{n_c}) \leq 0 \tag{3.9}$$

3.3.4 Selected tuning parameters

For the considered class of transmission towers in Florida, five tuning parameters ($\boldsymbol{X}^{\text{II}}$) were pre-selected a priori to parameterize the class fragility model: voltage, design wind speed, number of peaks (i.e., number of OHGW), span length, and yaw angle. Table 3.1 summarizes these parameters along with the valid ranges considered in this study. Importantly, all five tuning parameters are known or easily accessible, with example data sources (not exhaustive) indicated in Table 3.1. This ensures the direct usability of the parameterized fragility model. The 500 kV lines were excluded because this class of towers is not used at that voltage, according to the data collection (Section 3.3.1). The 69 kV lines were also omitted, as they are typically classified as sub-transmission, and the use of lattice towers in such lines is expected to be negligible. The design wind speeds considered here are 3-sec gusts based on wind maps of a 50-year return period ($T_r = 50$) (Wong and Miller, 2010), reflecting that the vast majority of the existing transmission towers were designed according to these earlier standards. It should be noted that the actual design wind speed for a tower may vary from the basic wind map values due to local regulations or project-specific requirements. The number of peaks (corresponding to the number of OHGW) can be one or two. The span length levels were determined from the 230 kV line data collection,

Table 3.1: Selected five tuning parameters for the class of transmission towers.

Parameter	Notation	Range	Number of variations	Example data source
Voltage	X_1^{II}	115, 138, 230 kV	3	GIS data (Homeland Infrastructure Foundation-Level Data (HIFLD), 2022)
Design wind speed	X_2^{II}	90, 100, ..., 150 mph (40, 45, ..., 67 m/s)	7	Basic wind speed map (Wong and Miller, 2010)
Number of peaks	X_3^{II}	1, 2	2	GIS-based mapping (Section 3.3.1)
Span length	X_4^{II}	400, 500, ..., 1400 ft (122, 152, ..., 427 m)	11	GIS-based mapping (Section 3.3.1)
Yaw angle	X_5^{II}	$0^\circ, 15^\circ, \ldots, 90^\circ$	7	GIS data (Homeland Infrastructure Foundation-Level Data (HIFLD), 2022), hurricane wind map (National Hurricane Center, 2025)

but they are representative of typical values for other voltages as well (Wong and Miller, 2010). The yaw angle depends on both the orientation of the transmission line and the relevant wind direction; the latter may be obtained from a hazard module or hurricane wind map. Consistent with common practice, the yaw angle was considered in 15° intervals (Ma et al., 2021a; Dikshit and Alipour, 2023; Cai et al., 2019).

From a fragility perspective, the selection of design wind speed, span length, and yaw angle was informed by previous studies, which have demonstrated their significant influence on tower fragility (Ma et al., 2021a; Cai et al., 2019). Although no direct evidence links voltage to tower fragility, it was included because supporting structure design is governed by the electrical function (Kalaga and Yenumula, 2017). The number of peaks was selected due to the significant contribution of cable loads to the overall loading. The actual influence of these two parameters on fragility outcomes is assessed in Section 3.3.9.

3.3.5 Experimental designs

Considering the five tuning parameters and their variations listed in Table 3.1, the full input space comprises 3234 combinations. To strategically and economically cover this space, we applied the generalized subset design (GSD) technique (Anderson et al., 2020), which generalizes traditional fractional factorial designs to factors with more than two levels, as in our case. A reduction factor of 6 was specified, reducing the number of experiments to 538 ($n_s = 538$). Thus, to obtain the functional relationships between the tuning parameters and the lognormal parameters, $\hat{\theta}(\mathbf{x}^{\mathrm{II}})$ and $\hat{\beta}(\mathbf{x}^{\mathrm{II}})$, the inputs are given by the 538 DoE points in $\mathscr{X} = \{\boldsymbol{x}_1^{\mathrm{II}}, \ldots, \boldsymbol{x}_{538}^{\mathrm{II}}\}$, with $\boldsymbol{x}_i^{\mathrm{II}} \in \mathbb{R}^5$, and the corresponding outputs are $\boldsymbol{\vartheta} = [\theta_1, \ldots, \theta_{538}]$ and $\boldsymbol{\beta} = [\beta_1, \ldots, \beta_{538}]$.

3.3.6 Uncertainty modeling of the tower class

As mentioned in Section 3.2.6, uncertainty characterization should be carried out for each DoE point to obtain the joint distribution of the Type III uncertain variables, denoted as $F^i_{\boldsymbol{X}^{\mathrm{III}}}(\boldsymbol{x}^{\mathrm{III}})$, $i = 1, 2, \ldots, 538$. There are several challenges in characterizing the uncertainty of tower modeling parameters (e.g., stiffnesses, capacities). Beyond some basic information, real tower data are largely unavailable. Moreover, unlike well-studied frame structures for which rulesets exist to translate generic building information into model-ready parameters, no such empirical rules have been established for transmission towers. As a result, directly assigning uncertainties to the modeling parameters would be infeasible or highly unreliable if based solely on judgment. To address these challenges, Section 3.3.6.1 introduces a novel approach that transforms uncertainty of transmission line design variables into uncertainty of surrogate-compatible modeling parameters through a dedicated design module and conversion step. Specifically, we characterize uncertainty in transmission line design parameters, for which more data are available and confidence is higher. These un-

certainties are propagated through the tower design module to generate batches of synthetic tower designs. The resulting raw design data are then converted into surrogate-compatible modeling parameters, thereby transforming the uncertainties from the design parameter space into the Type III parameter space.

Section 3.3.6.2 presents the uncertainty characterization using the post-converted batch tower modeling parameters. First, interpolation rules are established to reduce the number of uncertain parameters to a fixed set of 23. These 23 parameters comprehensively capture the modeling and analysis of the entire tower class; they include both mechanical and capacity parameters, explicitly accounting for component damage dependency. Finally, the joint distribution of these 23 parameters at each DoE point is obtained through statistical inference, with a Gaussian copula employed to represent the dependence structure.

3.3.6.1 Generation of tower designs incorporating design uncertainty

The use of the design module for generating synthetic tower designs and transforming design uncertainty is illustrated in Fig. 3.6. The process begins by characterizing the uncertainty in transmission line design variables for each DoE point. In total, seven primary design variables (grouped into three design phases) were identified based on available literature and judgment, with their probabilistic distributions summarized in Table 3.2. All seven variables were assumed to be mutually independent. Note that Table 3.2 applies to all 538 DoE points. For each DoE point, the LHS technique was employed to generate samples of the design variables, with each realization corresponding to a tower design produced by the design module. Since the seven variables include a mix of categorical, continuous, and discrete types, the LHS implementation from *SMT* (Saves et al., 2024) was used to handle this heterogeneity.

The cable design precedes and dictates the design of supporting towers. Conductor

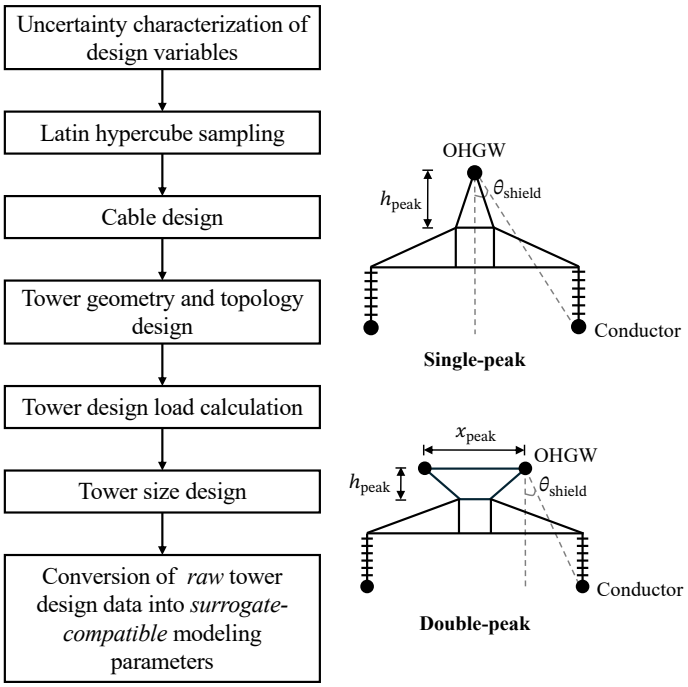

Figure 3.6: Flowchart of transforming design variable uncertainty into surrogate modeling parameter uncertainty through tower design and data conversion. The single-peak and double-peak drawings are illustrative only and not to scale.

Table 3.2: Uncertain design variables with corresponding probabilistic distributions.

Design aspect	Design variable	Notation	Type	Distribution
Cable design	Conductor	–	Categorical	Uniform on conductor database (Table D.1)
	OHGW	–	Categorical	Uniform on OHGW database (Table D.2)
	Tension percentage (%)	p_{T}	Continuous	Triangular $(15, 20, 25)$
Tower geometry and topology	Shield angle (°)	θ_{shield}	Continuous	Uniform $(20, 30)$
Tower size	Coefficient in Ryle's formula for tower weight	k_{W}	Continuous	Uniform $(0.0014, 0.0018)$
	Number of different leg sizes in a tower	n_{ls}	Discrete	Uniform $(2, 6)$
	Number of different brace sizes in a tower	n_{bs}	Discrete	Uniform $(2, 6)$

and OHGW were assumed to follow uniform distributions based on the databases provided in Appendix D. Note that the applicable conductor database depends on the line voltage, following the minimum conductor size recommendations (U.S. Department of Agriculture, Rural Utilities Service, 2015). The tension percentage refers to the horizontal cable tension (T_h), relative to its rated tensile strength (RTS): $T_h = p_{\mathrm{T}} \cdot \mathrm{RTS}$. This tension percentage is typically set around 20% (CIGRÉ Study Committee B2, 2016), and a triangular distribution with a mode of 20% was assumed in this study.

The tower design can be divided into three aspects: geometry, topology, and sizing, and an in-house code was developed following relevant standards and practices. While detailed procedures are omitted here, a high-level overview is provided below. The geometry and topology design are primarily governed by electrical requirements, such as shielding angle and various electrical clearances. The shielding angle, illustrated in Fig. 3.6, determines how the OHGW protects the conductors from lightning strikes. Its value influences geometric dimensions such as crossarm widths and was assumed to follow a uniform distribution based on typical industry values (Kalaga and Yenumula, 2017). Typical values for various clearances were adopted from the literature (Kalaga and Yenumula, 2017; U.S. Department of Agriculture, Rural Utilities Service, 2015). For double-peak towers, the peak height (h_{peak}) was set to a nominal value of 1 ft (0.3048 m), while the horizontal separation between two ground wires (x_{peak}) varies according to design. For single-peak towers, h_{peak} may vary, while $x_{\mathrm{peak}} = 0$. The design loads were computed considering two extreme wind load cases (Wong and Miller, 2010): one with a yaw angle of 0° and the other with 30°. As is common practice in tower design, the entire tower was treated as a single segment with a uniform solidity ratio and a uniform net area for the purpose of load calculation. Based on typical reference values from the literature (Wong and Miller, 2010; Tapia-Hernández and Sordo, 2017; Mara, 2013), we used a uniform solidity ratio $\varepsilon = 0.25$ (corresponding to a force coefficient of 2.775 by $4\varepsilon^2 - 5.9\varepsilon + 4$), and a unit uniform net area $\bar{A}_m = 0.55\ \mathrm{m}^2/\mathrm{m}$.

The tower size design is governed by structural requirements (ASCE, 2015). The Ryle's formula was used to estimate the tower weight during the preliminary design stage (Ryle, 1946):

$$W_{\text{tower}} = k_{\text{W}} \cdot H_{\text{tower}} \cdot \sqrt{M_{\text{GL}}} \tag{3.10}$$

where k_{W} is a coefficient assumed to follow a uniform distribution based on typical values; H_{tower} is the tower height; and M_{GL} denotes the overturning moment at the ground line. Moreover, along the tower height, from bottom to top, the structure not only tapers in its geometric dimensions but also typically employs progressively smaller leg and bracing members. Consequently, multiple leg and bracing sizes can exist within a single tower. In this study, both the number of leg sizes (n_{ls}) and the number of bracing sizes (n_{bs}) were assumed to follow a uniform distribution on $(2,6)$, based on literature and engineering judgment (Ma et al., 2021a; Dikshit and Alipour, 2023; Mara, 2013). To ensure design realism, it was further enforced that leg members are always larger than or equal to bracing members within the same panel.

The design module outputs raw tower design data, including geometric dimensions and the sizes of leg and bracing members. For each panel surrogate (see Section 3.3.2), six mechanical parameters are needed: h_p, m_p, K_{sa}, K_{sb}, K_{st}, and K_{ss}. In addition, two capacity parameters, P_{max} and $M_{X,\text{max}}$, are required to fully define the panel's PMM capacity plane. We employed rigorous conversion equations (for K_{sa}, K_{sb}, and K_{st}) together with response surface metamodels (for K_{ss}, P_{max}, and $M_{X,\text{max}}$) to translate the raw tower data into surrogate-compatible modeling parameters (Wang and Bocchini, 2025b). The metamodels were derived for two panel types (straight and inclined) to predict the surrogate modeling parameters and PMM capacity planes consistently, using five inputs: panel top width (w_t), leg sectional area (A_{leg}), brace sectional area (A_{brace}), connection slippage length (l_{slip}), and the yield stress of ASTM A36 steel (F_y). For a given tower, the first three inputs were supplied directly by the tower design module. The slippage length was randomly sampled

from a uniform distribution (lower bound = 0.31 mm, upper bound = 2.33 mm) and applied consistently across all panels within the tower (Ungkurapinan, 2000). Similarly, the yield stress was sampled from a lognormal distribution (mean = 290.0 MPa, standard deviation = 29.0 MPa) and was also applied consistently to all panels within the tower.

3.3.6.2 Statistical inference of joint distributions

Using the post-converted batch tower modeling parameters, a joint distribution is now sought for each DoE point to represent the corresponding uncertainty. However, two challenges arise. First, the number of panels varies among towers, so the number of Type III parameters is not fixed. This variability renders the derivation of the joint distribution non-tractable. Second, even with the surrogate modeling approach, a single tower may still involve a large number of parameters, making the derivation of the high-dimensional joint distribution challenging.

To overcome the aforementioned challenges, interpolation rules based on two reference panels were proposed. Due to the tapering geometry and decreasing member sizes from bottom to top, panel parameters within the same tower exhibit discernible trends. Fig. 3.7 illustrates the variations of the eight parameters along the panels for two example towers. Panel numbering starts from 1 at the bottom and increases upward. Tower 1 has 12 panels (five straight and seven inclined), while Tower 2 has eight panels (three straight and five inclined). Parameters of all straight panels show minimal variation, whereas those of inclined panels display more pronounced variation, following predictable patterns that can be approximated using linear, quadratic, or cubic functions. Similar trends were consistently observed across the generated batch tower designs; the two examples are shown here for clearer visualization. Therefore, we proposed two reference panels: the bottom straight panel (the lowest straight panel in the straight tower body) and the bottom inclined panel (the bottom panel of the entire tower). Guided by the observed trends and the physical

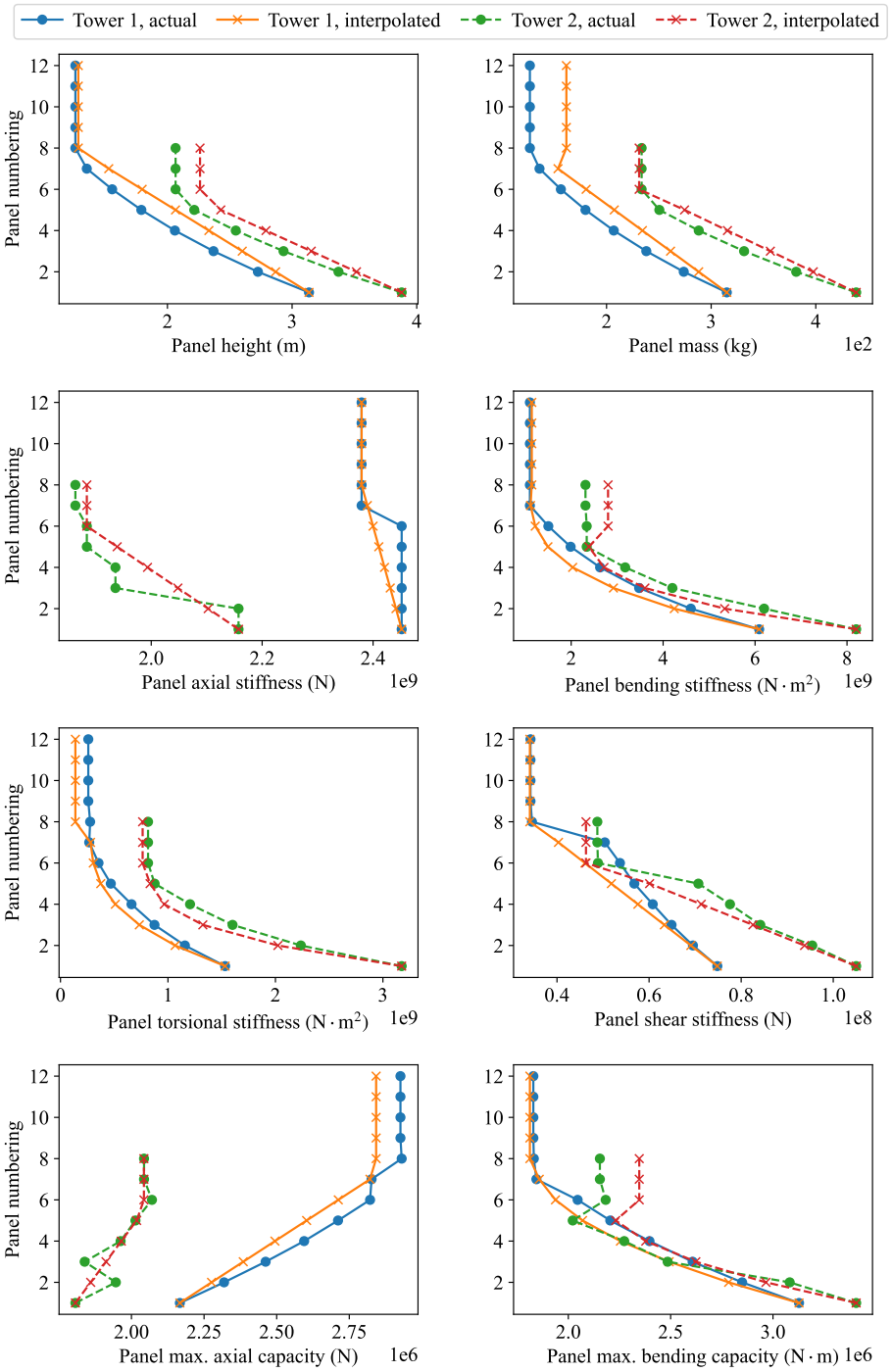

Figure 3.7: Actual and interpolated variation of surrogate modeling parameters across panels along the tower height for two example towers.

meaning of the parameters, we established the following rules. Let v_{inc} and v_{str} denote any of the eight parameters of the reference bottom inclined panel and the reference bottom straight panel, respectively. For a given tower, the parameters of all straight panels were assumed equal to the corresponding parameters of the reference bottom straight panel (v_{str}). For inclined panels, let λ denote the panel number whose parameters are to be interpolated, and let v_λ represent any generic parameter of that panel. Different interpolation functions were applied to different parameters. Specifically, linear interpolation was used for h_p, m_p, K_{sa}, K_{ss}, $P_{\max}$, as follows:

$$v_\lambda = v_{\text{inc}} - \frac{\lambda - 1}{\lambda_{\text{str}} - 1}(v_{\text{inc}} - v_{\text{str}}) \tag{3.11}$$

where λ_{str} denotes the panel number of the reference bottom straight panel. We proposed quadratic interpolation for $M_{X\max}$, as follows:

$$v_\lambda = v_{\text{str}} + \left(\frac{\lambda - \lambda_{\text{str}}}{1 - \lambda_{\text{str}}}\right)^2 (v_{\text{inc}} - v_{\text{str}}) \tag{3.12}$$

Finally, cubic interpolation was used for K_{sb} and K_{st}:

$$v_\lambda = v_{\text{str}} + \left(\frac{\lambda - \lambda_{\text{str}}}{1 - \lambda_{\text{str}}}\right)^3 (v_{\text{inc}} - v_{\text{str}}) \tag{3.13}$$

Fig. 3.7 also compares the actual and interpolated values for the two example towers. While the interpolation is not perfect, the interpolated values closely follow the actual values and preserve the general trends well. A few points are worth noting. First, the slight loss of accuracy is considered acceptable in the context of portfolio-scale analysis, where inter-structure variability typically dominates and several approximations already exist (e.g., surrogate modeling, curve fitting). Second, this interpolation is specifically intended to address the two challenges in deriving joint distributions for class-scale analyses;

Table 3.3: Type III parameters for the class of transmission towers.

Parameter	Unit	Notation	Type
x_{peak} if double-peak (h_{peak} = 1 ft); h_{peak} if single-peak (x_{peak} = 0)	m	X_1^{III}	Continuous
Width of cross-arms	m	X_2^{III}	Continuous
Number of straight panels	–	X_3^{III}	Discrete
Number of inclined panels	–	X_4^{III}	Discrete
Height of the bottom straight panel	m	X_5^{III}	Continuous
Mass of the bottom straight panel	kg	X_6^{III}	Continuous
Axial stiffness of the bottom straight panel	N	X_7^{III}	Continuous
Bending stiffness of the bottom straight panel	$\text{N}\cdot\text{m}^2$	X_8^{III}	Continuous
Torsional stiffness of the bottom straight panel	$\text{N}\cdot\text{m}^2$	X_9^{III}	Continuous
Shear stiffness of the bottom straight panel	N	X_{10}^{III}	Continuous
Maximum axial capacity of the bottom straight panel	N	X_{11}^{III}	Continuous
Maximum bending capacity of the bottom straight panel	$\text{N}\cdot\text{m}$	X_{12}^{III}	Continuous
Height of the bottom inclined panel	m	X_{13}^{III}	Continuous
Mass of the bottom inclined panel	kg	X_{14}^{III}	Continuous
Axial stiffness of the bottom inclined panel	N	X_{15}^{III}	Continuous
Bending stiffness of the bottom inclined panel	$\text{N}\cdot\text{m}^2$	X_{16}^{III}	Continuous
Torsional stiffness of the bottom inclined panel	$\text{N}\cdot\text{m}^2$	X_{17}^{III}	Continuous
Shear stiffness of the bottom inclined panel	N	X_{18}^{III}	Continuous
Maximum axial capacity of the bottom inclined panel	N	X_{19}^{III}	Continuous
Maximum bending capacity of the bottom inclined panel	$\text{N}\cdot\text{m}$	X_{20}^{III}	Continuous
Conductor	–	X_{21}^{III}	Categorical
OHGW	–	X_{22}^{III}	Categorical
Tension percentage	%	X_{23}^{III}	Continuous

for single-tower analyses, the joint distribution is not required and interpolation could be avoided. Third, these interpolation functions share the same spirit as the rulesets used in buildings, such as assuming uniform distributions for mass and stiffness across stories (Yi et al., 2025; Lu et al., 2020). Our approach may also provide guidance for other slender lattice structures, such as telecommunication towers. Finally, the joint distribution $F^i_{\boldsymbol{X}^{\text{III}}}(\boldsymbol{x}^{\text{III}})$ pertains to a fixed set of 23 Type III parameters, as summarized in Table 3.3. Note that the last three parameters also belong to the design uncertain variables introduced in Section 3.3.6.1. They are included in this joint distribution to capture the correlation between the tower structure and the loads transmitted from the cables (i.e., the tower–line system).

The joint distribution $F^i_{\boldsymbol{X}^{\text{III}}}(\boldsymbol{x}^{\text{III}})$ was obtained by statistical inference from the batch data generated for the i^{th} DoE point. We adopted the copula formalism to represent this multi-

variate distribution, using a Gaussian copula to capture the dependence structure among the 23 parameters (see Section 3.2.6). Statistical inference thus involved two steps: (1) fitting the marginals $F^i_{X^{\text{III}}_1}(x^{\text{III}}_1), \ldots, F^i_{X^{\text{III}}_{23}}(x^{\text{III}}_{23})$, and (2) estimating the Gaussian copula $\mathbb{C}^i$. For the last three parameters in Table 3.3, the marginals were already prescribed (see Table 3.2), so only copula inference was required to capture tower–line correlation. For marginal inference of the remaining 20 parameters, an automated approach was used (Lataniotis et al., 2015): each parameter was fitted to 12 candidate distributions ('Uniform', 'Normal', 'Log-normal', 'Gumbel', 'GumbelMin', 'Weibull', 'Gamma', 'Exponential', 'Beta', 'Triangular', 'Logistic', 'Laplace', 'Rayleigh'). The best-fitting distribution was selected using the Akaike Information Criterion (AIC). To avoid nonphysical values, fitted marginals were treated as truncated distributions within the observed data range. The Gaussian copula parameters were then estimated via Spearman's correlation coefficients among all pairs of random parameters. For each DoE point, 800 tower designs were generated to ensure stable statistical inference of both marginals and the copula. This sample size is an artifact of relying on a synthetic repository. Ideally, such statistical inference would be performed using actual inventory data.

Fig. 3.8 shows the joint distribution for one DoE point, including both the marginals and the copula. Overall, the 23 parameters exhibit non-negligible dependence. In particular, the 16 parameters from the two reference panels are mostly positively and strongly correlated, which is expected given the trends observed. This highlights the necessity of accounting for component demand and capacity correlations to ensure reliable damage analysis. In total, 538 joint distributions were obtained for the 538 DoE points. These enable efficient probabilistic simulation by supporting direct correlated sampling.

A summary of the sources of uncertainty for the class of transmission towers is provided as follows. The joint distributions of the 23 Type III parameters capture uncertainties transformed from the design variables and therefore represent structural uncertainty—both

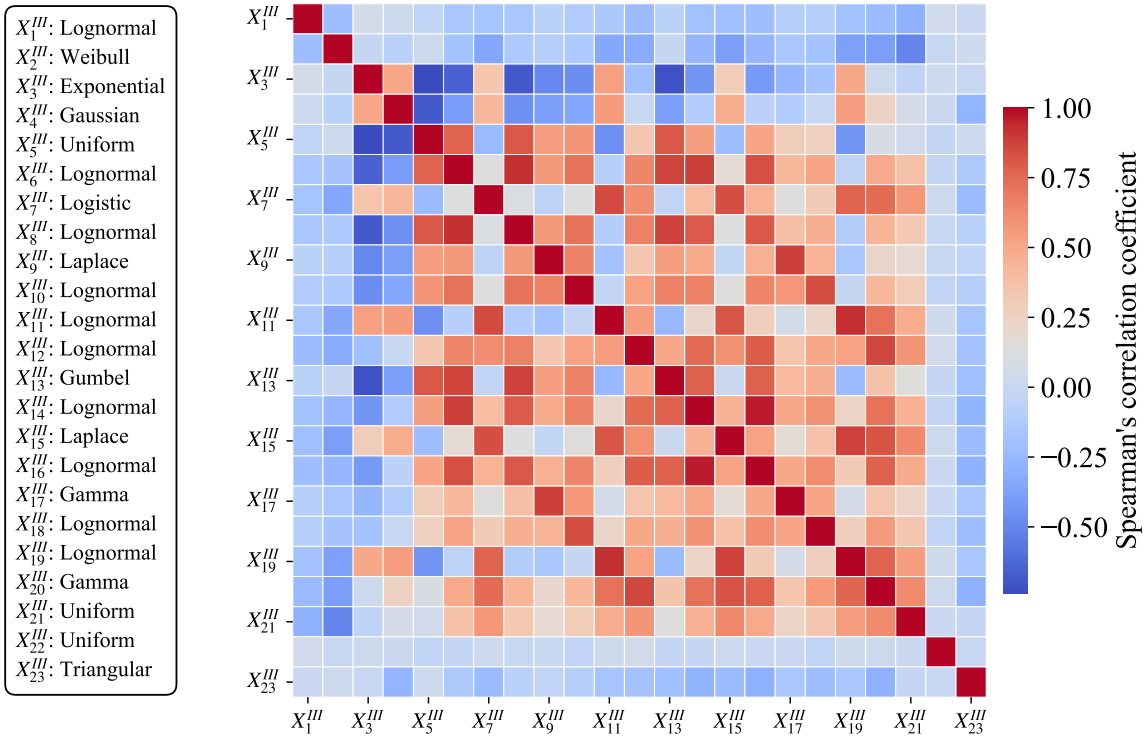

Figure 3.8: Example joint distribution at one design of experiments point. To avoid clutter, only the distribution types of the 23 marginals are shown; fitted parameters are omitted.

inter-structure and intra-structure, although the former typically dominates. Among these, the conductor, OHGW, and tension percentage are associated with load uncertainty, since cables are treated as external loads. Load uncertainty also arises from wind velocity turbulence acting directly on the tower body. The next section turns to the propagation of these uncertainties at each DoE point.

3.3.7 Dominance-guided uncertainty propagation

To propagate and embed uncertainty into the fragility curve for each DoE point, forward uncertainty propagation can be carried out through sampling. In our case, this requires correlated sampling from the joint distribution of the 23 Type III parameters, with each sample corresponding to a tower realization. In parallel, load uncertainty is propagated by sampling wind velocity histories from the repository for loads acting directly on the tower body, as well as simulated end force histories for loads transmitted from cables to the tower. An initial consideration before uncertainty propagation is the choice of data collection strategy for fragility derivation. To this end, we adopted an approach similar to that of Shinozuka et al. (2000) or multiple stripe analysis. This strategy was chosen for its ease of implementation and the flexibility it offers: intensity levels can be freely specified, and different load inputs may be used across intensity levels.

With the chosen strategy, uncertainty propagation involves three key considerations: (1) the number of structures (towers) to sample, (2) the number of load samples, and (3) the pairing scheme between sampled structures and loads for DTHA. At each DoE point, we considered intensity levels from 20 m/s to 80 m/s at 1 m/s intervals. A total of 100 intensity levels were sampled over this range and paired with 100 towers sampled via LHS from the joint distribution. Each tower was then subjected to three wind velocity time histories and three end force time histories, resulting in three DTHA per tower at the corresponding intensity. In total, 300 DTHA were performed to derive the fragility curve at each DoE point.

The above decisions were guided by uncertainty dominance—we prioritized the dominant source of uncertainty in order to achieve efficient yet reliable propagation. Comparative studies were conducted to examine the relative importance of structural versus load uncertainties by varying the number of structural and load samples. Fig. 3.9 illustrates one such study at a DoE point, comparing six cases and their corresponding fragility curves. The results show that the size of the load samples has a stronger influence on the fragility curves when only 50 structures are sampled than when 100 structures are used. This indicates that once a sufficient number of structures are sampled—thereby adequately propagating inter-structure uncertainty—the effect of additional load samples becomes small, as inter-structure uncertainty dominates over load uncertainty. Moreover, when taking the case '100 structures, 3 DTHA' as the reference, using only 50 structure samples leads to convergence toward a fragility curve that deviates from this benchmark, even if more load samples are added. This represents a more critical error than undersampling loads. This underscores that recognizing and prioritizing the dominant source of uncertainty in propagation is not only a matter of efficiency but also of correctness. Insufficient propagation of the dominant source can lead to misleading convergence of fragility estimates. Fig. 3.9 also shows the convergence of the two lognormal parameters for the case '100 structures, 3 DTHA'. Both parameters stabilize at around 100 structures, confirming adequate propagation of inter-structure uncertainty. Similar convergence checks were performed and verified at multiple DoE points, though are not shown here.

The fragility curves were fitted using the maximum likelihood method (Shinozuka et al., 2000; Baker, 2015), as illustrated in Fig. 3.10. Since each structure is paired with three loads (i.e., three DTHA), the per-structure failure fraction can take values of 0, $1/3$, $2/3$, or 1. Multiple structures may fall at the same IM level due to the sampling and pairing scheme. Consequently, the overall failure fraction (used for curve fitting) at an IM level depends on the number of structures present at that level.

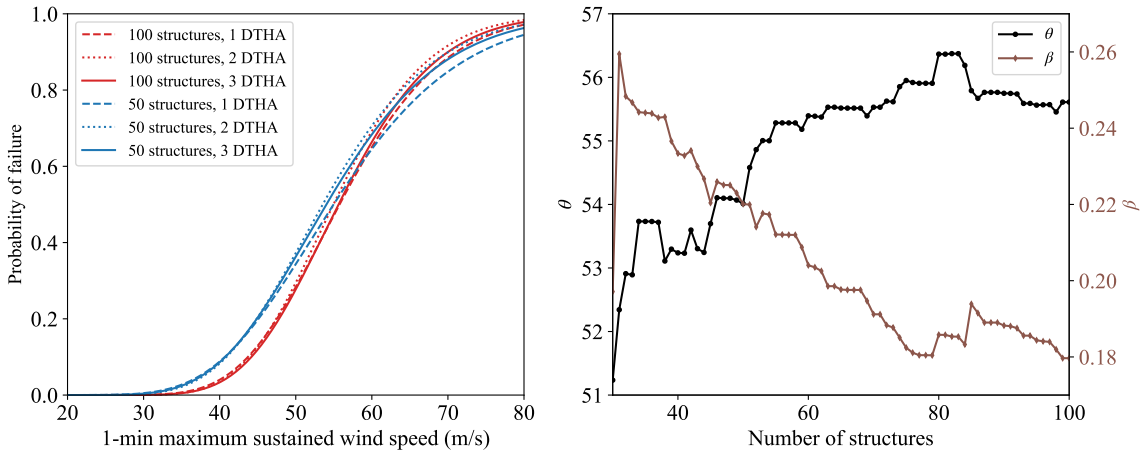

Figure 3.9: Comparison of different uncertainty propagation setups and their resulting fragility curves.

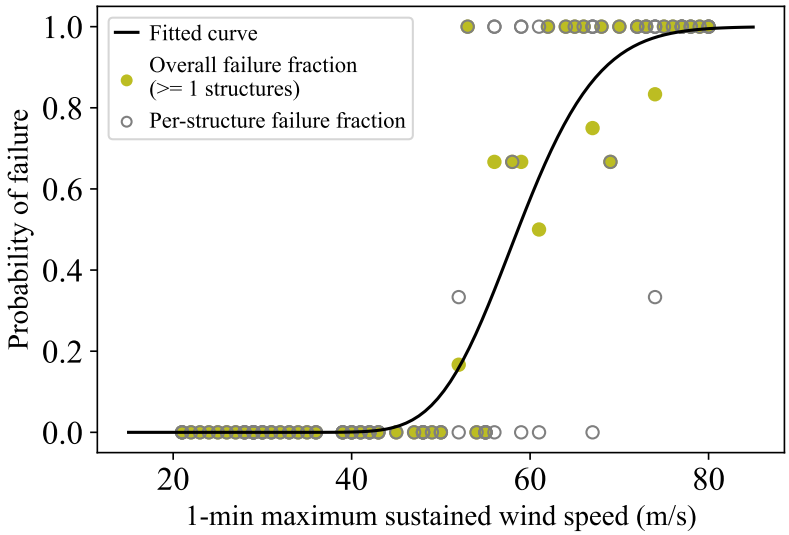

Figure 3.10: Example of fragility curve fitting.

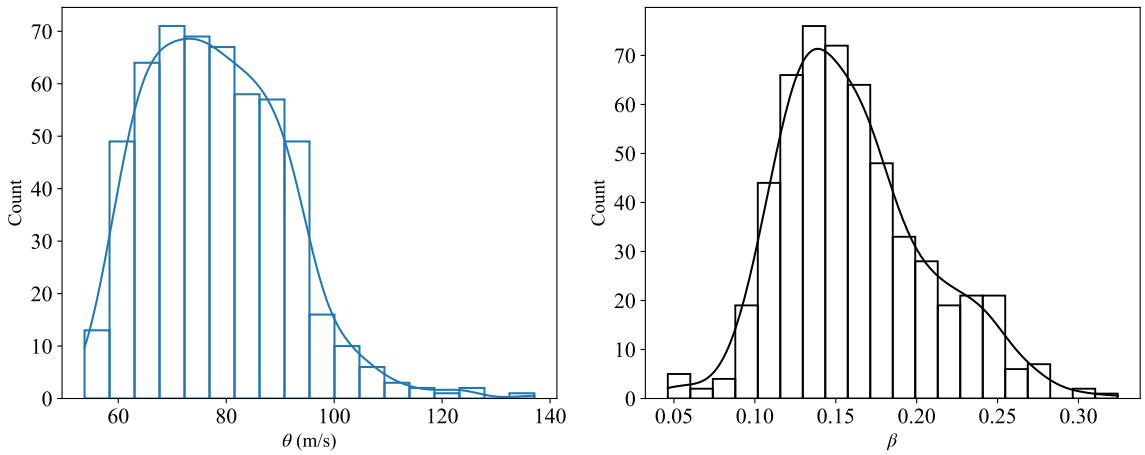

Figure 3.11: Histograms of θ and β with overlaid kernel density estimates.

3.3.8 Comparison of metamodels

Using the dominance-guided uncertainty propagation strategy, 538 fragility curves were obtained, yielding $\boldsymbol{\vartheta} = [\theta_1, \ldots, \theta_{538}]$ and $\boldsymbol{\beta} = [\beta_1, \ldots, \beta_{538}]$. Fig. 3.11 shows their histograms, where θ ranges from about 54 to 137 m/s and β from about 0.05 to 0.3. To identify optimal functional relationships from the input–output pairs $\{\mathscr{X}, \boldsymbol{\vartheta}\}$ and $\{\mathscr{X}, \boldsymbol{\beta}\}$, we compared four metamodeling methods: PRS, RF, XGBoost, and SVR (see Section 3.2.8). Model performance was evaluated using R^2 and MAPE. For PRS, four polynomial degrees (PRS1–PRS4) were tested, with lasso regression employed for automatic predictor selection. SVR was implemented using a radial basis function kernel, denoted SVR (RBF). Hyperparameters for all metamodels were tuned via grid search.

Fig. 3.12 and Fig. 3.13 show the performance of the metamodels for θ and β, respectively. The variation in performance with different training–testing splits is also displayed for convenient assessment, given the relatively small dataset. Fig. 3.12 indicates that PRS1 exhibits the lowest performance for θ prediction, while the other metamodels achieve similarly high accuracy across splits. Recall that θ represents the median corresponding to 50% failure probability. The strong prediction performance is likely due to the high relevance of

the chosen tuning parameters, such as design wind speed and yaw angle. No single metamodel clearly outperforms the others when considering both R^2 and MAPE across training and testing sets. In contrast, prediction of β is generally less accurate. Comparison of R^2 and MAPE scores between training and testing sets indicates varying degrees of overfitting, and the training-testing split has an important effect on performance. Recall that β is a dispersion parameter, with smaller values yielding steeper fragility curves and larger values producing flatter curves. The lower prediction accuracy for β is likely due to its weak direct relationship with the five tuning parameters. Among the PRS models of varying degrees, performance is generally inferior to that of RF, XGBoost, and SVR. Similarly, no single metamodel consistently outperforms the others across both R^2 and MAPE metrics.

To assess the impact of β prediction performance on the fragility curves, four hypothetical cases were considered by pairing the maximum and minimum values of θ and β (Fig. 3.11): $\theta = 54, \beta = 0.05$; $\theta = 54, \beta = 0.3$; $\theta = 137, \beta = 0.05$; and $\theta = 137, \beta = 0.3$. Based on the MAPE values in Fig. 3.13(a)-(b), a 10% deviation in β was assumed, generating artificially increased and decreased β values for each case. Fig. 3.14 illustrates the effect of these deviations on the fragility curves. When β is small ($= 0.05$), a 10% deviation has negligible impact regardless of θ value, as the curves are already steep. For larger β ($= 0.3$), the same deviation produces more noticeable differences, especially at higher θ. Overall, the fragility curves remain reasonably robust despite these deviations, consistent with the general understanding that θ primarily governs the fragility (first-order effect), while β has a secondary influence (second-order effect) (American Nuclear Society, 1982; Shinozuka et al., 2000).

3.3.9 Results and discussion

We shared all metamodels trained with a 90%-10% training-testing split at `https://doi.org/10.5281/zenodo.17504411`. Users may select any of these metamodels based on

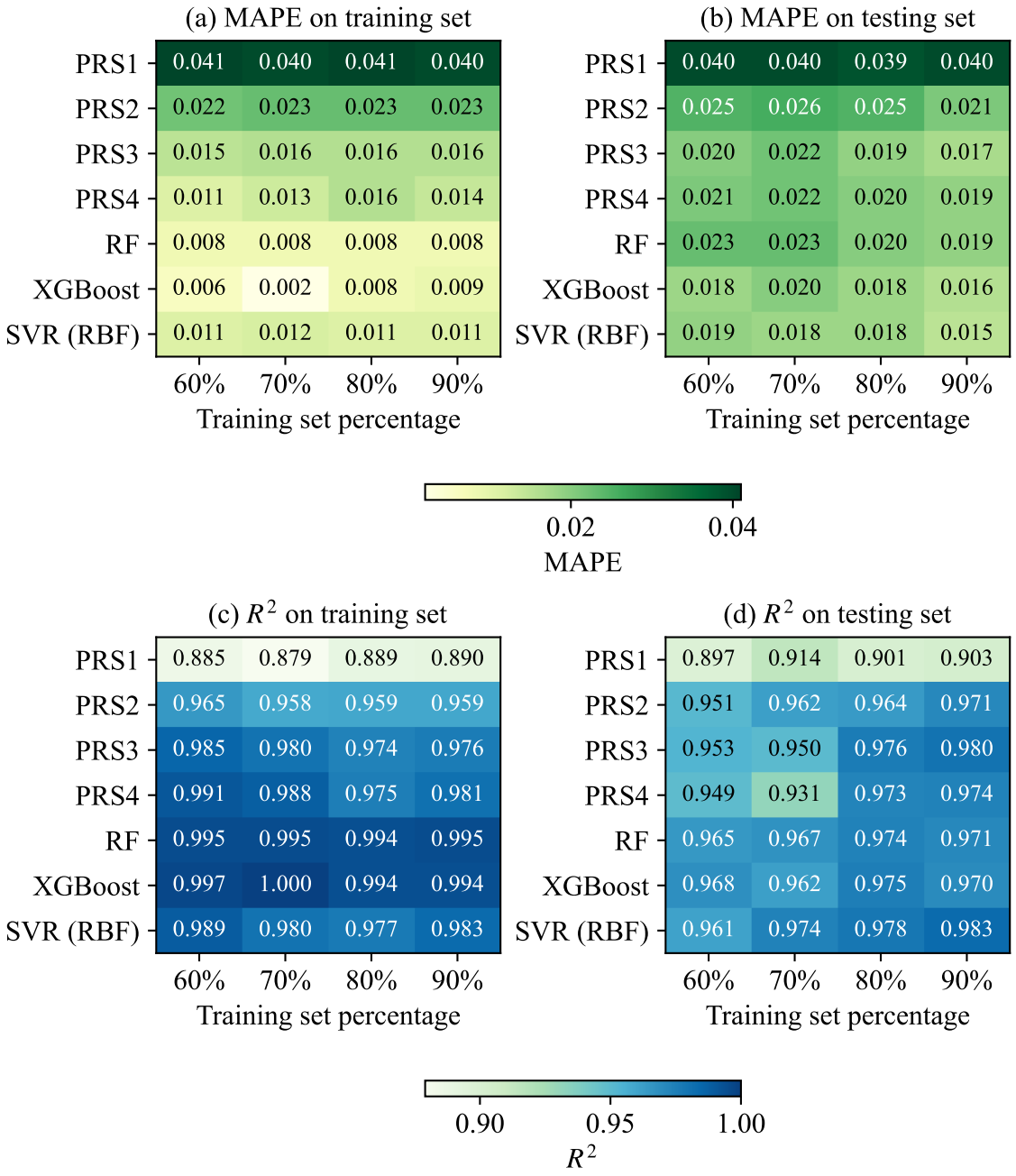

Figure 3.12: Performance of metamodels for θ prediction: (a) MAPE on training set; (b) MAPE on testing set; (c) R^2 on training set; (d) R^2 on testing set.

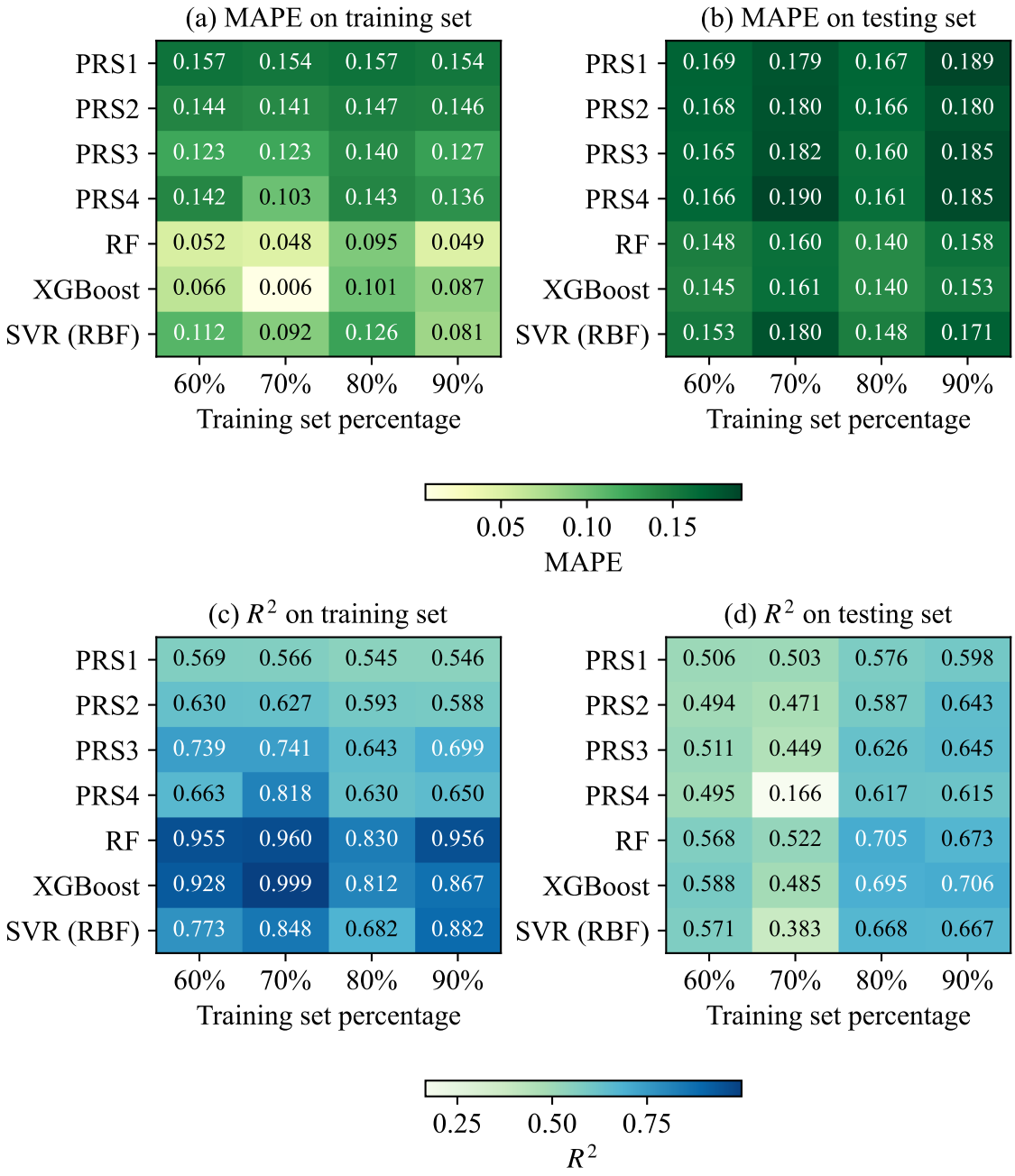

Figure 3.13: Performance of metamodels for β prediction: (a) MAPE on training set; (b) MAPE on testing set; (c) R^2 on training set; (d) R^2 on testing set.

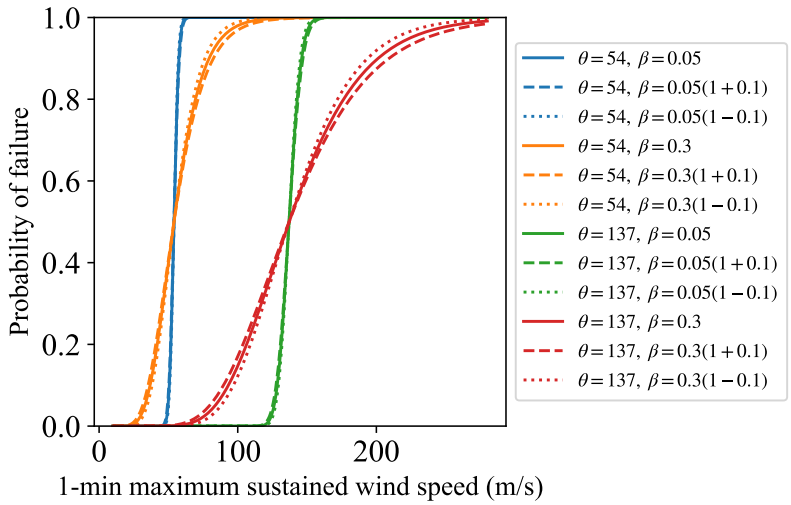

Figure 3.14: Effect of β prediction inaccuracy on fragility curves.

preference or practical considerations. The repository also includes example code demonstrating how to use the metamodels to generate tailored fragility curves. Given a hurricane wind map with intensity and direction information (e.g., from hurricane simulators), to use the parameterized fragility model $P_{f|\boldsymbol{X}^{\text{II}};IM}$, the user only needs to supply the five tuning parameters (Table 3.1) as inputs to the metamodels. The metamodels then return the corresponding θ and β, which define the tailored fragility curve for fragility analysis.

Section 3.3.9.1 provides a detailed discussion on the application and fine-tuning of the parameterized class fragility model. For illustration, the RF metamodel was used for both θ and β, though similar insights are expected with other metamodels. To investigate the relative importance of different parameters on fragilities, sensitivity analysis was performed using both input/output correlation coefficients and the Kucherenko global method. The problem formulation and SA results are summarized in Section 3.3.9.2.

3.3.9.1 Parameterized tower class fragility models

To illustrate the fine-tuning effect, Fig. 3.15 shows six fragility curves based on a 'base case' (138 kV, 90 mph, 1-peak, 600 ft, 0°), with each of the other cases differing from

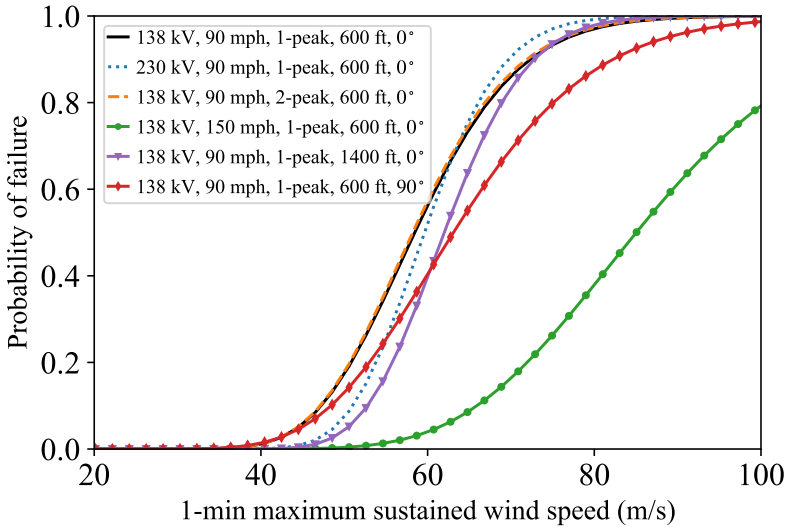

Figure 3.15: Effect of tuning parameter variation on tailoring fragility curves.

the base case by a single tuning parameter. This visual comparison focuses on the effect of each individual parameter in this limited scenario. A more systematic and quantitative assessment of the relative importance of all tuning parameters is presented in the next section using sensitivity analysis. As expected, higher design wind speed shifts the fragility curve to the right, reflecting stronger tower design. At a yaw of 90°, the transmitted cable loads are minimal, also shifting the curve to the right. Larger span length similarly produces a right-shifted fragility curve, though the physical link is less clear. Voltage has a noticeable effect: the 230 kV curve lies mostly to the right at lower wind speeds but crosses the base case curve at higher speeds. In contrast, the number of peaks has little influence, as the 2-peak curve nearly overlaps the base case.

3.3.9.2 Sensitivity analysis results

For sensitivity analysis, the input and output variables need to first be defined. In this study, we considered 29 input variables: 5 Type II parameters (Table 3.1), 23 Type III parameters (Table 3.3), and the *IM* level. The output variable was defined as the per-structure failure fraction (0, 1/3, 2/3, or 1; see Fig. 3.10). This setup resulted in 53800 input–output pairs

for sensitivity analysis. Given the relatively large number of input variables, sensitivity analysis was conducted in two stages, with the second method building on the insights from the first.

First, we computed input/output correlation coefficients, including both linear correlation coefficients (Eq. (3.4)) and Spearman's rank correlation coefficients (Eq. (3.5)), across all 29 input variables. The results are shown in Fig. 3.16, where positive and negative signs indicate the direction of correlation. While Spearman's coefficients are more robust than linear coefficients, the two measures yielded very similar results; the subsequent discussion focuses on the Spearman's coefficients. As expected, the *IM* level exhibits the strongest correlation with the failure fraction, though it is less informative for further discussion. Among the five tuning parameters, design wind speed (X_2^{II}), span length (X_4^{II}), and yaw angle (X_5^{II}) show strong negative correlations with failure fractions, consistent with the illustrative cases in Fig. 3.15. Voltage (X_1^{II}) and number of peaks (X_3^{II}) display weaker correlations, negative and positive respectively. These findings provide practical guidance for data collection when applying the parameterized fragility model: it is more important to obtain high-quality data for design wind speed, span length, and yaw angle, while voltage and number of peaks may be fixed at nominal values if necessary. Notably, the latter two were originally included as tuning parameters based largely on engineering judgment. Moreover, some Type III parameters (unknown and embedded as uncertainty) show stronger correlations with failure fractions than the Type II parameters (known and exposed for fragility model tuning). This should not be surprising, however, as Type III parameters capture inter-structure variability, which is often substantial. Considering all 29 input variables, the top eight influential parameters ranked by Spearman's correlation coefficients are: *IM* (0.739), X_{15}^{III} (0.258), X_2^{II} (0.258), X_{19}^{III} (0.253), X_{11}^{III} (0.238), X_7^{III} (0.226), X_{20}^{III} (0.220), X_{12}^{III} (0.175).

The input/output correlation coefficients are useful for assessing the influence of in-

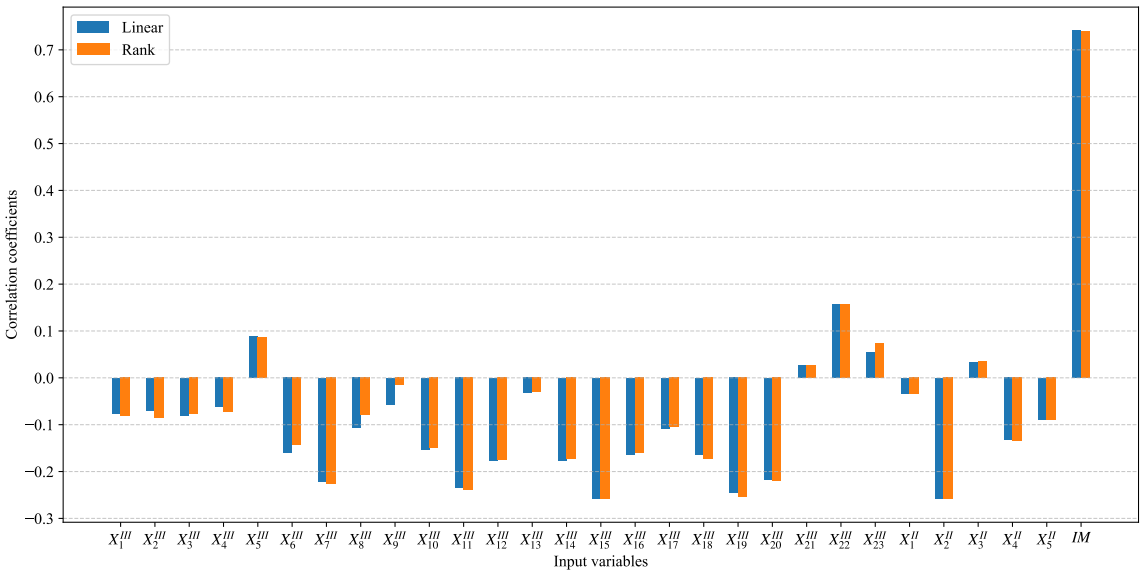

Figure 3.16: Input/output correlation coefficients considering 29 input variables.

dividual inputs on the output but cannot capture interaction effects between inputs. To overcome this limitation, we conducted a global sensitivity analysis using Kucherenko indices. The analysis focused on the top eight input variables given by Spearman's correlation coefficients, with the per-structure failure fraction retained as the output. Fig. 3.17 shows that *IM* remains the most influential variable according to both first-order and total-effect indices. The ranking of the eight input variables largely aligns with the correlation analysis (Fig. 3.16), with only minor shifts, and the relative impacts of the latter seven are comparable. However, the noticeable differences between the first-order and total-effect indices highlight substantial interaction effects among input variables. Accounting for these interactions is important for proper parameter handling, as ignoring them could lead to inappropriate decisions.

3.4 Concluding remarks

This chapter presented the derivation of parameterized fragility models for a representative class of lattice transmission towers under hurricane winds, with a focus on the power trans-

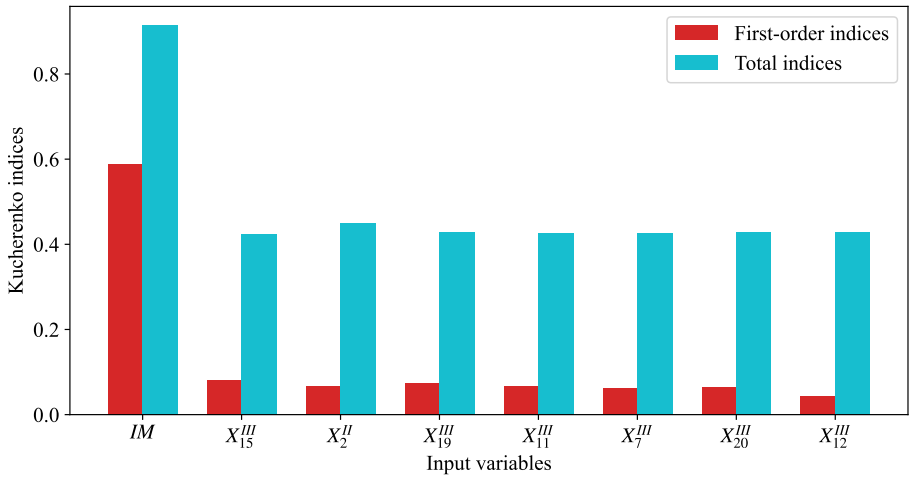

Figure 3.17: Kucherenko indices considering eight input variables.

mission network in Florida. Building on previous studies, we first outlined an eight-step framework for developing parameterized class fragility models, highlighting several original details and recommendations for best practice. We then applied this framework step by step to develop the tower class fragility model using dynamic time history analysis. To our knowledge, this is the first parameterized fragility model developed for this asset class. The resulting model enables more granular fragility assessment at the portfolio or network scale.

We proposed an efficient modeling approach for transmission tower–line systems in a portfolio context, based on two key ideas: (1) treating cables as loads by directly simulating the time histories of forces at the attachment points; (2) treating panels as the basic components using physics-based surrogate analytical models. The class fragility model was parameterized using five easily accessible tuning parameters: voltage, design wind speed, number of peaks (i.e., number of overhead ground wires), span length, and yaw angle. Fragility curves were assumed lognormal, and the two distribution parameters (θ, β) were expressed as functions of the tuning parameters through a regression-based design of experiments that strategically covered the input space. Uncertainty modeling at each design point involved transforming the uncertainty of tower design variables into uncertainty

of surrogate-compatible modeling parameters, using a tower design module to generate synthetic inventory and a conversion step to map raw designs into surrogate model parameters. We introduced novel interpolation functions to reduce the joint distributions of this tower class to 23 uncertainty parameters while explicitly accounting for correlations between component demands and capacities. Additionally, we proposed a dominance-guided uncertainty propagation strategy, which is both more efficient and critical for ensuring adequate propagation of uncertainties. For example, increasing the number of structural samples (the dominant source of uncertainty) was found to be more important than increasing the number of load samples. Different metamodeling methods were used to construct the functional relationships. Sensitivity analyses revealed that design wind speed, span length, and yaw angle are the most influential tuning parameters, whereas voltage and number of peaks have minor effects.

While the refined framework is intended to be generally applicable for developing parameterized fragility models for any hazard and asset type, the application to transmission towers is particularly relevant for similar assets, such as other classes of transmission towers, telecommunication towers, or slender structures. Data availability remains a common challenge in regional or portfolio-scale analyses; Nevertheless, the use of a tower design module to generate synthetic inventory data could ideally be replaced by actual inventory data.

Chapter 4

Using parameterized fragility models for hurricane risk analysis of power transmission networks

4.1 Introduction

Regional risk and resilience analysis has seen significant advancements over the past decades. The focus has expanded from earthquakes to hurricanes and to multi-hazard scenarios, while the scope of analysis has broadened from residential buildings to diverse infrastructure systems. Several dedicated platforms have been developed to support such studies (FEMA, 2021; Zsarnoczay et al., 2025; IN-CORE, 2024; PRAISys, 2025). Within the risk and resilience assessment framework, fragility analysis is a critical step for predicting the damage of physical assets or structures, typically through the use of fragility models (also known as fragility functions or curves) (Melchers and Beck, 2018). At the regional scale—unlike at the single-structure level—analysts often face the challenge of heterogeneous portfolios containing hundreds or thousands of assets that exhibit substantial structure-to-structure variability (Silva et al., 2019). In this context, several approaches to fragility modeling have been adopted, with two major families being archetype fragility models and class fragility models (either parameterized or non-parameterized).

The archetype fragility approach is more widely used, largely due to its similarity to single-structure fragility development and its historical legacy. In this approach, a few representative (or index) structures are selected from the portfolio or class, and a separate fragility model is developed for each following conventional single-structure fragility

procedures, without explicitly accounting for inter-structure uncertainty. In regional applications, each archetype fragility is then assigned to the entire portfolio or to the subset it best represents. While straightforward, this practice provides only a coarse representation of portfolio fragility, capturing heterogeneity at low resolution. The class fragility approach can be further categorized into *parameterized* and *non-parameterized* forms. The non-parameterized class fragility is obtained by first deriving multiple archetype fragilities and then combining them into a single, aggregated fragility model without explicit parameterization. Although seldom used in academia, this approach is more common in the catastrophe modeling industry. The focus here is on the parameterized class fragility. Instead of relying on a few representative structures, this approach explicitly characterizes and propagates inter-structure uncertainty within the heterogeneous portfolio during fragility model development. Such model expresses fragility as a function of a vector of tuning parameters, such as structural characteristics, site conditions, and system configurations (FEMA, 2020; Ghosh et al., 2013; Mohammadi Darestani and Shafieezadeh, 2019). For regional analyses, users can input available parameters to generate tailored fragility curves for individual assets within a heterogeneous portfolio. This parameterization enables flexible modeling that captures heterogeneity more rigorously, providing a finer-grained representation of portfolio fragility.

Despite their clear methodological and practical differences, both archetype and class fragility models are routinely used in practice. However, the implications of adopting different fragility modeling approaches for regional risk and resilience assessments remain poorly understood. Recently, using bridge and transportation networks as case studies, Rincon and Padgett (2024) showed that the level of portfolio resolution achieved by different fragility modeling practices can substantially influence risk outcomes and lead to divergent conclusions. It is unclear whether and how these findings generalize to other infrastructure and hazard types. The electric power transmission system is a critical case

in point: transmission lines carry high-voltage bulk power over long distances and can cause much larger, system-scale disruptions than distribution networks, yet they are vulnerable to hurricane winds and have historically experienced extensive physical damage and outages (NERC, 2018; Florida Public Service Commission, 2018, 2019). Most prior hurricane risk studies of transmission networks have relied on archetype fragility representations for structural components (e.g., towers, conductors), rather than parameterized fragilities (Ma et al., 2021a; Huang and Wang, 2024; Xue et al., 2020). This practice is partly explained by the general shortage of parameterized fragility models for transmission assets. For lattice transmission towers specifically—complex and commonly used supporting structures—many archetype or single-tower fragility models exist (Cai et al., 2019; Dikshit and Alipour, 2023; Fu et al., 2019; Ma et al., 2021a; Macedo et al., 2024; Tian et al., 2020; Mohammadi Darestani et al., 2020). The parameterized fragility model developed in Chapter 3 creates an opportunity to perform a systematic comparison of archetype versus class fragility approaches for transmission networks and answer the open question about how fragility-modeling practices affect regional hurricane risk quantification.

This study evaluates the implications of different fragility analysis practices on hurricane risk quantification outcomes for electric power transmission networks. Section 4.2 presents the methodology for this comparative study within a probabilistic simulation framework, considering three different fragility models: a *parameterized* class fragility model, a *mean* fragility model, and an *archetype* fragility model. The section also introduces a novel once-for-all temporal sampling scheme for using class fragility models, designed to prevent repeated activation of embedded inter-structure uncertainty and thereby avoid risk overestimation. In addition, a blending approach for hurricane wind field simulation is described. Section 4.3 applies the methodology to the Florida (FL) transmission network under two historical hurricanes—Irma (2017) and Michael (2018). The three fragility analysis practices are compared across both events using multiple metrics, including geospatial

and aggregate network-level measures, to systematically assess their implications for risk evaluation of heterogeneous portfolios at regional or network scale. Finally, Section 4.4 summarizes the main findings, and discusses the limitations and broader implications of the work.

4.2 Methodology

4.2.1 Graphical modeling of power transmission network

This study models the power transmission system as a graph using complex network (CN) theory, which provides specialized analytical tools and systematic insights for characterizing the structural properties of complex systems through statistical patterns in their topology (Ma et al., 2021b). A power system can be represented as a connected graph $\mathscr{G}(V,E,W)$, where V is a set of N nodes, E is a set of K edges, and W contains the edge weights. Typically, nodes correspond to buses with generators, substations, and loads, while edges represent transmission lines connecting the nodes. Edge weights can be defined in various ways: the simplest approach assigns all edges a weight of 1, considering only the network topology, whereas more realistic weights—such as line reactance or power flow—capture the electrical properties of transmission lines (Wang et al., 2017b).

Extreme events like hurricanes can damage structural components (e.g., transmission towers). Using CN theory, these damage scenarios can be simulated by removing the affected nodes or edges, thereby reflecting the resulting network state. Details of the failure mechanisms are provided in Section 4.2.4.

4.2.2 Simulation of hurricane wind field

Structural components in transmission networks are sensitive to wind direction, which has been shown to significantly influence their response (Ma et al., 2021a; Mohammadi Darestani et al., 2020). Therefore, hurricane wind fields that include both wind speed and direction are required for fragility analysis. Such wind fields are typically generated using sophisticated hurricane simulators (Xu et al., 2024; Ma et al., 2022). For historical hurricanes, reanalysis datasets such as ERA5 are available (Hersbach et al., 2023); however, they often underestimate peak wind speeds, inadequately capture the inner-core structure of hurricanes, and may have spatial or temporal resolutions that are too coarse for high-resolution risk analysis (Liu et al., 2025). For events with known tracks, such as those in IBTrACS (Knapp et al., 2010; Gahtan et al., 2024), wind field simulation can be efficiently performed using a boundary-layer model (Wang and Wu, 2022). To address the limitations of ERA5 data, parametric correction methods can be applied (Liu et al., 2025). In this study, we use a simplified blending approach to reconstruct hurricane wind fields for historical events. This approach combines the wind field simulated by the parametric Holland model (Holland, 1980) with the ERA5 reanalysis wind field. For a site at distance r from the hurricane center, the blended wind speed (V_b) is given by:

$$V_b = w \cdot V_p + (1 - w) \cdot V_e \tag{4.1}$$

where V_p is the surface wind speed at 10 m above ground, obtained by converting the gradient wind speed from the parametric Holland model; V_e is the ERA5 wind speed at 10 m above ground (interpolation is applied if data are unavailable at a given location). V_p, V_e, and V_b represent 1-min sustained winds in m/s. The weight coefficient w, defined by a

cosine taper, blends V_p and V_e and is given by:

$$w = \begin{cases} 1, & r \leq R_{\text{inner}} \\ 0.5 \cdot \left[1 + \cos\left(\pi \cdot \frac{r - R_{\text{inner}}}{R_{\text{outer}} - R_{\text{inner}}}\right)\right], & R_{\text{inner}} < r < R_{\text{outer}} \\ 0, & r \geq R_{\text{outer}} \end{cases} \tag{4.2}$$

where R_{inner} is the inner radius where blending begins, set equal to the radius of maximum wind ($R_{\max}$); R_{outer} is the outer radius where blending ends, defined as $\max(3 \cdot R_{\max}, 100 \text{ km})$.

The blending assigns the inner core to be dominated by the parametric Holland model and the far field by ERA5, with a smooth transition in between. This approach leverages the strengths of both sources: the parametric model provides a more realistic hurricane core, while ERA5 captures the broader, background wind field. It is worth noting that we use the parametric Holland model for its simplicity and popularity, which meets the objectives of this study. We acknowledge that more advanced, physics-based wind profile models exist (Chavas et al., 2015; Sheng and Bocchini, 2025) and could be employed if available and justified.

4.2.3 Fragility modeling of structural components

A power transmission network includes many types of structural components, such as power plants, substations, and transmission lines. In this study, we focus on overhead transmission lines, specifically the supporting structures that carry the cables, as they are most vulnerable and exposed to hurricane winds. The most common supporting structures are steel poles and lattice towers, each with further variations and classifications (Kalaga and Yenumula, 2017). A schematic of a transmission line and the relevant angles is shown

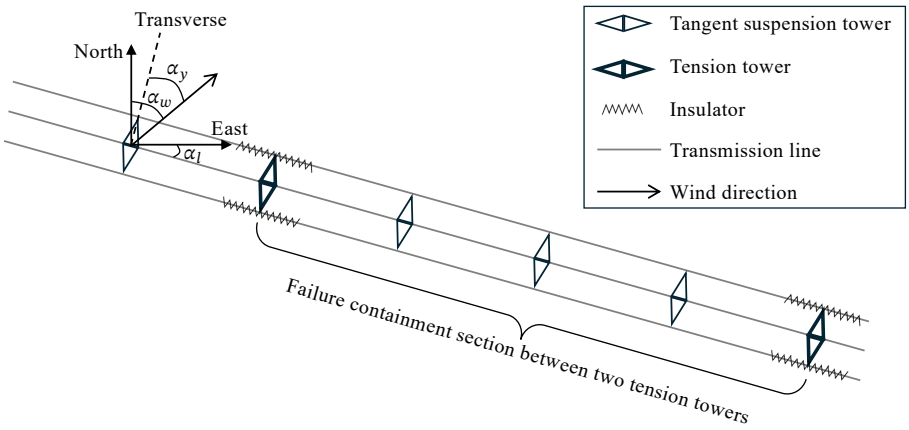

Figure 4.1: Plan-view illustration of the yaw angle (α_y) and tower types along transmission lines (not to scale).

in Figure 4.1. The yaw angle (α_y) is calculated based on the line direction (α_l) and wind direction (α_w) from the simulated wind field: $\alpha_y = \alpha_w - \alpha_l$, with 0° corresponding to the transverse direction and 90° to the longitudinal direction. We consider three fragility models for the supporting structures, representing different regional fragility analysis practices: parameterized fragility, mean fragility, and archetype fragility. All three correspond to one failure limit state: tower collapse.

First, we use the parameterized fragility model developed in Chapter 3, which represents a general class of self-supporting, suspension lattice transmission towers in Florida. The model is expressed as the conditional probability of failure $P_{f|\boldsymbol{X};IM}$, where IM is the intensity measure (1-min maximum sustained wind speed, m/s) and $\boldsymbol{X}$ is a vector of five tuning parameters—voltage (kV), design wind speed (3-sec wind gust, mph), number of peaks (= number of overhead ground wires), span length (ft), and yaw angle (degree). This parameterized fragility model captures the realistic structure-to-structure variability of the heterogeneous transmission line portfolio (e.g., design wind speeds ranging from 90 to 150 mph, span lengths from 400 to 1400 ft) by explicitly characterizing and propagating inter-structure uncertainty. It represents the state-of-the-art fragility for transmission towers and is publicly available (Wang and Bocchini, 2025a). For regional or network-

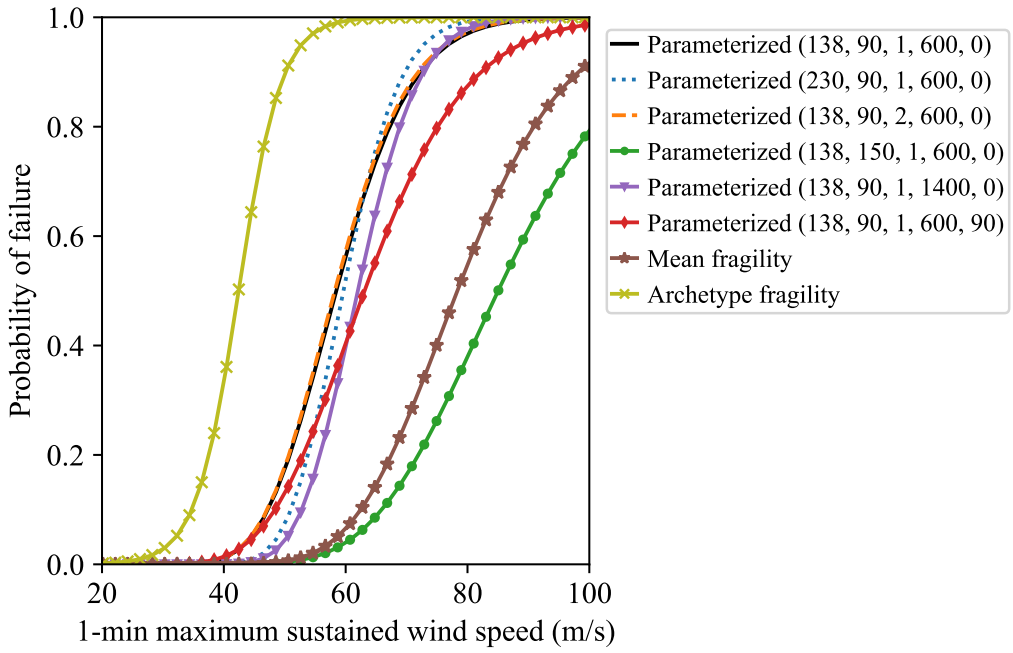

Figure 4.2: Fragility curves used in this study. Shown are examples of parameterized fragility curves, along with the mean fragility curve and the archetype fragility curve. The parameterized fragility curves are adapted from Chapter 3, with tuning parameters listed in parentheses: voltage (kV), design wind speed (3-sec wind gust, mph), number of peaks, span length (ft), and yaw angle (degrees). For comparison, the original intensity measure of the archetype fragility curve has been converted to 1-min maximum sustained wind speed (m/s).

scale analysis, the analyst provides the known tuning parameters for each tower to obtain a fine-tuned fragility curve $P_{f|\boldsymbol{X}=\boldsymbol{x};IM}$ which reflects the remaining unknown uncertainty. By conditional on both the structural features and the intensity measure, this model delivers a high-resolution, granular representation of fragility for heterogeneous portfolios. Figure 4.2 illustrates example parameterized fragility curves and the effect of tuning. The most influential parameters are design wind speed, span length, and yaw angle, whereas voltage and number of peaks have small impact. In this study, we apply this parameterized fragility model to all supporting structures in the Florida transmission network—including poles and lattice towers—except for failure-containment tension structures, which are assumed not to fail (see Section 4.2.4). For this application, we assume all supporting structures belong to the same class considered in Chapter 3.

The second fragility model, referred to as the mean fragility, is constructed by fixing the five tuning parameters at their nominal values: $\overline{\boldsymbol{X}}$ = (138 kV, 120 mph, 2-peak, 900 ft, 45 degrees). The resulting fragility curve, denoted as $P_{f|\boldsymbol{X}=\overline{\boldsymbol{X}};IM}$, is shown in Figure 4.2. This model reflects a popular practice in fragility analysis—using a mean fragility curve in the expectation of obtaining mean results. The underlying assumption is that under- and over-estimations will balance out when results are aggregated across the portfolio. However, the validity and implications of this assumption for power transmission networks remain unclear. Note that this is a single, fixed fragility curve conditional only on the intensity measure, despite being expressed with parameter notation. For regional or network-scale analyses, the same mean fragility curve is assigned to all supporting structures it represents, regardless of inter-structure variability. Consequently, differences in predicted damage are driven solely by variations in the intensity measure, not by structural characteristics. In this study, the mean fragility model is applied to all supporting structures in the Florida transmission network—including poles and lattice towers—except for tension structures, which are assumed not to fail.

The third fragility model is the archetype fragility, denoted $P_{f|IM}$, which represents a very common practice in fragility analysis. The model used in this study is adapted from that available on the IN-CORE platform (IN-CORE, 2024). As shown in Figure 4.2, the archetype fragility curve is weaker than both the example parameterized and mean fragility curves. The original model uses a 3-sec wind gust as the intensity measure, which is converted here to 1-min max sustained wind speed (MSWS) for consistency and comparison. The archetype fragility corresponds to a single representative transmission tower assumed to typify an entire portfolio (or a subset thereof), without explicitly accounting for structure-to-structure uncertainty. Similar to the mean fragility, it is a single curve conditional only on the intensity measure, providing a coarse representation of portfolio fragility. Accordingly, analysts typically assign this same curve to all assets it best represents, disregarding

inter-structure variability. In this study, the archetype fragility is likewise applied uniformly to all supporting structures in the Florida transmission network (including poles and lattice towers), assuming that the archetype tower is representative of the entire transmission line portfolio.

Since all three fragility models were originally developed for lattice towers but are applied here to both towers and poles, we use the term 'tower' broadly to refer to all supporting structures, unless otherwise specified.

4.2.4 Failure mechanism of tower-line system

Transmission lines extend over long distances, and from the standpoint of longitudinal strength, the supporting structures can be broadly categorized as suspension and tension towers (Figure 4.1). Suspension towers are not designed to resist longitudinal loads; instead, they rely on the free swing of insulators to balance small longitudinal forces. Because of their weak longitudinal capacity, the failure of a suspension tower can trigger a cascading failure along the line, similar to a domino effect (Dikshit et al., 2024). To limit the extent of such cascades, tension towers—also known as failure-containment or anchor towers—are installed periodically along the line. These structures are designed to resist longitudinal loads and are therefore stronger (shown in bold in Figure 4.1). The spacing between tension structures typically ranges from 2 to 10 miles ($3.2 - 16.1$ km) (Wong and Miller, 2010). Cascading failures can propagate until they stop naturally or are arrested by a tension tower, effectively confining the failure within a failure-containment section. The fragility models defined in Section 4.2.3 are applied to suspension towers, which constitute $80\% - 90\%$ of transmission structures (Fang et al., 1997). In this study, tension towers are assumed not to fail and are considered to always arrest a cascade once reached. The spacing between two tension towers is assumed to be 10 km for all transmission lines. Thus, lines shorter than 10 km contain no intermediate tension towers (i.e., a single failure-containment

section bounded by two nodes), whereas longer lines include at least one tension tower dividing them into multiple containment sections.

Two extreme scenarios are considered to represent the cascading failure mechanism: (1) Without cascading—failure of a suspension tower does not trigger adjacent failures; (2) With cascading—failure of a suspension tower triggers the failure of all other suspension towers within the same containment section. The reality falls between these two extremes and is closer to the 'without cascading' case. Nonetheless, analyzing both scenarios provides upper and lower bounds on the potential number of failed towers. In summary, the total number of failed towers equals the number of initially failed towers in the no-cascade case, or the number of final failed towers after propagation in the with-cascade case. A transmission line (edge) is considered failed (inactive) if any of its supporting structures fail; failed edges are then removed from the original network to yield a damaged graph representing the post-event system state.

4.2.5 Probabilistic simulation of structural components failure within the network

With the fragility models defined for structural components, hurricane risk analysis of transmission networks is performed within a probabilistic simulation framework, typically using Monte Carlo simulation (Ma et al., 2022; Ouyang and Duenas-Osorio, 2014). This study adopts a similar approach, with two key methodological aspects highlighted in this section. Section 4.2.5.1 introduces a novel *once-for-all* temporal sampling strategy to correctly apply class fragility models and avoid bias from unintended inter-structure uncertainty. Section 4.2.5.2 describes the incorporation of spatial correlation through random fields, followed by a summary of the overall probabilistic framework.

4.2.5.1 Once-for-all temporal sampling strategy

Unlike earthquake events, which typically last only seconds, hurricanes are long-duration, evolving events, spanning hours to weeks. As a result, hurricane risk analysis often involves temporal sampling—evaluating the hazard at multiple time steps with a specified interval. Common intervals reported in the literature include 10 minutes (Xu et al., 2024), 1 hour (Ma et al., 2022), and 4 hours (Liu and Singh, 2010). However, when using class fragility models, repeated temporal sampling can introduce a bias toward overestimation. This occurs because inter-structure uncertainty is explicitly embedded in class fragility curves. Each temporal sample effectively represents a 'different' structure. In reality, a tower remains unchanged throughout the hurricane, so multiple samples at different time steps artificially simulate multiple structures. Since a tower fails if it exceeds its limit at any time step, even a single 'weak' sample triggers failure, leading to systematic overestimation of tower failure probabilities and risk. This overestimation is further amplified by the fact that a transmission line behaves as a series system: the failure of any single tower results in the failure of the entire line, even without considering cascading failures. This challenge can be broadly described as decoupling different sources of uncertainty. To decouple structural and load uncertainties, Ma et al. (2022) proposed the *fragility pool* technique: a pre-generated pool of archetype fragilities (assuming fully known archetypes, without structural uncertainty) is created, and for each simulation, fragility models are sampled from the pool and assigned to structures at the start. Because the assigned archetype structures remain deterministic throughout the event, multiple temporal sampling can be taken without overestimating risk. While theoretically rigorous, this approach is rarely practical. Generating a comprehensive pool of archetype fragilities demands substantial computational resources and, more importantly, assumes full knowledge of each structure—a requirement that is often infeasible due to limited data availability.

In this study, we propose a practical once-for-all temporal sampling strategy to correctly use class fragility models without evoking the embedded structure-to-structure uncertainty, thereby avoiding risk overestimation. The approach proceeds in two steps. First, for each tower j in the transmission network $\mathscr{G}$, we evaluate the tower failure probabilities at all time steps based on the fine-tuned fragility curves and record the maximum failure probability throughout the event, $P_{j,\max}^{\text{tower}}$. A 1-hour time interval is used, consistent with the wind load duration used in the development of the parameterized fragility model. Second, a single sample is drawn for the entire event, and the sampled value is compared with $P_{j,\max}^{\text{tower}}$ to determine tower failure. By sampling only once, we avoid effectively 'resampling' different structures at each time step, thereby preventing overestimation of risk. This approach reflects the fact that a tower fails if it exceeds its limit at any time step, analogous to a temporal series system. The first step is illustrated in Algorithm 4.1, and the second step is detailed in Section 4.2.5.2. For a tower j, the failure probability varies across time steps $t_i \in \mathscr{T}$ due to two factors: the time-varying yaw angle $\alpha_{y,j}(t_i)$, which fine-tunes the fragility curve at each step, and the time-varying wind speed $IM_j(t_i)$. For consistency and comparison, the same strategy is applied to the mean and archetype fragility models, although the archetype model does not involve inter-structure uncertainty. It is worth noting that our proposed approach is conceptually related to the idea of synchronous sampling, where a single random realization is maintained across models or scales to enable consistent and fair comparison. In our case, the once-for-all sampling strategy plays an analogous role by 'synchronizing' the structural realization across all times steps within an event simulation.

4.2.5.2 Modeling spatial correlation using random fields

Another important aspect of regional risk analysis is the spatial correlation of damage among structural components. This correlation arises from two main sources: (1) structural similarity, as nearby structures often share similar design, vintage, and deterioration char-

Algorithm 4.1 Computation of maximum tower failure probabilities during a hurricane event.

Require: ERA5 data, hurricane track data, transmission network $\mathscr{G}$, simulation time period $\mathscr{T}$, fragility model choice (*parameterized* or *mean* or *archetype*)

for each time step $t_i \in \mathscr{T}$ **do**
  Initialize wind field simulation using the blending approach
  for each tower $j \in \mathscr{G}$ **do**
    Compute wind speed $IM_j(t_i)$ and wind direction $\alpha_{w,j}(t_i)$
    if *parameterized* fragility **then**
      Set tuning parameters, including the yaw angle $\alpha_{y,j}(t_i)$
      Predict lognormal parameters $\theta_j(t_i)$ and $\beta_j(t_i)$ by metamodels
      Compute probability of failure $P_j^{\text{tower}}(t_i)$ using the finetuned fragility curve, with known $IM_j(t_i)$
    else if *mean* fragility **then**
      Compute probability of failure $P_j^{\text{tower}}(t_i)$ using the *mean* fragility curve, with known $IM_j(t_i)$
    else
      Compute probability of failure $P_j^{\text{tower}}(t_i)$ using the *archetype* fragility curve, with known $IM_j(t_i)$
    Update $P_{j,\max}^{\text{tower}} = \max(P_{j,\max}^{\text{tower}}, P_j^{\text{tower}}(t_i))$
return $[P_{j,\max}^{\text{tower}}]$, for $j \in \mathscr{G}$

acteristics, and (2) hazard correlation, since structures in close proximity experience similar hazard conditions. The importance of considering such correlations has been demonstrated in regional seismic risk studies (Heresi and Miranda, 2022; Sousa et al., 2018; Bocchini et al., 2011), and for hurricane risk in power systems, Ma et al. (2022) incorporated spatial correlation using a random field approach. Although calibrating spatial correlation models is very challenging due to system complexity and limited data, including even a crude correlation is preferable to ignoring it. Moreover, spatial correlation typically has a secondary effect on damage predictions; the primary influence comes from the fragility-based failure probabilities, which capture the dominant factors affecting asset failure.

In this study, we adopt the random field technique to model spatial correlation (Ma et al., 2022; Bocchini et al., 2011). For each simulation sample s, the external stressors on transmission network components are simulated as a two-dimensional, non-Gaussian ran-

dom field D_s with uniform marginal distribution in $[0,1]$. A covariance matrix is required to generate the field, with a correlation distance λ set to 10 km, based on the spacing between tension towers. We recognize that a comprehensive calibration of λ would require extensive data and simulations, which is beyond the scope of this work. To generate D_s, the study region is discretized into a regular grid, and the field value at tower j, denoted $d_{j,s}$, is obtained via interpolation. Initial failures of suspension towers (without cascading) are determined by comparing $d_{j,s}$ with the maximum tower failure probability $P^{\text{tower}}_{j,\max}$. Algorithm 4.2 summarizes the probabilistic simulation framework for structural component failures. For each simulation, a single spatially correlated random field is generated for the entire hurricane event, as per the once-for-all temporal sampling strategy. Monte Carlo simulations continue until the edge failure probabilities $[P^{\text{edge}}_{k,s}]$ converge at sample size N_s, following the convergence criterion in Ma et al. (2022).

Algorithm 4.2 Probabilistic risk assessment of transmission network under hurricanes.

Require: maximum tower failure probabilities $[P^{\text{tower}}_{j,\max}]$, transmission network $\mathscr{G}$, correlation length λ, number of simulations N_s

for $s = 1$ **to** N_s **do**
  Generate a random field $\mathscr{D}_s$ with given λ
  for each edge $k \in \mathscr{G}$ **do**
    Compute field value $d_{j,s}$ for each tower $j \in$ edge k by interpolation
    Determine initial failures of suspension towers (without cascading): failure if $d_{j,s} \leq P^{\text{tower}}_{j,\max}$; count as $n^{\text{initial}}_{k,s}$
    Determine cascaded failures of suspension towers; count as $n^{\text{cascade}}_{k,s}$
    Determine edge state: failure if $n^{\text{initial}}_{k,s} > 0$, survival otherwise
    Update edge probability of failure $P^{\text{edge}}_{k,s}$
  Obtain damaged network $\mathscr{G}^{\text{damage}}_s$ by removing failed edges from $\mathscr{G}$
  Compute network performance metrics for $\mathscr{G}^{\text{damage}}_s$
return $[P^{\text{edge}}_{k,s}]$, $[n^{\text{initial}}_{k,s}]$, $[n^{\text{cascade}}_{k,s}]$, and [Network metrics], for $k \in \mathscr{G}$ and $s = 1, \ldots, N_s$

4.2.6 Network performance metrics

Using complex network theory, various metrics (topological, spectral) can quantify power network performance (Ma et al., 2021b). This study focuses on three simple and effective network-level metrics: the number of failed towers, the largest connected component (LCC) ratio, and the global efficiency ratio. Descriptions of each metric are provided below.

The number of failed towers provides a direct and intuitive measure of network damage. It is computed for two extreme cases: without and with cascading. As shown in Algorithm 4.2, the total number of failed towers is obtained by summing the initial failures and, for the cascading case, the additional failures triggered along the lines. These are denoted as N^{initial} and N^{cascade}, respectively. In the pre-event, undamaged state, the entire network forms a single connected component. (Here, a 'component' refers to a set of connected nodes, not structural components like towers.) The LCC ratio quantifies network connectivity after damage and is defined as LCC ratio $= N_{\text{LCC}}/N$, where N_{LCC} is the number of nodes in the largest connected component. A smaller LCC ratio indicates greater fragmentation and more severe network damage. Finally, global efficiency measures how efficiently nodes can communicate and has been used as a network performance metric (Rincon and Padgett, 2024). To facilitate interpretation relative to the undamaged state, we define the global efficiency ratio, $\eta_r = \eta_d/\eta_u$, where η_d and η_u are the global efficiencies of the damaged and undamaged networks, respectively. Smaller η_r values indicate more severe damage and greater loss of network performance.

4.3 Demonstration on the Florida power transmission network under historical hurricanes

In this section, the proposed methodology is demonstrated using the Florida transmission network under historical hurricane events. Florida is selected as the case study due to its high hurricane exposure and history of severe storm impacts. Section 4.3.1 describes the graph model of the FL transmission network. Section 4.3.2 presents the simulated hurricane wind fields for two representative events—Irma (2017) and Michael (2018). Section 4.3.3 compares the results obtained from different fragility modeling practices and discusses their implications.

4.3.1 Florida transmission network modeling

To model the FL transmission network, we use publicly available GIS data and manually collected sources (Homeland Infrastructure Foundation-Level Data (HIFLD), 2022; Homeland Infrastructure Foundation-Level Data (HIFLD), 2023). Missing information is imputed as needed while preserving available data integrity. Detailed node and edge attributes are omitted here and can be found in the cited sources. Below, we describe the data collection for the five tuning parameters required by the parameterized class fragility model.

Edge voltages are directly obtained from GIS data (Homeland Infrastructure Foundation-Level Data (HIFLD), 2022), with all towers along the same line sharing the same voltage. Design wind speeds are derived from publicly available raster data (American Society of Civil Engineers (ASCE), 2023); for each line, the design wind speed at the line midpoint is assigned to all towers along that line, consistent with usual design practice. Span lengths for 500 kV and 230 kV lines are taken from manually collected data (see

Chapter 3), while those for other voltages are sampled from a discrete uniform distribution $[400, 500, \ldots, 1400]$ ft, a typical range of span lengths. All towers along a line share the same span length. The number of peaks (1 or 2) is not easily available or will take a lot of efforts to collect. Given that it has negligible influence on fragility fine-tuning, it is randomly assigned from a discrete uniform distribution $[1, 2]$ and kept constant within each line. Finally, the yaw angle for each tower (recall Figure 4.1) is computed from the simulated wind direction and the line orientation from GIS data (Homeland Infrastructure Foundation-Level Data (HIFLD), 2022). Among the five tuning parameters, only the yaw angle varies with time and across towers, while the other four remain static and identical within each line.

As shown in Figure 4.3, the FL transmission network is modeled as an undirected graph consisting of 2404 nodes and 3013 transmission lines (edges) (Hagberg et al., 2008). The lines are color-coded by voltage level: 69 kV, 115 kV, 138 kV, 230 kV, and 500 kV. Figure 4.4 shows the distribution of the number of towers per transmission line, excluding very short lines that contain no towers. Overall, the network comprises 90419 towers (i.e., all supporting structures, including poles and lattice towers).

4.3.2 Wind fields of historical hurricanes Irma (2017) and Michael (2018)

Two historical hurricanes—Irma (2017) and Michael (2018)—are selected because they followed distinct tracks and affected different regions of Florida. Irma struck the state twice, first as a Category 4 at Cudjoe Key and then as a Category 3 on Marco Island, producing strong winds across nearly the entire state except the western Panhandle (Wikipedia contributors, 2025a). In contrast, Hurricane Michael was the first recorded Category 5 hurricane to make landfall in the Florida Panhandle (Wikipedia contributors, 2025b). Studying

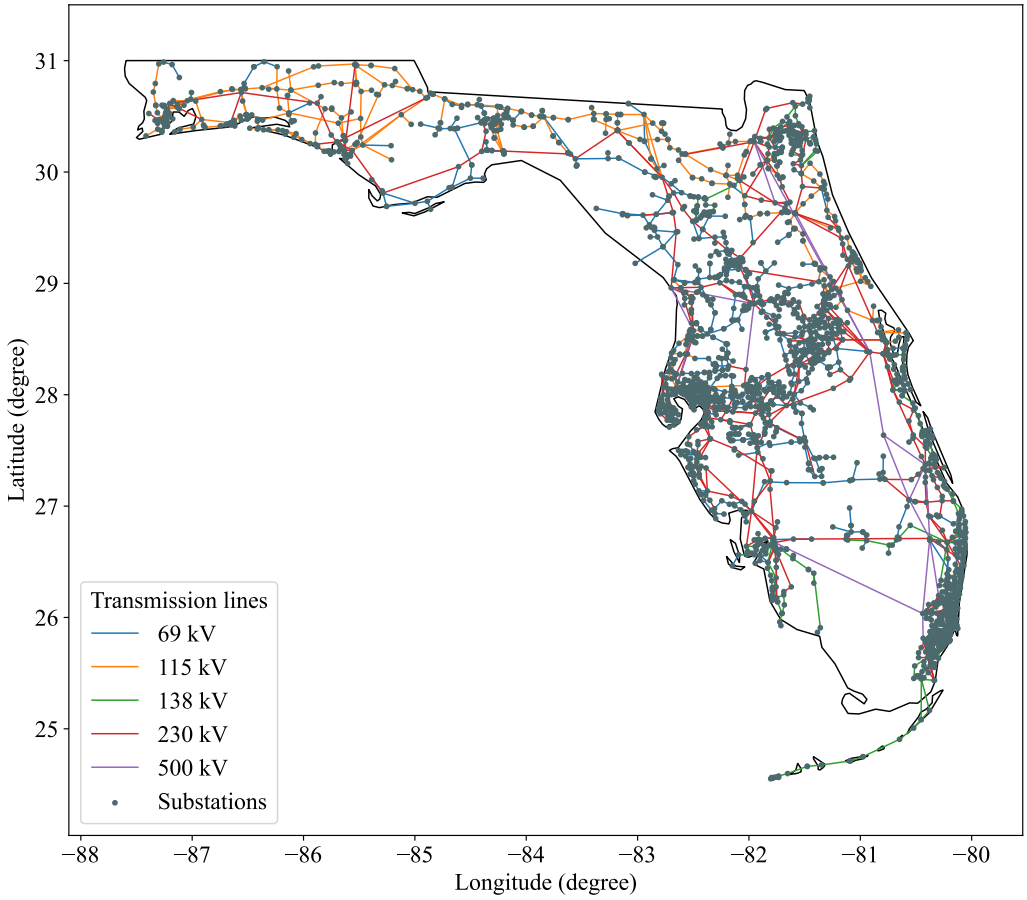

Figure 4.3: Graph model of the Florida transmission network, where nodes represent substations and edges represent transmission lines.

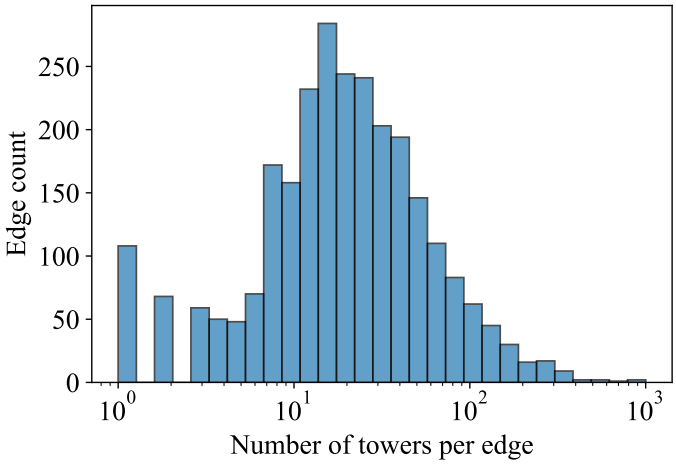

Figure 4.4: Histogram showing the distribution of the number of towers per transmission line (edge).

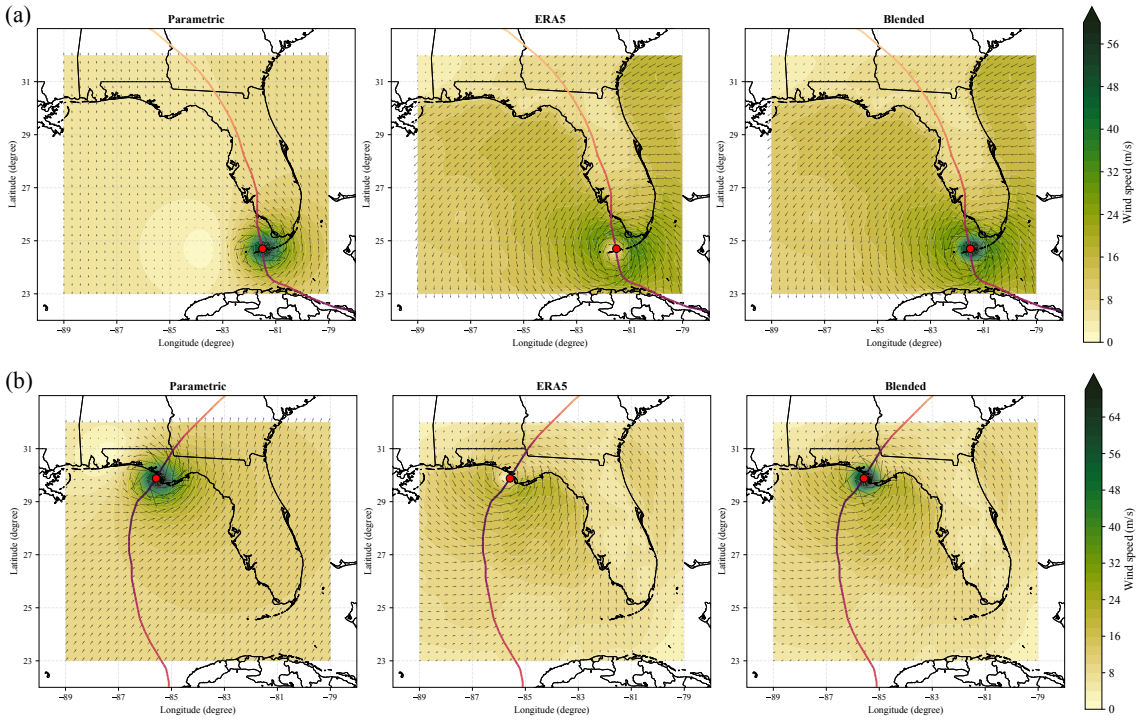

Figure 4.5: (a) Wind field for Hurricane Irma on 2017-09-10 at 13:00 UTC; (b) Wind field for Hurricane Michael on 2018-10-10 at 17:00 UTC.

these two events allows assessing the implications of different fragility modeling practices under varied scenarios, yielding more robust and generalizable conclusions. Using the blending approach described in Section 4.2.2, wind fields over Florida are simulated at 1-hour intervals for each hurricane event. Figure 4.5 shows the wind fields at selected time steps for Irma and Michael, along with the hurricane track and center. Wind speeds are expressed as 1-min MSWS (m/s). ERA5 wind fields underestimate peak winds and poorly capture the inner-core structure, whereas the blended fields effectively address these issues by integrating the parametric and ERA5 wind fields. The simulated wind fields and source data (tracks, ERA5) are publicly available (Wang and Bocchini, 2025c).

4.3.3 Results and discussion

Geospatial results are presented before aggregated metrics to preserve spatial information and provide context for interpreting network-level outcomes. Section 4.3.3.1 shows transmission line (edge) failure probabilities and maximum tower failure probabilities, offering both a network-wide overview and detailed edge- and tower-level insights. Section 4.3.3.2 presents the three aggregated network performance metrics. In both sections, the three fragility models are compared across the two hurricanes and across metrics. This comprehensive comparison allows for a thorough assessment of model behavior, ensuring that observed differences reflect inherent characteristics of the fragility models rather than random variations between events.

4.3.3.1 Geospatial results

The Monte Carlo simulation follows the procedure described in Section 4.2.5 (see Algorithms 4.1 and 4.2). Using the three fragility models for each hurricane, six simulation cases are analyzed in total. For each case, 500 samples ($N_s = 500$) are sufficient to ensure convergence of edge failure probabilities. Figure 4.6 shows the convergence plots for all six cases, along with box plots summarizing the edge failure probabilities at convergence. For Hurricane Irma, 65, 40, and 2072 edges fail at least once ($P^{\text{edge}} \geq 1/500 = 0.002$) under the parameterized, mean, and archetype fragility models, respectively. For Hurricane Michael, the corresponding numbers are 94, 86, and 336. The archetype fragility model markedly overestimates damage compared with the parameterized and mean fragility models, as evident in the geospatial maps (Figure 4.7(c) and (f)), where even edges far from the hurricane tracks experience failures.

The final convergent edge failure probabilities are shown in the boxplots of Figure 4.6 and summarized in Table 4.1. For Irma, the parameterized and mean fragility models yield

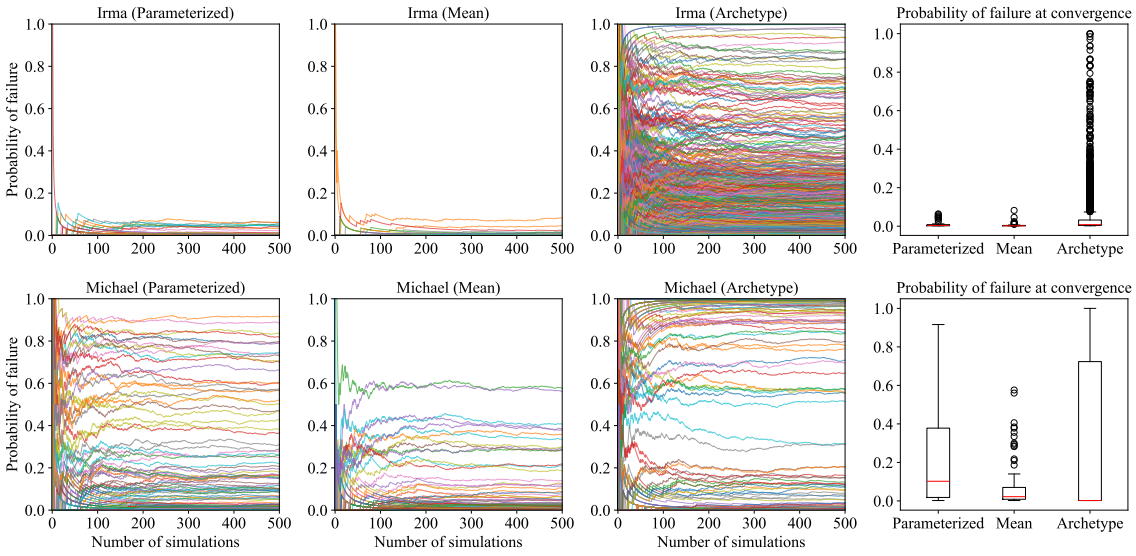

Figure 4.6: Convergence plots for all six simulation cases, with accompanying box plots summarizing the probability of transmission line failure at convergence for each case. Note: plots show only lines that failed at least once in each respective simulation.

similarly low central values (median and mean) and narrow distributions (small range and standard deviation), indicating generally low predicted damage. In contrast, the archetype model produces much higher mean and median values, systematically overestimating failure probabilities—an expected outcome given that the selected archetype represents a relatively weak structure (Figure 4.2). Its results also exhibit a much wider spread (standard deviation about 10 times larger) and an extreme maximum of 1, indicating unrealistically high or near-total failure probabilities in some cases. All models show right-skewed distributions (mean $>$ median), but the archetype model displays the strongest skew, with a large gap between mean (0.058) and median (0.008), implying that a few extreme overpredictions drive up the average. Overall, for Irma, the parameterized and mean fragility models behave similarly, while using a single archetype fragility model introduces systematic bias, overestimating risk and producing extreme outliers.

For Michael, the parameterized fragility model yields the highest median and the second-highest mean edge failure probabilities, indicating overall greater central tendencies than the other two models. The archetype model exhibits a strongly right-skewed distribution—

Table 4.1: Summary statistics of transmission line failure probabilities at convergence.

Hurricane	Model	Mean	Median	Max.	Min.	Standard deviation
Irma	Parameterized	0.010	0.004	0.064	0.002	0.015
	Mean	0.007	0.002	0.082	0.002	0.014
	Archetype	0.058	0.008	1.000	0.002	0.135
Michael	Parameterized	0.233	0.102	0.916	0.002	0.272
	Mean	0.079	0.022	0.576	0.002	0.127
	Archetype	0.268	0.002	1.000	0.002	0.416

Note: The reported statistics refer to lines that failed at least once during the simulation.

mostly low probabilities with a few extreme outliers that inflate the mean. In terms of variability, the archetype model remains inconsistent and occasionally extreme, while the parameterized model preserves more variability than the mean model—likely reflecting more realistic spatial heterogeneity in vulnerability, as further illustrated in the geospatial maps below. All models are right-skewed, but the archetype model exhibits the strongest skew (mean = 0.268 vs. median = 0.002), indicating predominantly low probabilities with occasional extreme values.

Comparing across the two hurricanes shows event-level trends: The mean edge failure probabilities from the parameterized, mean, and archetype fragility models for Michael are approximately 23, 11, and 5 times those for Irma, respectively. All models show substantially higher predicted damage for Michael, consistent with its greater intensity and inland penetration. The parameterized model scales most strongly (mean increases from 0.010 to 0.233), suggesting that it captures hazard intensity and structural vulnerability changes effectively. The mean fragility model increases more moderately (mean increases from 0.007 to 0.079), possibly under-responsive to event severity due to its coarse fragility definition. The archetype fragility model shows a less proportional rise (mean increases from 0.058 to 0.268), reflecting saturation effects from already inflated values. There is also consistency across both events: the parameterized fragility model yields the most balanced and stable predictions, the mean fragility model systematically underpredicts relative to parameterized model, and the single archetype fragility model produces highly variable results with

occasional unrealistic extremes. These consistent patterns across hurricanes indicate that the observed differences reflect model characteristics rather than random event effects.

Figure 4.7 shows geospatial maps of transmission line failure probabilities for six simulation cases. Zoomed-in insets display maximum tower failure probabilities (as points) along each line in the bounding box. For Irma, comparing the three fragility models (Figure 4.7 (a)-(c)), the archetype fragility substantially overestimates the number and extent of failed edges. In contrast, the parameterized and mean fragility models localize damage more realistically to areas of strong winds near the hurricane track. Notably, the parameterized model also predicts failures in central Florida beyond the main wind field near landfall, reflecting its ability to capture structural heterogeneity and wind direction effects. The mean fragility model, conditional only on wind intensity, provides a coarser, lower-resolution damage prediction that cannot resolve these finer patterns. Focusing on the zoom-in of maximum tower failure probabilities in Figure 4.7(a)-(c), the parameterized and mean fragility models show similar ranges, but their spatial patterns differ. In Figure 4.7(a), the maximum tower failure probabilities exhibit scattered, non-continuous variations along lines, reflecting high-resolution fragility definition due to spatial heterogeneity captured by the five tuning parameters. In contrast, the mean fragility model (Figure 4.7(b)), being a single curve conditional only on wind speed, produces smooth, continuous patterns following the wind field. For the same reason, the archetype fragility (Figure 4.7(c)) also yields smooth, continuous patterns, but with maximum tower failure probabilities reaching 1. This tower-level overestimation drives extreme edge failure probabilities, since an edge fails if any tower within it fails.

For Michael, the geospatial maps in Figure 4.7(d)-(f) show similar patterns as observed for Irma. The archetype fragility substantially overestimates the scope and number of failed edges, whereas the parameterized and mean models localize damage to areas near strong winds along the track. Focusing on the zoomed-in bounding box of maximum tower failure

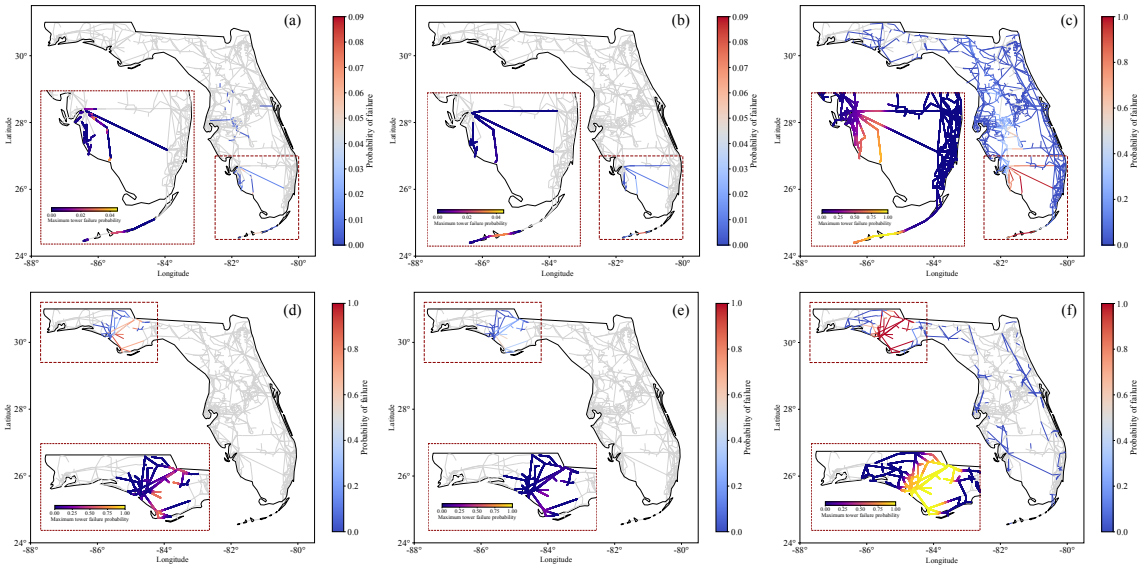

Figure 4.7: Geospatial maps of transmission line failure probability for six simulation cases: (a)–(c) Irma with parameterized, mean, and archetype fragilities; (d)–(f) Michael with parameterized, mean, and archetype fragilities. Zoom-in maps in the bounding box show the maximum tower failure probability (as points) along each line. Lines that never failed are grey; lines that failed at least once are shown in color. For easier comparison, Michael cases (d)–(f) share the same color scale, even though their maximum values differ slightly. For Irma, subplot (c) uses a different scale than (a) and (b) due to its higher maximum values.

probabilities, the parameterized and mean fragility models differ both in spatial pattern and range, with maximum tower failure probabilities reaching about 0.73 and 0.26, respectively. As with Irma, the parameterized fragility model captures fine-grained variations reflecting spatial heterogeneity, while the mean and archetype models produce coarser, speed-driven predictions that ignore structural variability and wind direction effect.

Comparing the two events, we observe clear event-level trends. Maximum tower failure probabilities increase substantially for Michael across all three fragility models, consistent with the corresponding rise in edge failure probabilities, since edge failure is driven by tower-level failures. However, the scaling of maximum tower failure probabilities differs across the three fragility models—largest for the parameterized model, moderate for the mean model, and smallest for the archetype model—mirroring the patterns observed in edge failure probabilities for the same reasons. Across both hurricanes, the parameter-

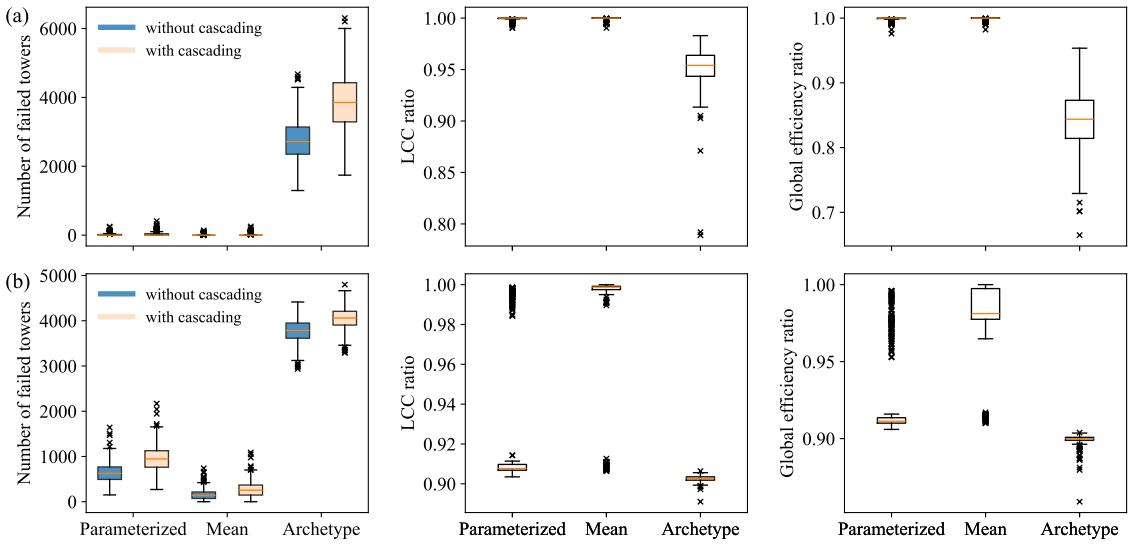

Figure 4.8: Comparison of network performance metrics from using different fragility models: (a) Irma; (b) Michael.

ized and mean models yield realistic geospatial damage scope. The parameterized model further offers finer spatial resolution by capturing structural heterogeneity and wind direction effects through its tuning parameters, whereas the mean model tends to underpredict (relative to the parameterized model) and lacks this granularity. The archetype model, in addition to producing unrealistic extreme maxima, systematically overestimates damage extent and fails to resolve spatial heterogeneity. Overall, the consistent relative behavior of the three models across both events reinforces that these differences stem from inherent model characteristics rather than random event variability.

4.3.3.2 Aggregate network performance results

Results of the three aggregate metrics introduced in Section 4.2.6 are discussed here. Figure 4.8(a) and (b) compare network performance metrics across fragility models for Irma and Michael, respectively, with key statistics summarized in Table 4.2.

The number of failed towers is examined first. As expected, failures considering cascading effects (N^{cascade}) exceed those without cascading (N^{initial}). Recall that these two

Table 4.2: Summary statistics of network performance metrics.

Hurricane	Model	Metric	Mean	Median	Max.	Min.	Standard deviation
Irma	Parameterized	N^{initial}	14	0	248	0	28
	Parameterized	N^{cascade}	28	0	408	0	51
	Mean	N^{initial}	5	0	140	0	14
	Mean	N^{cascade}	10	0	253	0	28
	Archetype	N^{initial}	2769	2713	4674	1296	621
	Archetype	N^{cascade}	3894	3853	6304	1742	780
	Parameterized	LCC ratio	0.99933	1.0	1.0	0.99043	0.00153
	Mean	LCC ratio	0.99935	1.0	1.0	0.99043	0.00164
	Archetype	LCC ratio	0.95247	0.95403	0.98295	0.78910	0.01772
	Parameterized	η_r	0.99878	1.0	1.0	0.97594	0.00249
	Mean	η_r	0.99923	1.0	1.0	0.98216	0.00196
	Archetype	η_r	0.84241	0.84375	0.95348	0.66476	0.04374
Michael	Parameterized	N^{initial}	642	625	1641	150	209
	Parameterized	N^{cascade}	959	945	2169	270	271
	Mean	N^{initial}	154	140	738	0	110
	Mean	N^{cascade}	269	255	1087	0	171
	Archetype	N^{initial}	3770	3786	4414	2935	254
	Archetype	N^{cascade}	4050	4061	4798	3289	236
	Parameterized	LCC ratio	0.92563	0.90765	0.99875	0.90349	0.03543
	Mean	LCC ratio	0.98813	0.99875	1.0	0.90641	0.02872
	Archetype	LCC ratio	0.90255	0.90266	0.90641	0.89101	0.00127
	Parameterized	η_r	0.92459	0.91131	0.99610	0.90597	0.02746
	Mean	η_r	0.97780	0.98119	1.0	0.90999	0.02532
	Archetype	η_r	0.89949	0.89995	0.90387	0.85901	0.00302

represent upper and lower bounds, with reality typically closer to the non-cascading case; hence, N^{initial} serves as the more realistic reference. According to available post-event data, three utility companies reported 23 damaged transmission structures (excluding known wood transmission poles) from Hurricane Irma (Florida Public Service Commission, 2018). Comparing this to the central values of N^{initial}, the parameterized fragility model yields the closest estimates (mean = 14, median = 0), while the mean fragility model somewhat underpredicts (mean = 5, median = 0). The archetype fragility model produces unrealistically high results (mean = 2769, median = 2713), reaffirming its strong tendency to overestimate risk. For Hurricane Michael, two utility companies reported repairs or replacements of 519 equivalent transmission structures (excluding known wood transmission poles) (Florida Public Service Commission, 2019, 2020). Comparing this to the central values of N^{initial}, the parameterized fragility model provides the closest estimates (mean = 642, median = 625), while the mean fragility model underpredicts (mean = 154, median = 140). The archetype fragility model again shows substantial overestimation (mean = 3770, median = 3786).

We acknowledge that the above comparison is not a full rigorous validation, as the available data may be incomplete and the historical events inherently include random variability. Nonetheless, it offers a useful sanity check and an indicative benchmark. In both Irma and Michael, the results consistently show that the parameterized fragility model yields the most realistic and reliable damage estimates, the mean fragility model tends to underpredict, and the archetype fragility model substantially overestimates risk. The consistent relative behavior of the three models across both events further supports that these patterns reflect inherent model characteristics rather than event-specific randomness.

A discussion on the systematic bias of the mean and archetype fragility models is provided below. Starting with the mean fragility model, recall that it is defined by fixing the five tuning parameters at their nominal or median values, i.e., $\boldsymbol{X} = \overline{\boldsymbol{X}}$ = (138 kV, 120

mph, 2-peak, 900 ft, 45°). The accuracy/performance of this model depends on the actual distribution and heterogeneity of these parameters across the network. In an idealized, homogeneous system—where all towers share the same properties as the nominal setting and reach their maximum failure probabilities at a yaw angle of 45°—the parameterized and mean fragility models would yield identical results. In reality, however, the portfolio is heterogeneous. The mean fragility model tends to underestimate damage primarily for two reasons. First, at the individual tower level, it cannot capture the temporal chain (or series-system) effect associated with time-varying yaw angles. Although it accounts for time-varying wind speeds, it ignores the changing wind direction during a hurricane, which significantly influences tower response. Because failure is typically governed by the weakest temporal state (often when the yaw angle is near 0°), the mean fragility model misses this critical effect and thus underestimates failure probability. Second, at the portfolio or regional scale, variations in other important parameters—such as design wind speed—also influence the overall damage estimation. If the portfolio contains a larger proportion of vulnerable towers (e.g., with design wind speeds below 120 mph) than represented by the nominal setting, the mean fragility model will underestimate aggregate damage. Conversely, if the portfolio is dominated by stronger towers, it may overestimate risk. This highlights a well-known limitation of using a single mean fragility curve—defined by average structural characteristics—for regional analysis of a heterogeneous portfolio. Mean structural properties rarely guarantee a true 'mean' fragility response and often introduce systematic bias, leading to consistent under- or overestimation. In simple terms, mean input does not necessarily translate to a mean result. In contrast, the flexible, parameterized fragility model provides more objective and robust assessments by explicitly accounting for structure-to-structure variability.

Regarding the overestimation by the archetype fragility curve, a similar mixture effect applies as discussed for the mean fragility model. However, in this case, many towers in

the portfolio are stronger than the 'weak' archetype tower, leading the archetype curve to systematically overpredict failures. We did not intentionally select a weak archetype; it was used simply because it is the only tower fragility model available in the IN-CORE platform. The aim is not to critique this particular archetype, but to illustrate that applying a single fragility curve across a heterogeneous portfolio can produce misleading results, emphasizing the limitations of such an approach.

Using the parameterized model as a reference, for Irma, both the LCC ratio and global efficiency ratio indicate that the mean fragility model slightly underestimates damage (overestimates network performance), while the archetype fragility noticeably overestimates damage (underestimates network performance). For Michael, the trends are similar: the mean fragility model underestimates damage, and the archetype model overestimates it. Overall, based on the parameterized model, Hurricane Michael (mean LCC ratio = 0.92563, mean η_r = 0.92459) causes more severe network damage than Irma (mean LCC ratio = 0.99933, mean η_r = 0.99878), consistent with Michael's greater intensity and inland penetration.

Comparing the two events reveals patterns similar to those observed in transmission line failure probabilities (Table 4.1). For Irma, a lower-intensity event, the archetype fragility model produces much higher dispersion in the three network metrics than the parameterized and mean models (Table 4.2). This occurs because the parameterized and mean models predict very low tower failure probabilities, while the archetype model spans $0-1$, increasing variability. For Michael, a higher-intensity event, the parameterized fragility model generally exhibits the largest standard deviation in the three metrics. This should be because the archetype model is mostly saturated at high maximum tower failure probabilities, reducing dispersion. The parameterized model preserves more variability than the mean model by capturing realistic spatial heterogeneity. The trends in aggregate metrics align with the geospatial observations. The consistent relative behavior of the three mod-

els across all metrics and both hurricanes reinforces that these differences reflect intrinsic model characteristics rather than random event effects.

4.4 Concluding remarks

This study investigated how different regional fragility analysis practices influence hurricane risk assessments of power transmission networks. Using a probabilistic simulation framework, we compared three fragility models for transmission structures: parameterized class fragility model, mean fragility model, and archetype fragility model. The transmission network was represented as a graph, and hurricane wind fields were simulated using a hybrid approach blending the parametric Holland model with ERA5 data. We proposed a novel once-for-all temporal sampling strategy for the class fragility model, computing the maximum tower failure probability over all time steps of a hurricane event. This approach avoids overestimating risk due to activating the embedded inter-structure uncertainty. Spatial correlation of damage was also accounted for using a random field method. Network performance was evaluated using both granular geospatial metrics—edge failure probability and maximum tower failure probability—and aggregate network metrics, including the number of failed towers (with and without cascading), largest connected component ratio, and global efficiency ratio.

We demonstrated the methodology using the hurricane-prone Florida transmission network, considering two historical hurricanes (Irma and Michael) with distinct tracks and impacts. Comparing results across these events allows us to assess whether observed patterns reflect inherent model characteristics rather than random event effects. By benchmarking against available historical damage data (number of failed transmission structures), the parameterized fragility model consistently produced the most realistic and credible results for both hurricanes. Across all metrics, the relative behavior of the three fragility models was

consistent: the mean fragility model tended to underestimate damage, while the archetype fragility model substantially overestimated risk. The parameterized model captures realistic spatial heterogeneity through its tuning parameters, providing a finer-grained fragility definition, higher-resolution damage assessments, and in turn more accurate aggregate network metrics. These findings align with Rincon and Padgett (2024), highlighting that the resolution in portfolio fragility modeling could impact the risk outcomes significantly and lead to very different conclusions. Therefore, parameterized class fragility models are recommended for more reliable and adaptable hurricane risk and resilience analysis of power transmission networks, enabling more objective and informed decision-making.

While the results are consistent across two events, multiple metrics, and a large network, they are specific to the three fragility models and the network/portfolio considered in this study. As discussed, the relative behavior of the mean and archetype fragility models—whether they underestimate or overestimate risk—may vary with portfolio heterogeneity, characteristics, and the selected fragility models. This underscores a key limitation of low-resolution portfolio modeling approaches: they lack robustness and flexibility and can easily skew results if the model is not carefully chosen. The main conclusion remains: parameterized class fragility models are better suited for regional risk analysis. This promotes the broader development and use of flexible, parameterized fragility models for other hazards and infrastructure types, to enable more accurate regional risk assessment. The framework presented here can be generalized to other comparative studies involving different hazards or asset types. In particular, the once-for-all temporal sampling strategy is valuable for long-duration hazards and for using class fragility models where inter-structure uncertainty must be carefully handled. Other temporal effects—such as tower aging due to corrosion or fatigue, and damage accumulation either within a single event or across multiple events—are not considered in this study, and their impacts should be explored in future work. Future studies could also enhance the analysis by incorporating power flow–enabled metrics, such

as outage modeling; however, this requires detailed electrical data, which is often difficult to obtain for security reasons, especially for large-scale networks.

Chapter 5

Conclusions

5.1 Summary

This dissertation develops a comprehensive framework for modeling and analyzing the hurricane vulnerability of lattice transmission towers and power transmission networks at the regional scale. Recognizing the need to balance model fidelity with computational tractability, the research progresses from physics-based surrogate modeling of individual tower panels to parameterized class fragility modeling and finally to network-scale hurricane risk assessment. Together, the three studies collectively advance both the methodological foundation and the practical applicability of fragility-based regional risk analysis for electric power infrastructure.

The first study abstracted panels as the basic components of lattice transmission towers and proposed a **physics-based surrogate analytical model** that enables efficient panel-level finite element representation of towers. Through systematic numerical experiments on straight and inclined panels, the study established consistent definitions for failure limit state and engineering demand parameters (EDPs) and proposed axial force–bending moment (PMM) limit capacity surfaces for panels. The surrogate model—implemented using an elastic beam-column element with condensed stiffness parameters—was shown to reproduce the EDPs of high-fidelity panel models with negligible loss of accuracy. When applied to full-tower simulations, the surrogate-based approach reduced computational time by several orders of magnitude while maintaining acceptable accuracy for portfolio-level

analyses. These findings demonstrated that physics-based surrogate modeling provides an efficient and scalable foundation for modeling tower heterogeneity in regional studies.

Building on this foundation, the second study developed a **parameterized fragility model** for a representative class of transmission towers under hurricane winds, focusing on the Florida transmission network. The study refined an eight-step framework for deriving class fragility models, highlighting several original details and recommendations for best practice. The fragility model was parameterized using five tuning parameters—voltage, design wind speed, span length, number of peaks, and yaw angle—allowing fragility curves to adapt flexibly to variations across a portfolio. Sensitivity analyses revealed that design wind speed, span length, and yaw angle were the most influential parameters governing tower fragility. The presented framework offers a generalizable methodology for developing parameterized fragility models for other hazards and infrastructure asset types.

The third study extended the investigation to the network scale, examining how different fragility modeling practices influence **hurricane risk assessments of transmission networks**. A probabilistic simulation framework was used that integrates hurricane wind field simulation, spatial correlation of structural damage, and network performance analysis. Three fragility modeling approaches—archetype fragility, mean fragility, and parameterized class fragility—were compared using historical Hurricanes Irma and Michael as case studies. The parameterized class fragility model consistently produced the most realistic and credible risk estimates when benchmarked against observed damage data, while the mean and archetype models respectively under- and overestimated network damage. A novel 'once-for-all' temporal sampling strategy was introduced for using class fragility models to avoid overestimating risk from evoking the embedded inter-structure uncertainty. The study highlighted the critical role of fragility resolution in regional risk assessment, showing that flexible, parameterized fragility models lead to more granular and reliable risk characterizations.

5.2 Contributions

An overview of the research activities conducted during the Ph.D. program is provided in Section 1.2. This dissertation presents a subset of those studies, and the key contributions of the presented work are summarized as follows:

1. A physics-based surrogate analytical model for panels is developed to enable efficient modeling of portfolios of transmission towers. Beyond the specific model proposed, a major contribution is the formulation of a rational procedure for developing and evaluating mechanical models suitable for large-scale probabilistic analysis. This procedure can be extended to alternative surrogate formulations that balance accuracy and computational cost differently or target other structural systems. For example, future studies could explore nonlinear beam elements as panel surrogates or adapt the procedure to develop panel-based surrogate models for telecommunication towers, following similar calibration and validation steps.

2. A parameterized fragility model for a general class of transmission towers is derived—the first of its kind for this asset type. The model enables more granular fragility assessment at the portfolio or network scale and is publicly available in Wang and Bocchini (2025a). While the presented framework is broadly applicable to developing parameterized fragility models for various hazards and asset types, its application to transmission towers demonstrates particular relevance for similar slender structures, such as other transmission or telecommunication towers.

3. The influence of different regional fragility analysis practices on hurricane risk assessments of power transmission networks is investigated. The parameterized model captures realistic spatial heterogeneity through its tuning parameters, resulting in finer-grained fragility definitions, higher-resolution damage estimates, and more ac-

curate network-level performance metrics. The framework presented here can be generalized to other comparative studies targeting different hazards or asset types. In addition, the simulated hurricane wind fields used in this study are publicly available in Wang and Bocchini (2025c).

Additional contributions from other studies not included in this dissertation, as well as secondary contributions from all studies, are summarized as follows:

1. A mechanistic and probabilistic methodology is proposed to assess wildfire ignition risk from conductor-vegetation contact during high-wind events. The encroachment mechanism is modeled through dynamic transmission line response and random vibration theory. This approach enables sensitivity analyses and supports operational decisions (e.g., power shutoff and vegetation management) by quantifying the probability of conductor-vegetation interaction under varying wind and clearance conditions.

2. A dynamic traffic–based framework is developed for transportation network resilience assessment, integrating time-dependent functionality analysis with mesoscopic traffic simulations. The results demonstrate that dynamic (rather than static) modeling captures spatiotemporal congestion patterns and localized impacts of disruptions such as earthquakes and protests, thus providing deeper insight into system behavior and supporting more informed resilience planning.

3. A wind hazard map of extreme wind gusts with a 20-year return period is created for the state of California using historical wind data and GIS analysis. This map earned media coverage (Venteicher et al., 2023) and helped raise public awareness of regional wind and wildfire risks.

4. The effectiveness and accuracy of the proposed surrogate model for lattice panels

are thoroughly examined. The model successfully captures structural responses, including potential nonlinear effects arising from material behavior and connection slippage, despite its linear element formulation. This capability is achieved through rigorous physics-based parameter mapping and calibration against high-fidelity models.

5. An expert opinion survey on post-storm power restoration is collaboratively conducted (as a contributor). The survey, designed in Qualtrics and distributed to professional linemen and grid operators, yielded valuable responses and was complemented by interviews for deeper insight.

Appendix A

Commonly used angle profiles

In the spirit of providing all necessary information for reproducing the results, Table A.1 lists the common angle profiles used in the design of experiments in Section 2.3.1. The indices are arranged in ascending order of sectional area.

Table A.1: Database of commonly used angle profiles.

Index by area	Profile in × in × in	Area in^2 (mm^2)	Index by area	Profile in × in × in	Area in^2 (mm^2)
1	$2 \times 2 \times 0.125$	0.48 (310)	32	$4 \times 4 \times 0.625$	4.61 (2974)
2	$2 \times 2 \times 0.1875$	0.71 (458)	35	$4 \times 4 \times 0.75$	5.44 (3510)
4	$2 \times 2 \times 0.25$	0.94 (606)	24	$5 \times 5 \times 0.3125$	3.03 (1955)
6	$2 \times 2 \times 0.3125$	1.15 (742)	27	$5 \times 5 \times 0.375$	3.61 (2329)
8	$2 \times 2 \times 0.375$	1.36 (877)	30	$5 \times 5 \times 0.4375$	4.18 (2697)
3	$2.5 \times 2.5 \times 0.1875$	0.902 (582)	33	$5 \times 5 \times 0.5$	4.75 (3065)
7	$2.5 \times 2.5 \times 0.25$	1.19 (768)	37	$5 \times 5 \times 0.625$	5.86 (3781)
10	$2.5 \times 2.5 \times 0.3125$	1.46 (942)	39	$5 \times 5 \times 0.75$	6.94 (4477)
12	$2.5 \times 2.5 \times 0.375$	1.73 (1116)	42	$5 \times 5 \times 0.875$	7.98 (5148)
17	$2.5 \times 2.5 \times 0.5$	2.25 (1452)	28	$6 \times 6 \times 0.3125$	3.65 (2355)
5	$3 \times 3 \times 0.1875$	1.09 (703)	31	$6 \times 6 \times 0.375$	4.36 (2813)
9	$3 \times 3 \times 0.25$	1.44 (929)	34	$6 \times 6 \times 0.4375$	5.06 (3265)
13	$3 \times 3 \times 0.3125$	1.78 (1148)	36	$6 \times 6 \times 0.5$	5.75 (3710)
16	$3 \times 3 \times 0.375$	2.11 (1361)	38	$6 \times 6 \times 0.5625$	6.43 (4148)
19	$3 \times 3 \times 0.4375$	2.43 (1568)	40	$6 \times 6 \times 0.625$	7.11 (4587)
21	$3 \times 3 \times 0.5$	2.75 (1774)	43	$6 \times 6 \times 0.75$	8.44 (5445)
11	$3.5 \times 3.5 \times 0.25$	1.69 (1090)	46	$6 \times 6 \times 0.875$	9.73 (6277)
15	$3.5 \times 3.5 \times 0.3125$	2.09 (1348)	47	$6 \times 6 \times 1$	11 (7097)
20	$3.5 \times 3.5 \times 0.375$	2.48 (1600)	41	$8 \times 8 \times 0.5$	7.75 (5000)
23	$3.5 \times 3.5 \times 0.4375$	2.87 (1852)	44	$8 \times 8 \times 0.5625$	8.68 (5600)
25	$3.5 \times 3.5 \times 0.5$	3.25 (2097)	45	$8 \times 8 \times 0.625$	9.61 (6200)
14	$4 \times 4 \times 0.25$	1.94 (1252)	48	$8 \times 8 \times 0.75$	11.44 (7381)
18	$4 \times 4 \times 0.3125$	2.4 (1548)	49	$8 \times 8 \times 0.875$	13.23 (8535)
22	$4 \times 4 \times 0.375$	2.86 (1845)	50	$8 \times 8 \times 1$	15 (9677)
26	$4 \times 4 \times 0.4375$	3.31 (2135)	51	$8 \times 8 \times 1.125$	16.73 (10794)
29	$4 \times 4 \times 0.5$	3.75 (2419)			

Appendix B

Verification study of PMM capacity surfaces

Transmission towers have traditionally been studied at the member level because the primary failure mode is member buckling. To the authors' knowledge, no prior research—either experimental or numerical—has investigated the PMM capacities of full panels. In order to gain a better understanding of the PMM capacity surfaces, two small batches of numerical experiments were conducted for the straight and inclined panel types. For each panel type, 50 panels were sampled using the DoE strategy described in Section 2.3.1. One inclined panel sample incurred non-permissible design and thus was discarded. Then, for each sampled panel, its PMM limit capacity surface was constructed point by point based on the flowchart shown in Figure 2.10, where 50 different target loading patterns (i.e., $N = 50$) were generated by the LHS technique.

Figure B.1 illustrates the PMM capacity surfaces for two example panels, where the 50 mirrored points are obtained from symmetry (see Figure 2.8). Visual inspection of all the 99 surfaces indicates that the PMM capacity surfaces of both panel types can be characterized as planes in the PMM 3D space. To more rigorously verify this hypothesis, the capacity points constituting each surface were fitted to a plane and the goodness of fit was evaluated. The least square method was utilized for the surface fitting and its quality was quantified by the coefficient of determination (R^2). For the 50 PMM capacity surfaces of the straight panels, the minimum, maximum and mean of the R^2 values were found to be 0.99949, 1.00000, and 0.99999 respectively. For the 49 PMM capacity surfaces of the inclined panels, the minimum, maximum and mean of the R^2 values were evaluated 0.99944,

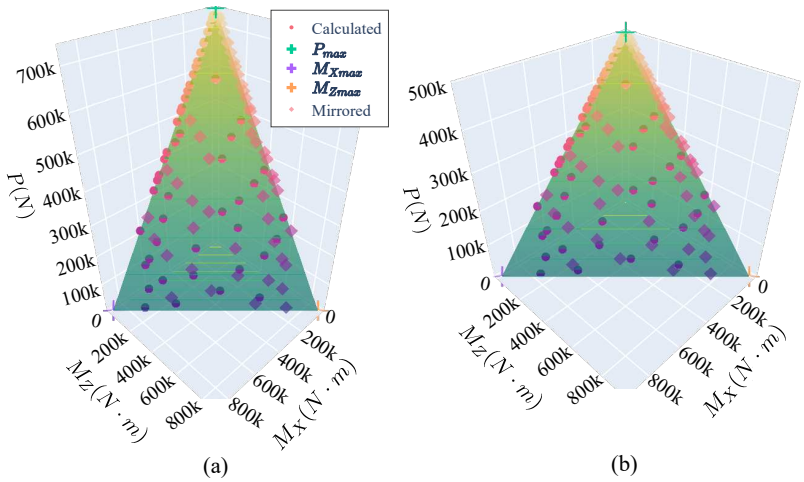

Figure B.1: Example PMM capacity surfaces in the 3D space: (a) a straight panel ($w_t = 2.335$m, $s_{\text{leg}} = 14$, $s_{\text{brace}} = 13$); (b) an inclined panel ($w_t = 3.458$m, $s_{\text{leg}} = 9$, $s_{\text{brace}} = 9$). For brevity, the sampled values of the other eight variables are omitted here.

1.00000, and 0.99993 respectively. The R^2 values are all very close to 1, supporting the hypothesis that the PMM capacity surfaces of both panel types are well represented as planes, as the nonlinearity introduced by the joint behavior is negligible in practice.

It is known that three non-collinear points can define a plane in the 3D space. Figure B.1 further suggests that the capacity plane can be determined by three particular points—$(P_{\text{max}}, 0, 0)$, $(0, M_{X\text{max}}, 0)$, and $(0, 0, M_{Z\text{max}})$—where $M_{X\text{max}} = M_{Z\text{max}}$ due to symmetry. Therefore, the limit capacity plane of a panel can be fully characterized by knowing P_{max} and $M_{X\text{max}}$. To accurately determine these two quantities, the high-fidelity approach is recommended over the simple truss approach. This recommendation is based on a quantitative comparison using the 50 straight panels and 49 inclined panels discussed above. In the comparison study, both approaches employed the panel design routine (see Figure 2.6) to determine the buckling lengths, following which the compression capacities (P_c) of leg members were calculated from the equations provided in Section 2.2.4. The high-fidelity approach determines P_{max} and $M_{X\text{max}}$ through finite element analysis of the 3-panel structure model; the simple truss approach estimates $P_{\text{max}} = 4P_c/\cos(\alpha_p)$ and $M_{X\text{max}} = 2P_c w_t/\cos(\alpha_p)$, utilizing prominent simplifications by neglecting beam-column

behavior, connection effects, indeterminacy, etc.

Figure B.2 illustrates the discrepancies between the two approaches (see the white box plots) in the computed $P_{\max}$ and $M_{X\max}$ for straight and inclined panels. The mean percentage differences for 'straight, $P_{\max}$', 'straight, $M_{X\max}$', 'inclined, $P_{\max}$', and 'inclined, $M_{X\max}$' are 4.2%, 3.4%, 7.7%, and 12.4%, respectively. This level of average discrepancy justifies the conventional use of the simple truss approach in certain cases. However, significant discrepancies can arise, as indicated by the maximum percentage differences: 24.8%, 19.0%, 38.3%, and 36.3%. Notably, the discrepancies are larger in inclined panels compared to straight panels. This is likely because the slope/inclination increases the influence of connections and bracings, resulting in more complex structural behavior that the simple truss approach fails to account for. Since the simple truss approach can yield unacceptably large discrepancies, the high-fidelity approach should be used as the basis for a more reliable and accurate determination of $P_{\max}$ and $M_{X\max}$. For a complete comparison, the metamodel—trained on data obtained from the high-fidelity approach—exhibits superior accuracy, as shown by the colored box plots in Figure B.2. The mean percentage differences for 'straight, $P_{\max}$', 'straight, $M_{X\max}$', 'inclined, $P_{\max}$', and 'inclined, $M_{X\max}$' are 1.8%, 2.0%, 2.6%, and 2.2%, respectively. The maximum percentage differences are: 7.0%, 10.4%, 5.4%, and 5.7%.

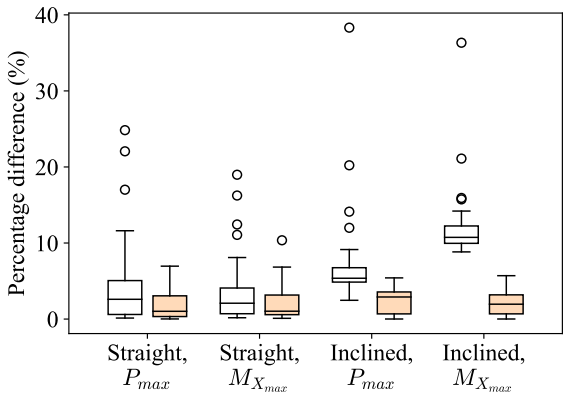

Figure B.2: Discrepancies in computed $P_{\max}$ and $M_{X\max}$. The simple truss approach and the meta-model prediction are compared to the high-fidelity approach, as illustrated by the white and colored box plots, respectively.

Appendix C

Coefficients of the metamodel

The detailed coefficients corresponding to the metamodel in Equation (2.22) are summarized in Table C.1.

Table C.1: Coefficients of the metamodel.

Type	Straight			Inclined		
Purpose	Capacity		Demand	Capacity		Demand
$\hat{Y}$	$P_{\max}$ (N)	$M_{X\max}$ (N·m)	K_{ss} (N)	$P_{\max}$ (N)	$M_{X\max}$ (N·m)	K_{ss} (N)
θ_0	3.061×10^6	2.614×10^6	4.371×10^7	1.399×10^6	1.782×10^6	8.585×10^7
θ_1	1.969×10^5	-6.259×10^3	7.733×10^6	-8.974×10^4	-3.158×10^4	2.180×10^7
θ_2	5.517×10^5	-1.940×10^6	1.505×10^7	4.599×10^5	-5.457×10^5	3.116×10^7
θ_3	3.047×10^5	1.770×10^5	8.131×10^6	-1.047×10^4	-1.306×10^5	1.798×10^7
θ_4	2.531×10^5	2.709×10^5	-3.081×10^6	6.875×10^4	1.698×10^5	-1.898×10^6
θ_5	1.093×10^5	3.348×10^4	-3.508×10^5	-1.762×10^4	2.995×10^4	1.910×10^6
θ_6	-5.532×10^5	2.248×10^6	-1.430×10^6	-4.859×10^5	9.360×10^5	6.235×10^6
θ_7	-7.652×10^4	-6.316×10^4	-3.664×10^6	-1.554×10^4	3.032×10^4	3.609×10^6
θ_8	-7.952×10^4	-9.019×10^4	-2.202×10^6	1.131×10^4	-6.672×10^4	-1.031×10^7
θ_9	-4.235×10^5	2.448×10^5	-1.553×10^6	-2.632×10^5	6.820×10^3	3.697×10^6
θ_{10}	8.192×10^3	9.656×10^3	1.417×10^6	3.260×10^1	1.287×10^5	4.097×10^6
θ_{11}	1.204×10^4	-3.366×10^4	-2.569×10^6	8.852×10^3	-6.033×10^4	-9.848×10^6
θ_{12}	2.574×10^6	2.144×10^6	3.860×10^6	1.178×10^6	9.468×10^5	5.648×10^6
θ_{13}	-1.518×10^4	-9.710×10^3	-1.432×10^6	-4.393×10^3	7.109×10^3	-7.540×10^6
θ_{14}	-1.289×10^5	-7.026×10^4	5.478×10^6	1.797×10^5	2.759×10^5	-1.381×10^6
θ_{15}	-2.171×10^5	-2.422×10^5	4.559×10^6	-8.969×10^4	-1.606×10^5	1.737×10^6
θ_{16}	1.420×10^5	-3.184×10^5	1.369×10^6	3.994×10^5	-1.621×10^4	-1.713×10^6
θ_{17}	3.320×10^5	3.056×10^5	-8.836×10^6	2.184×10^5	2.329×10^5	-2.290×10^7
θ_{18}	-4.704×10^4	-1.392×10^4	-5.460×10^6	-1.195×10^5	-1.758×10^5	-9.359×10^6
θ_{19}	1.270×10^4	3.747×10^4	-1.552×10^6	-9.356×10^3	2.880×10^4	4.859×10^6
θ_{20}	6.844×10^4	-1.502×10^5	-1.686×10^6	5.331×10^2	-6.693×10^4	-4.338×10^6

Appendix D

Data used in tower design module

Table D.1: Database of commonly used transmission conductors (adapted from Kalaga and Yenumula (2017)). All conductors are of the aluminum conductor steel reinforced (ACSR) type.

No.	Label	Size (kcmil)	Area (in^2)	Stranding	Diameter (in)	Unit weight (lb/ft)	RTS (lb)	Applicable voltage (kV)
1	Penguin	266.8	0.1939	6/1	0.563	0.2911	8350	115
2	Linnet	336.4	0.3069	26/7	0.721	0.463	14100	115, 138
3	Pelican	477	0.3952	18/1	0.814	0.518	11800	115, 138
4	Hawk	477	0.4355	26/7	0.858	0.657	19500	115, 138
5	Dove	556.5	0.5084	26/7	0.927	0.766	22600	115, 138
6	Drake	795	0.7269	26/7	1.108	1.094	31500	115, 138, 230
7	Tern	795	0.668	45/7	1.063	0.896	22100	115, 138, 230
8	Rail	954	0.8013	45/7	1.165	1.075	25900	115, 138, 230
9	Cardinal	954	0.8462	54/7	1.196	1.229	33800	115, 138, 230
10	Bittern	1272	1.0679	45/7	1.345	1.434	34100	115, 138, 230
11	Falcon	1590	1.4073	54/19	1.545	2.044	54500	115, 138, 230
12	Kiwi	2167	1.7762	72/7	1.735	2.3005	49800	115, 138, 230
13	Bluebird	2156	1.8304	84/19	1.762	2.511	60300	115, 138, 230

Note: 1 in = 25.4 mm, 1 lb/ft = 14.6 N/m, 1 lb = 4.45 N, 1 ft = 0.3048 m.

Table D.2: Database of common overhead ground wires (adapted from Kalaga and Yenumula (2017)).

No.	Label	Material	Diameter (in)	Area (in^2)	Unit weight (lb/ft)	RTS (lb)
1	3#6 AW	Alumoweld	0.35	0.077	0.178	10280
2	7#8 AW	Alumoweld	0.385	0.091	0.262	15930
3	7#9 AW	Alumoweld	0.343	0.072	0.208	12630
4	3/8 HS	Steel	0.36	0.079	0.273	10800
5	3/8 EHS	Steel	0.36	0.079	0.273	15400
6	7/16 HS	Steel	0.435	0.149	0.399	14500
7	7/16 EHS	Steel	0.435	0.149	0.399	20800

Note: 1 in = 25.4 mm, 1 lb/ft = 14.6 N/m, 1 lb = 4.45 N, 1 ft = 0.3048 m.

References

American Nuclear Society [1982]. "PRA procedures guide." *Report No. NUREG/CR-2300, Vol. 1*, American Nuclear Society, La Grange Park, IL; Institute of Electrical and Electronics Engineers, Inc., New York (USA).

American Society of Civil Engineers (ASCE) [2023]. "Raster Dataset (ASCE/SEI 7-10 50-year Wind Map) — Image Service". Retrieved from `https://www.arcgis.com/apps/mapviewer/index.html?url=https://gis.asce.org/arcgis/rest/services/ASCE/wind2010_50/ImageServer&source=sd`.

Ancheta, T., Darragh, R., Stewart, J., Seyhan, E., Silva, W., Chiou, B., Wooddell, K., Graves, R., Kottke, A., Boore, D., Kishida, T., and Donahue, J. [2014]. "NGA-West2 Ground Motion Database". Retrieved from `https://ngawest2.berkeley.edu/`.

Anderson, E. et al. [2020]. "pyDOE3: The Experimental Design Package for Python".

ASCE [2015]. *Design of Latticed Steel Transmission Structures*. American Society of Civil Engineers, Reston, VA.

ASCE [2016]. *Minimum Design Loads and Associated Criteria for Buildings and Other Structures*. American Society of Civil Engineers, Reston, VA.

Baker, J. W. [2015]. "Efficient analytical fragility function fitting using dynamic structural analysis." *Earthquake Spectra*, 31(1), 579–599.

Baker, J. W., Almeter, E., Cook, D., Liel, A. B., and Haselton, C. [2024]. "A model for

partially dependent component damage fragilities in seismic risk analysis." *Earthquake Spectra*, 40(1), 609–628.

Bocchini, P., Frangopol, D. M., and Deodatis, G. [2011]. "A random field based technique for the efficiency enhancement of bridge network life-cycle analysis under uncertainty." *Engineering Structures*, 33(12), 3208–3217.

Britton, J. and Bouslog, T. [2015]. "Considerations in the Development of a Lattice Tower Structure Family." *Electrical Transmission and Substation Structures*, Branson, MO, American Society of Civil Engineers, 387–400.

Cai, Y., Xie, Q., Xue, S., Hu, L., and Kareem, A. [2019]. "Fragility modelling framework for transmission line towers under winds." *Engineering Structures*, 191, 686–697.

Catchpole, P. and Fife, B. [2014]. *Structural Engineering of Transmission Lines*. ICE Publishing, London, UK.

Chavas, D. R., Lin, N., and Emanuel, K. [2015]. "A model for the complete radial structure of the tropical cyclone wind field. Part I: Comparison with observed structure." *Journal of the Atmospheric Sciences*, 72(9), 3647–3662.

Chen, B., Weng, S., Zhi, L., and Li, D. [2016]. "Response control of a large transmission tower-line system under seismic excitations using friction dampers." *Advances in Structural Engineering*, 20(8), 1155–1173.

Chen, L., Huang, C., Chen, H., and Zheng, Z. [2022]. "Seismic fragility models of a bridge system based on copula method." *Earthquake Spectra*, 38(2), 1417–1437.

Chen, L., Mo, R., Chen, Y., Guo, Z., and Zheng, Z. [2024]. "Investigation of intraclass correlation of seismic capacity for rc bridge piers based on hierarchical model." *ASCE-ASME Journal of Risk and Uncertainty in Engineering Systems, Part A: Civil Engineering*, 10(3), 04024041.

Chicco, D., Warrens, M. J., and Jurman, G. [2021]. "The coefficient of determination R-squared is more informative than SMAPE, MAE, MAPE, MSE and RMSE in regression analysis evaluation." *PeerJ Computer Science*, 7, e623.

CIGRÉ Study Committee B2 [2016]. "Sag-tension calculation methods for overhead lines." *Report no.*, CIGRÉ. First edition: June 2007; Revision: April 2016.

Cimellaro, G. P., Reinhorn, A. M., and Bruneau, M. [2010]. "Framework for analytical quantification of disaster resilience." *Engineering Structures*, 32(11), 3639–3649.

d'Aragona, M. G., Polese, M., and Prota, A. [2020]. "Stick-IT: A simplified model for rapid estimation of IDR and PFA for existing low-rise symmetric infilled RC building typologies." *Engineering Structures*, 223, 111182.

de Souza, R. R., Miguel, L. F. F., Kaminski Jr, J., and Lopez, R. H. [2019]. "Topology design recommendations of transmission line towers to minimize the bolt slippage effect." *Engineering Structures*, 178, 286–297.

de Souza, R. R., Miguel, L. F. F., Lopez, R. H., Miguel, L. F. F., and Torii, A. J. [2016]. "A procedure for the size, shape and topology optimization of transmission line tower structures." *Engineering Structures*, 111, 162–184.

Deierlein, G. G., McKenna, F., Zsarnóczay, A., Kijewski-Correa, T., Kareem, A., Elhaddad, W., Lowes, L., Schoettler, M. J., and Govindjee, S. [2020]. "A cloud-enabled application framework for simulating regional-scale impacts of natural hazards on the built environment." *Frontiers in Built Environment*, 6, 558706.

Deodatis, G. [1996]. "Simulation of ergodic multivariate stochastic processes." *Journal of engineering mechanics*, 122(8), 778–787.

Dikshit, S. and Alipour, A. [2023]. "A moment-matching method for fragility analysis of

transmission towers under straight line winds." *Reliability Engineering & System Safety*, 236, 109241.

Dikshit, S., Dobson, I., and Alipour, A. [2024]. "Cascading structural failures of towers in an electric power transmission line due to straight line winds." *Reliability Engineering & System Safety*, 250, 110304.

Douglas, D. H. and Peucker, T. K. [1973]. "Algorithms for the reduction of the number of points required to represent a digitized line or its caricature." *Cartographica*, 10(2), 112–122.

Du, X. and Hajjar, J. F. [2022]. "Nonlinear dynamic analysis and fragility development of electrical transmission towers under hurricanes." *Proceedings of the Annual Stability Conference*, Denver, CO.

Ellingwood, B. R. and Tekie, P. B. [1999]. "Wind Load Statistics for Probability-Based Structural Design." *Journal of Structural Engineering*, 125(4), 453–463.

Fang, S., Roy, S., and Kramer, J. [1997]. *"Transmission Structures" Structural Engineering Handbook*. CRC Press, Boca Raton, FL.

FEMA [2020]. *Hazus Earthquake Model Technical Manual*. Federal Emergency Management Agency.

FEMA [2021]. *Hazus Hurricane Model Technical Manual*. Federal Emergency Management Agency.

FHWA [n.d.]. *National Bridge Inventory*. Federal Highway Administration. Retrieved from `https://www.fhwa.dot.gov/bridge/nbi.cfm`.

Florida Public Service Commission [2018]. "Review of Florida's electric utility hurricane preparedness and restoration actions, 2018." *Technical report*, Florida

Public Service Commission (July). Retrieved from https://www.floridapsc.com/pscfiles/website-files/PDF/Publications/Reports/ElectricGas/UtilityHurricanePreparednessRestorationActions2018.pdf.

Florida Public Service Commission [2019]. "In Re: Petition for Limited Proceeding for Recovery of Incremental Storm Restoration Costs Related to Hurricane Michael and Tropical Storm Alberto." *Technical report*, Florida Public Service Commission (November). Retrieved from https://www.psc.state.fl.us/library/filings/2019/11075-2019/11075-2019.pdf.

Florida Public Service Commission [2020]. "In re: Application for recovery of storm restoration costs and other relief." *Technical report*, Florida Public Service Commission. Retrieved from https://www.psc.state.fl.us/library/filings/2020/09268-2020/09268-2020.pdf.

Fu, X., Li, H.-N., Tian, L., Wang, J., and Cheng, H. [2019]. "Fragility Analysis of Transmission Line Subjected to Wind Loading." *Journal of Performance of Constructed Facilities*, 33(4), 04019044.

Gahtan, J., Knapp, K. R., Schreck, C. J., Diamond, H. J., Kossin, J. P., and Kruk, M. C. [2024]. "International Best Track Archive for Climate Stewardship (IBTrACS) Project, Version 4r01". Accessed on 11-Nov-2025.

Ghosh, J., Padgett, J. E., and Dueñas-Osorio, L. [2013]. "Surrogate modeling and failure surface visualization for efficient seismic vulnerability assessment of highway bridges." *Probabilistic Engineering Mechanics*, 34, 189–199.

Giovenale, P., Cornell, C. A., and Esteva, L. [2004]. "Comparing the adequacy of alternative ground motion intensity measures for the estimation of structural responses." *Earthquake engineering & structural dynamics*, 33(8), 951–979.

Goda, K. and Tesfamariam, S. [2015]. "Multi-variate seismic demand modelling using copulas: Application to non-ductile reinforced concrete frame in victoria, canada." *Structural Safety*, 56, 39–51.

Gokkaya, B., Baker, J., and Deierlein, G. [2017]. "Estimation and impacts of model parameter correlation for seismic performance assessment of reinforced concrete structures." *Structural Safety*, 69, 68–78.

Gong, J. and Zhi, X. [2020]. "Earthquake failure mode and collapse fragility of a 1000 kV outgoing line frame considering interactions in the tower line system." *Structures*, 27, 626–638.

Google LLC [n.d.]. "Google Earth Pro [Computer software]".

Hagberg, A. A., Schult, D. A., and Swart, P. J. [2008]. "Exploring network structure, dynamics, and function using networkx." *Proceedings of the 7th Python in Science Conference*, G. Varoquaux, T. Vaught, and J. Millman, eds., Pasadena, CA USA, 11 – 15.

Heresi, P. and Miranda, E. [2022]. "Structure-to-structure damage correlation for scenario-based regional seismic risk assessment." *Structural Safety*, 95, 102155.

Hersbach, H., Bell, B., Berrisford, P., Biavati, G., Horányi, A., Muñoz Sabater, J., Nicolas, J., Peubey, C., Radu, R., Rozum, I., Schepers, D., Simmons, A., Soci, C., Dee, D., and Thépaut, J.-N. [2023]. "ERA5 hourly data on single levels from 1940 to present". Accessed on 11-Nov-2025.

Hoerl, A. E. and Kennard, R. W. [2000]. "Ridge Regression: Biased Estimation for Nonorthogonal Problems." *Technometrics*, 42(1), 80–86.

Holland, G. J. [1980]. "An analytic model of the wind and pressure profiles in hurricanes.

Holmes, J. D. [2007]. *Wind loading of structures*. CRC press.

Homeland Infrastructure Foundation-Level Data (HIFLD) [2022]. "Electric Power Transmission Lines", https://catalog.data.gov/dataset/electric-power-transmission-lines. Metadata updated 2022-11-02; Accessed: 2024-07-28 (no longer publicly available).

Homeland Infrastructure Foundation-Level Data (HIFLD) [2023]. "Electric Substations", https://catalog.data.gov/dataset/electric-substations. Metadata last updated 17-Sep-2023; Accessed: 2024-07-28 (no longer publicly available).

Huang, X. and Wang, N. [2024]. "An adaptive nested dynamic downscaling strategy of wind-field for real-time risk forecast of power transmission systems during tropical cyclones." *Reliability Engineering & System Safety*, 242, 109731.

IN-CORE [2024]. "IN-CORE Tool Suite". Retrieved from https://tools.in-core.org/.

Jarry, P. [n.d.]. "Double-circuit transmission tower [Photograph]". Retrieved from https://unsplash.com/@pierrejarry.

Jiang, W.-Q., Liu, Y.-P., Chan, S.-L., and Wang, Z.-Q. [2017]. "Direct Analysis of an Ultrahigh-Voltage Lattice Transmission Tower Considering Joint Effects." *Journal of Structural Engineering*, 143(5), 04017009.

Kalaga, S. and Yenumula, P. [2017]. *Design of Electrical Transmission Lines: Structures and Foundations. Volume I.* CRC Press, Boca Raton, FL.

Karamlou, A. and Bocchini, P. [2015]. "Computation of bridge seismic fragility by large-scale simulation for probabilistic resilience analysis." *Earthquake Engineering & Structural Dynamics*, 44(12), 1959–1978.

Khazaali, M., Christou, V., and Bocchini, P. [2022]. "Classification protocol and com-

prehensive database of vertically correlated longitudinal wind velocities for structural analysis and risk assessment." *Journal of Structural Engineering*, 148(1), 06021006.

Knapp, K. R., Kruk, M. C., Levinson, D. H., Diamond, H. J., and Neumann, C. J. [2010]. "The International Best Track Archive for Climate Stewardship (IBTrACS): Unifying tropical cyclone best track data." *Bulletin of the American Meteorological Society*, 91, 363–376.

Kravitz, R. A. [1985]. *Design Manual for Transmission Line, Tower, and Foundation*. AJIKAWA IRON WORKS & CONSTRUCTION CO., LTD.

Kucherenko, S., Tarantola, S., and Annoni, P. [2012]. "Estimation of global sensitivity indices for models with dependent variables." *Computer physics communications*, 183(4), 937–946.

Lataniotis, C., Marelli, S., and Sudret, B. [2015]. "UQLab user manual–The Input module." *Report UQLab-V0*, 9–102.

Li, H.-N., Shi, W.-L., Wang, G.-X., and Jia, L.-G. [2005]. "Simplified models and experimental verification for coupled transmission tower–line system to seismic excitations." *Journal of Sound and Vibration*, 286(3), 569–585.

Liu, G., Jiang, S., Zheng, M., Lin, S., Kong, Y., and Zhan, P. [2025]. "A global ERA5-based tropical cyclone wind field dataset enhanced by integrated parametric correction methods." *Scientific Data*, 12(1), 1429.

Liu, Y. and Singh, C. [2010]. "A methodology for evaluation of hurricane impact on composite power system reliability." *IEEE Transactions on Power Systems*, 26(1), 145–152.

Lu, X., McKenna, F., Cheng, Q., Xu, Z., Zeng, X., and Mahin, S. A. [2020]. "An open-source framework for regional earthquake loss estimation using the city-scale nonlinear time history analysis." *Earthquake Spectra*, 36(2), 806–831.

Ma, L., Bocchini, P., and Christou, V. [2020]. "Fragility models of electrical conductors in power transmission networks subjected to hurricanes." *Structural Safety*, 82, 101890.

Ma, L., Christou, V., and Bocchini, P. [2022]. "Framework for probabilistic simulation of power transmission network performance under hurricanes." *Reliability Engineering & System Safety*, 217, 108072.

Ma, L., Khazaali, M., and Bocchini, P. [2021a]. "Component-based fragility analysis of transmission towers subjected to hurricane wind load." *Engineering Structures*, 242, 112586.

Ma, X., Zhou, H., and Li, Z. [2021b]. "On the resilience of modern power systems: A complex network perspective." *Renewable and Sustainable Energy Reviews*, 152, 111646.

Macedo, F. C., Alminhana, F., Miguel, L. F. F., and Beck, A. T. [2024]. "Performance-based reliability assessment of transmission lines under tornado actions." *Reliability Engineering & System Safety*, 252, 110475.

Mara, T. G. [2013]. *Capacity assessment of a transmission tower under wind loading*. The University of Western Ontario (Canada).

Marelli, S., Lamas, C., Konakli, K., Mylonas, C., Wiederkehr, P., and Sudret, B. [2019]. "Uqlab user manual–sensitivity analysis." *Report UQLab-V1*, 2–106.

McKenna, F., Scott, M. H., and Fenves, G. L. [2010]. "Nonlinear Finite-Element Analysis Software Architecture Using Object Composition." *Journal of Computing in Civil Engineering*, 24(1), 95–107.

Melchers, R. E. and Beck, A. T. [2018]. *Structural Reliability Analysis and Prediction*. John Wiley & Sons, Hoboken, NJ.

Miguel, L. F. F., Alminhana, F., Brito, J. W. S., Sousa, D. M., and Beck, A. T. [2023]. "Multi-hazard assessment of transmission line systems subjected to independent non-concurrent turbulent winds and ground accelerations." *Structural Safety*, 105, 102376.

Misra, S. and Padgett, J. E. [2019]. "Seismic fragility of railway bridge classes: methods, models, and comparison with the state of the art." *Journal of Bridge Engineering*, 24(12), 04019116.

Mitchell-Wallace, K., Jones, M., Hillier, J., and Foote, M. [2017]. *Natural Catastrophe Risk Management and Modelling: A Practitioner's Guide*. John Wiley & Sons, Hoboken, NJ.

Mohammadi Darestani, Y. and Shafieezadeh, A. [2019]. "Multi-dimensional wind fragility functions for wood utility poles." *Engineering Structures*, 183, 937–948.

Mohammadi Darestani, Y., Shafieezadeh, A., and Cha, K. [2020]. "Effect of modelling complexities on extreme wind hazard performance of steel lattice transmission towers." *Structure and Infrastructure Engineering*, 16(6), 898–915.

Muhr, E. [n.d.]. "Single-circuit transmission tower [Photograph]". Retrieved from `https://unsplash.com/@ericmuhr`.

Murphy, K. P. [2012]. *Machine learning: a probabilistic perspective*. MIT press.

National Hurricane Center [2025]. "National Hurricane Center". Retrieved from `https://www.nhc.noaa.gov/`.

NERC [2018]. *Hurrican Harvey Event Analysis Report*. North Amereican Electric Reliability Coporation. Retrieved from `https://www.nerc.com/pa/rrm/ea/Hurricane_Harvey_EAR_DL/NERC_Hurricane_Harvey_EAR_20180309.pdf`.

Nielson, B. G. [2005]. "Analytical fragility curves for highway bridges in moderate seismic zones." Ph.D. thesis, Georgia Institute of Technology, Atlanta,

GA. Retrieved from https://www.proquest.com/docview/304998824/abstract/CF0106146D02465DPQ/1.

Nielson, B. G. and DesRoches, R. [2006]. "Influence of modeling assumptions on the seismic response of multi-span simply supported steel girder bridges in moderate seismic zones." *Engineering Structures*, 28(8), 1083–1092.

Ouyang, M. and Duenas-Osorio, L. [2014]. "Multi-dimensional hurricane resilience assessment of electric power systems." *Structural Safety*, 48, 15–24.

Padgett, J. E. [2007]. "Seismic vulnerability assessment of retrofitted bridges using probabilistic methods." Ph.D. thesis, Georgia Institute of Technology, Atlanta, GA. Retrieved from https://repository.gatech.edu/handle/1853/14469.

Padgett, J. E. and DesRoches, R. [2007]. "Sensitivity of Seismic Response and Fragility to Parameter Uncertainty." *Journal of Structural Engineering*, 133(12), 1710–1718.

Padgett, J. E., Nielson, B. G., and DesRoches, R. [2008]. "Selection of optimal intensity measures in probabilistic seismic demand models of highway bridge portfolios." *Earthquake engineering & structural dynamics*, 37(5), 711–725.

Padilha Alves, G., Fadel Miguel, L. F., Holdorf Lopez, R., and Beck, A. T. [2024]. "Reliability assessment of guyed transmission towers through active learning metamodeling and progressive collapse simulation." *Structure and Infrastructure Engineering*, 20(5), 715–729.

Patsialis, D. and Taflanidis, A. A. [2020]. "Reduced order modeling of hysteretic structural response and applications to seismic risk assessment." *Engineering Structures*, 209, 110135.

Pedregosa, F., Varoquaux, G., Gramfort, A., Michel, V., Thirion, B., Grisel, O., Blondel, M., Prettenhofer, P., Weiss, R., Dubourg, V., Vanderplas, J., Passos, A., Cournapeau, D.,

Brucher, M., Perrot, M., and Duchesnay, E. [2011]. "Scikit-learn: Machine learning in Python." *Journal of Machine Learning Research*, 12, 2825–2830.

Porter, K. and Cho, I. [2013]. "Characterizing a building class via key features and index buildings for class-level vulnerability functions." *Proceedings of the 11th International Conference on Structural Safety & Reliability (ICOSSAR)*, New York, NY.

Power Line Systems [n.d.]. "TOWER [Computer software]".

PRAISys [2025]. "PRAISys: Probabilistic Resilience Assessment for Interdependent Systems". Retrieved from `http://www.praisys.org/`.

Rincon, R. and Padgett, J. E. [2024]. "Fragility modeling practices and their implications on risk and resilience analysis: From the structure to the network scale." *Earthquake Spectra*, 40(1), 647–673.

Ryle, P. J. [1946]. "Steel tower economics." *Journal of the Institution of Electrical Engineers*, 93(523), 541–546.

Saves, P., Lafage, R., Bartoli, N., Diouane, Y., Bussemaker, J., Lefebvre, T., Hwang, J. T., Morlier, J., and Martins, J. R. R. A. [2024]. "SMT 2.0: A Surrogate Modeling Toolbox with a focus on hierarchical and mixed variables Gaussian processes." *Advances in Engineering Software*, 188, 103571.

Schofer, J., Bocchini, P., Burton, H., DesRoches, S., Heil, A., Knatz, G., Miller-Hooks, E., Phillips, A., Marquez, J. R., Rivas, V., Wells, J., and Wilson, S. [2021]. "Investing in Transportation Resilience: A Framework for Informed Choices." *Report no.*, The National Academies Press, Washington, D.C.

Schweikert, A. E., Nield, L., Otto, E., and Deinert, M. R. [2019]. "Resilience and critical power system infrastructure: Lessons learned from natural disasters and future research needs." *Report no.*, World Bank, Washington, DC.

SEA, B. H., BoM, J. K., Ginger, J., Franklin, J., Powell, M., Black, P., TTU, C. L., and UWO, C. M. [2010]. "Guidelines for converting between various wind averaging periods in tropical cyclone conditions.

Segura, R., Padgett, J. E., and Paultre, P. [2020]. "Metamodel-Based Seismic Fragility Analysis of Concrete Gravity Dams." *Journal of Structural Engineering*, 146(7), 04020121.

Seo, J., Dueñas-Osorio, L., Craig, J. I., and Goodno, B. J. [2012]. "Metamodel-based regional vulnerability estimate of irregular steel moment-frame structures subjected to earthquake events." *Engineering Structures*, 45, 585–597.

Sheng, C. and Bocchini, P. [2025]. "An improved physics-based hurricane track model over the north atlantic basin with its application for wind-hazard assessment." *Journal of Structural Engineering*, 151(9), 04025122.

Shinozuka, M., Feng, M. Q., Lee, J., and Naganuma, T. [2000]. "Statistical analysis of fragility curves." *Journal of Engineering Mechanics*, 126(12), 1224–1231.

Silva, V., Akkar, S., Baker, J., Bazzurro, P., Castro, J. M., Crowley, H., Dolsek, M., Galasso, C., Lagomarsino, S., Monteiro, R., Perrone, D., Pitilakis, K., and Vamvatsikos, D. [2019]. "Current Challenges and Future Trends in Analytical Fragility and Vulnerability Modeling." *Earthquake Spectra*, 35(4), 1927–1952.

Sobol, I. M. [2001]. "Global sensitivity indices for nonlinear mathematical models and their Monte Carlo estimates." *Mathematics and computers in simulation*, 55(1-3), 271–280.

Sousa, L., Silva, V., Marques, M., and Crowley, H. [2018]. "On the treatment of uncertainty in seismic vulnerability and portfolio risk assessment." *Earthquake Engineering & Structural Dynamics*, 47(1), 87–104.

Tabet, F. [2009]. “Static and Dynamic Analyses of a Transmission Towerline System Using A Simplified Model.” M.S. thesis, University of Manitoba, Winnipeg, MB.

Tapia-Hernández, E. and Sordo, E. [2017]. “Structural behaviour of lattice transmission towers subjected to wind load.” *Structure and Infrastructure Engineering*, 13(11), 1462–1475.

Tian, L., Zhang, X., and Fu, X. [2020]. “Fragility analysis of a long-span transmission tower–line system under wind loads.” *Advances in Structural Engineering*, 23(10), 2110–2120.

Ungkurapinan, N. [2000]. “A study of joint slip in galvanized bolted angle connections.” M.S. thesis, University of Manitoba, Winnipeg, MB. Retrieved from `http://hdl.handle.net/1993/2341`.

U.S. Army Corps of Engineers, Hydrologic Engineering Center [2025]. “National Structure Inventory (NSI) Documentation”. Retrieved from `https://www.hec.usace.army.mil/confluence/nsi/`.

U.S. Department of Agriculture, Rural Utilities Service [2015]. “Design manual for high voltage transmission lines.” *Report No. Bulletin 1724E-200*. Revised December 2, 2015. Retrieved from `https://www.rd.usda.gov/files/UEP_Bulletin_1724E-200.pdf`.

U.S. Department of Energy [2013]. *Comparing the Impacts of Northeast Hurricanes on Energy Infrastructure*. Office of Electricity Delivery and Energy Reliability, U.S. Department of Energy. Retrieved from `https://www.energy.gov/sites/prod/files/2013/04/f0/Northeast%20Storm%20Comparison_FINAL_041513c.pdf`.

U.S. Department of Transportation [2023]. “Resilience and Disaster Recovery (RDR) Tool Suite”. Retrieved from `https://github.com/VolpeUSDOT/RDR-Public`.

Venteicher, W., Begert, B., and Kaenel, C. V. [2023]. "Here's where California's power grid is most at risk for high winds and fire threat" (August). Retrieved from https://www.mercurynews.com/2023/08/23/heres-where-californias-power-grid-is-most-at-risk-for-high-winds-and-fire-threat/.

Viana, F. A., Gogu, C., and Goel, T. [2021]. "Surrogate modeling: tricks that endured the test of time and some recent developments." *Structural and Multidisciplinary Optimization*, 64(5), 2881–2908.

Wang, D., Chen, X., and Li, J. [2017a]. "Prediction of wind-induced buffeting response of overhead conductor: Comparison of linear and nonlinear analysis approaches." *Journal of Wind Engineering and Industrial Aerodynamics*, 167, 23–40.

Wang, H. and Wu, T. [2022]. "Statistical investigation of wind duration using a refined hurricane track model." *Journal of Wind Engineering and Industrial Aerodynamics*, 221, 104908.

Wang, X. and Bocchini, P. [2023]. "Predicting wildfire ignition induced by dynamic conductor swaying under strong winds." *Scientific Reports*, 13(1), 3998.

Wang, X. and Bocchini, P. [2025a]. "Parameterized class fragility models for transmission towers", https://doi.org/10.5281/zenodo.17504411. [Model].

Wang, X. and Bocchini, P. [2025b]. "Physics-based surrogate models of panels for portfolio analysis of transmission towers under hurricanes." *Structure and Infrastructure Engineering*, 1–26.

Wang, X. and Bocchini, P. [2025c]. "Simulated hurricane wind fields for Florida using a blending approach", https://doi.org/10.5281/zenodo.17504628. [Data set].

Wang, X., Bocchini, P., Venkitasubramaniam, P., and Xie, S. [2024]. "Dynamic traffic

simulation for transportation system resilience assessment." *Bridge Maintenance, Safety, Management, Digitalization and Sustainability*, CRC Press, 3259–3266.

Wang, X., Ma, L., and Bocchini, P. [2023]. "Panel-oriented surrogate model for developing class fragility curves for transmission towers." *14th International Conference on Applications of Statistics and Probability in Civil Engineering (ICASP14)*, Dublin, Ireland.

Wang, Z., Hill, D. J., Chen, G., and Dong, Z. Y. [2017b]. "Power system cascading risk assessment based on complex network theory." *Physica A: Statistical Mechanics and its Applications*, 482, 532–543.

Wen, Y. and Wu, C.-L. [2001]. "Uniform hazard ground motions for mid-america cities." *Earthquake spectra*, 17(2), 359–384.

Wikipedia contributors [2025a]. "Effects of Hurricane Irma in Florida". Retrieved from `https://en.wikipedia.org/wiki/Effects_of_Hurricane_Irma_in_Florida`.

Wikipedia contributors [2025b]. "Hurricane Michael". Retrieved from `https://en.wikipedia.org/wiki/Hurricane_Michael`.

Wikipedia contributors [2025c]. "Saffir–Simpson scale". Retrieved from `https://en.wikipedia.org/wiki/Saffir%E2%80%93Simpson_scale`.

Wong, C. and Miller, M. [2010]. "Guidelines for electrical transmission line structural loading. asce manuals and reports on engineering practice, vol. 74." *Amer. Soc. Civil Engineers*.

Xie, Y. [2025]. "Impact of component damage correlations on seismic fragility and risk assessment of multi-component bridge systems." *Structural Safety*, 102635.

Xu, C. and Gertner, G. Z. [2008]. "Uncertainty and sensitivity analysis for models with correlated parameters." *Reliability Engineering & System Safety*, 93(10), 1563–1573.

Xu, L., Lin, N., Xi, D., Feng, K., and Poor, H. V. [2024]. "Hazard resistance-based spatiotemporal risk analysis for distribution network outages during hurricanes." *IEEE Transactions on Power Systems*.

Xue, J., Mohammadi, F., Li, X., Sahraei-Ardakani, M., Ou, G., and Pu, Z. [2020]. "Impact of transmission tower-line interaction to the bulk power system during hurricane." *Reliability Engineering & System Safety*, 203, 107079.

Yasui, H., Marukawa, H., Momomura, Y., and Ohkuma, T. [1999]. "Analytical study on wind-induced vibration of power transmission towers." *Journal of wind engineering and industrial aerodynamics*, 83(1-3), 431–441.

Yi, S.-r., Taflanidis, A. A., Movaghar, P. T., and Galasso, C. [2025]. "Impact of structural information fidelity on reduced-order model development for regional risk assessment." *Structural Safety*, 116, 102602.

Zsarnoczay, A., Deierlein, G. G., McKenna, F., Schoettler, M., Yi, S.-r., Cetiner, B., Satish, A. B., Zhao, J., Bonus, J., Melaku, A. F., et al. [2025]. "An open-source simulation platform to support and foster research collaboration in natural hazards engineering." *Frontiers in Built Environment*, 11, 1590479.

Vita

Xinyue Wang（王新悦）was born in Weifang, China, in 1994. She earned her Bachelor of Science degree in Civil Engineering from Shandong University in 2016 and her Master of Science degree in Civil Engineering from Harbin Institute of Technology in 2019. During her studies, she received several honors, including the National Scholarship (top 0.2% nationwide) in 2015 and 2016. For her master's thesis, she conducted vulnerability assessments of a high-rise building under mainshock-aftershock sequences. In 2019, Xinyue joined Lehigh University to pursue a Ph.D. in Structural Engineering.

Journal Articles Published

Wang, X., and Bocchini, P. (2025). "Physics-based surrogate models of panels for portfolio analysis of transmission towers under hurricanes." *Structure and Infrastructure Engineering*, 1–26.

Wang, X., and Bocchini, P. (2023). "Predicting wildfire ignition induced by dynamic conductor swaying under strong winds." *Scientific Reports*, 13(1), Article 1.

Wang, X., Wen, W., and Zhai, C. (2020). "Vulnerability assessment of a high-rise building subjected to mainshock–aftershock sequences." *The Structural Design of Tall and Special Buildings*, 29(15), e1786.

Zhai, C., Bao, X., Zheng, Z., and **Wang, X.** (2018). "Impact of aftershocks on a post-mainshock damaged containment structure considering duration." *Soil Dynamics and Earthquake Engineering*, 115, 129–141.

Manuscripts in Preparation

Wang, X., and Bocchini, P. (2025). "Using parameterized fragility models for hurricane risk analysis of power transmission networks."

Wang, X., and Bocchini, P. (2025). "Parameterized class fragility model for transmission towers under hurricane wind."